2017-12-01

Ion Trajectory Simulations and Design Optimization of Toroidal Ion Trap Mass Spectrometers

Jessica Marie Higgs
Brigham Young University

Ion Trajectory Simulations and Design Optimization of Toroidal Ion Trap Mass Spectrometers

Jessica Marie Higgs

A dissertation submitted to the faculty of
Brigham Young University
in partial fulfillment of the requirements for the degree of

Doctor of Philosophy

Daniel E. Austin, Chair
Jaron C. Hansen
David D. Dearden
Paul B. Farnsworth
Merritt B. Andrus

Department of Chemistry and Biochemistry

Brigham Young University

ABSTRACT

Ion Trajectory Simulations and Design Optimization of Toroidal Ion Trap Mass Spectrometers

Jessica Marie Higgs
Department of Chemistry and Biochemistry, BYU
Doctor of Philosophy

Ion traps can easily be miniaturized to become portable mass spectrometers. Trapped ions can be ejected by adjusting voltage settings of the radiofrequency (RF) signal applied to the electrodes. Several ion trap designs include the quadrupole ion trap (QIT), cylindrical ion trap (CIT), linear ion trap (LIT), rectilinear ion trap (RIT), toroidal ion trap, and cylindrical toroidal ion trap. Although toroidal ion traps are being used more widely in miniaturized mass spectrometers, there is a lack of fundamental understanding of how the toroidal electric field affects ion motion, and therefore, the ion trap's performance as a mass analyzer. Simulation programs can be used to discover how traps with toroidal geometry can be optimized.

Potential mapping, field calculations, and simulations of ion motion were used to compare three types of toroidal ion traps: a symmetric and an asymmetric trap made using hyperbolic electrodes, and a simplified trap made using cylindrical electrodes. Toroidal harmonics, which represent solutions to the Laplace equation in a toroidal coordinate system, may be useful to understand toroidal ion traps. Ion trapping and ion motion simulations were performed in a time-varying electric potential representing the symmetric, second-order toroidal harmonic of the second kind—the solution most analogous to the conventional, Cartesian quadrupole. This potential distribution, which we call the toroidal quadrupole, demonstrated non-ideal features in the stability diagram of the toroidal quadrupole which were similar to that for conventional ion traps with higher-order field contributions. To eliminate or reduce these non-ideal features, other solutions to the Laplace equation can be added to the toroidal quadrupole, namely the toroidal dipole, toroidal hexapole, toroidal octopole, and toroidal decapole. The addition of a toroidal hexapole component to the toroidal quadrupole provides improvement in ion trapping, and is expected to play an important role in optimizing the performance of all types of toroidal ion trap mass spectrometers.

The cylindrical toroidal ion trap has been miniaturized for a portable mass spectrometer. The first miniaturized version (r_0 and z_0 reduced by 1/3) used the same central electrode and alignment sleeve as the original design, but it had too high of capacitance for the desired RF frequency. The second miniaturized version (R, r_0, and z_0 reduced by 1/3) was designed with much less capacitance, but several issues including electrode alignment and sample pressure control caused the mass spectra to have poor resolution. The third miniaturized design used a different alignment method, and its efficiency still needs to be improved.

Keywords: toroidal ion trap, potential mapping, ion simulation, collisional cooling model, stability diagram, SIMION, toroidal harmonics

ACKNOWLEDGEMENTS

First I would like to thank my research adviser Dr. Austin for giving me the opportunity to work in his research group at Brigham Young University. The experiences I have had while working here has expanded my skills in the field of mass spectrometry and my confidence in my abilities. At times when I was discouraged with myself, Dr. Austin was there to help me keep up with the research.

I would also like to thank Dr. Hansen, Dr. Dearden, Dr. Farnsworth, and Dr. Andrus as part of my research committee as well as Dr. Prince who was on my committee for my first two years. They helped review my progress through my graduate school experience and offered suggestions for my research. I'd also like to thank Dr. Spencer from the Physics and Astronomy department in helping me learn Matlab for data processing.

I have to thank the collaborators that helped me with my research projects. Dr. Lammert from PerkinElmer and Dr. Warnick from the Engineering and Technology Department came up with the calculations for the toroidal harmonics.

I also want to thank the research group members that have also contributed to my projects. Dr. Nick Taylor showed me the operation of the cylindrical toroidal ion and the basics of SIMION. Brae V. Petersen helped with programming the simulations during his summer internship. Kit White and Dr. Ailin Li also helped in the assembly and operation of the miniaturized cylindrical toroidal ion traps. I'd also like to thank my other group members, past and present, for their support in reviewing presentations for progress reports and conferences.

I also thank the Precision Machining Lab for machining the parts for the various trap designs and the NASA Planetary Instrument Definition and Development Program for funding.

Finally, I want to thank my family and friends for supporting me emotionally through graduate school. My mother was there to remind me what I have been working towards. My siblings and my friends also helped me keep going through the rough patches in life. They also helped me keep balance in my life.

TABLE OF CONTENTS

LIST OF TABLES

LIST OF FIGURES

1 ION TRAP THEORY AND APPLICATION

1.1 Portable Mass Spectrometry

Mass spectrometry has been used since then 1910's in characterizing, identifying, and quantifying chemical samples [1] [2] [3]. This type of chemical analysis consists of producing gaseous ions, separating the resulting ions and fragment ions by their mass-to-charge ratio (*m/z*), and detecting the ions. This analytical method has been used in various fields of study including environmental studies [4] [5] [6], agriculture [7], detection of dangerous chemicals [8] [9] [10], forensics [11], and space exploration [12] [13].

Often, results can take a long time because of the time it takes to transport the sample to the laboratory and because of the backlog of samples. There are also instances when results are needed as soon as possible where immediate action is required. In order to get timely results, a portable mass spectrometer can be taken to the field and analyze samples on-site [14]. These portable mass spectrometers can either be transported by vehicle [15] or carried by a person [16] [17] depending on the accessibility of the location and size of the instrument.

Several types of mass spectrometers are limited in their use as portable instruments [18] [19]. Many mass analyzers have large sizes, and almost all need pressure in the µtorr range or less, but a good candidate for portability is the ion trap [20] [21] [22]. The mass analyzer is already a small size, and it actually benefits from operating at a higher pressure (in the mtorr range) [23].

1.2 Ion Trap Theory

Wolfgang Paul developed the quadrupole ion trap (QIT) in 1953 as an ion storage device [20]. The design was based on taking the cross section of the quadrupole mass filter (QMF) and rotating it about a central axis. The electrodes have hyperbolic shapes that share asymptotic slopes (Figure 1-1). A radiofrequency (RF) waveform of usually around 1 MHz is applied to the ring electrode while the endcap electrodes can be grounded or have a constant voltage applied. In 1959, its trapping capabilities were utilized for mass analysis [24].

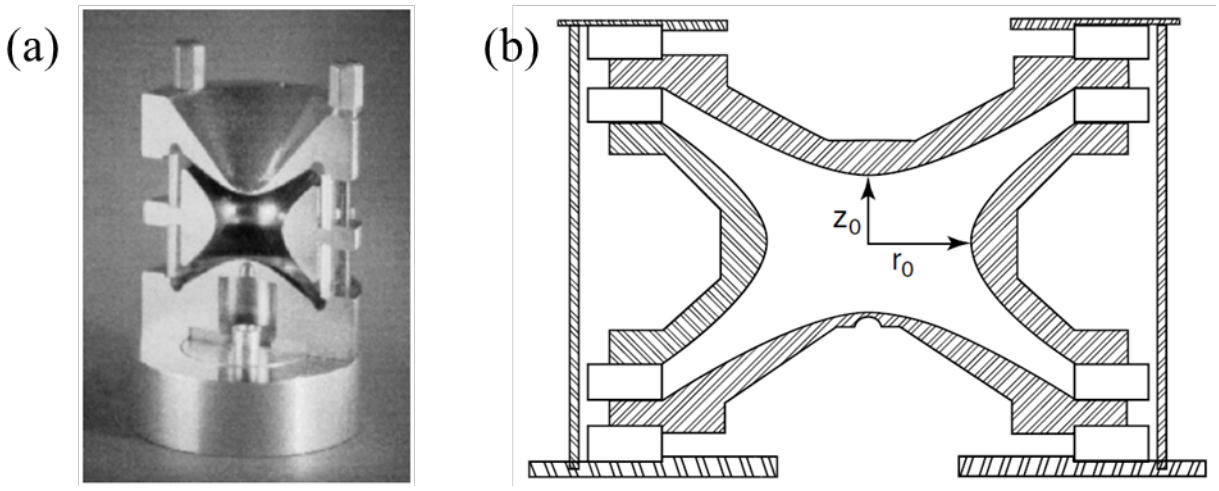

Figure 1-1: Quadrupole ion trap: (a) photograph of ion trap cut in half along axis of cylindrical symmetry; (b) schematic diagram of three-dimensional ideal ion trap showing asymptotes and dimensions r_0 and z_0. (Adapted from R. E. March and J. F. J. Todd, Quadrupole Ion Trap Mass Spectrometry, Second Edition, Hoboken, NJ: Wiley-Interscience, 2005. [25])

Other fields of study have also benefitted from utilizing ion traps. Wolfgang Paul [26], Hans G. Dehmelt [27], and David J. Wineland [28] received Nobel Prizes in Physics for work involving ion traps. The work for most recent award in 2012 by Wineland involved using trapped ions for quantum logic gates that could be utilized in quantum computing [29] [30]. Trapped ions

have been used as frequency standards [31] [32] [33] and can also be used for various spectroscopic analyses [34] [35] [36] [37].

1.2.1 Quadrupole Ion Trap Potential

The time-independent potential inside a pure quadrupole trap can be represented as

$$\Phi_{x,y,z} = A(\lambda x^2 + \sigma y^2 + \gamma z^2) + C \tag{1-1}$$

where x, y, and z are the rectangular coordinates within a trap, A represents the electric potential applied between the ring electrode and endcap electrodes, C is the potential (or DC offset) applied to all the electrodes, and λ, σ, and γ are weighting constants for their respective coordinates [25]. Given that

$$\nabla^2 = \frac{\partial^2}{\partial x^2} + \frac{\partial^2}{\partial y^2} + \frac{\partial^2}{\partial z^2} \tag{1-2}$$

the Laplace condition states that the second derivative of the potential must be equal to zero at a given point inside a trap

$$\nabla^2 \Phi_{x,y,z} = \frac{\partial^2 \phi}{\partial x^2} + \frac{\partial^2 \phi}{\partial y^2} + \frac{\partial^2 \phi}{\partial z^2} = 0 \tag{1-3}$$

Performing the partial derivatives on the potential function leads to

$$\nabla^2 \Phi = A(2\lambda + 2\sigma + 2\gamma) = 0 \tag{1-4}$$

$$\lambda + \sigma + \gamma = 0 \tag{1-5}$$

Because the QIT is cylindrically symmetric, the weighting constants are equal to

$$\lambda = \sigma = 1 \text{ and } \gamma = -2 \tag{1-6}$$

Because the QIT operates with RF applied to the ring electrode, the voltage difference between the electrodes at any given time t can be represented by the time-dependent relation:

$$\Phi_0 = U + V\cos(\Omega t) \tag{1-7}$$

where U is the DC voltage, V is the RF amplitude, and Ω is the RF frequency. The trapping potential of a QIT at any given position (x, y, z) can be represented by the following equation:

$$\Phi = \frac{1}{2}(U - V\cos(\Omega t))\frac{(x^2+y^2-2z^2)}{r_0^2} + \frac{U-V\cos(\Omega t)}{2} \quad (1\text{-}8)$$

where r_0 is the inner radius of the ring electrode [38]. The spacing of the electrodes within the trap is typically optimized to $r_0^2 = 2z_0^2$, where $2z_0$ is the distance between the endcap electrodes.

1.2.2 Trapped Ion Motion and Stability

The electric potential applied to the electrodes creates a force on the ion. The ion motion that results from this force can be described by the Mathieu equation [39]

$$\frac{d^2u}{d\xi^2} + (a_u + 2q_u\cos(2\xi))u = 0 \quad (1\text{-}9)$$

where u represents either x, y, or z and $\xi = \frac{\Omega t}{2}$. The Mathieu stability parameters, $a_u$and q_u for the QIT can be defined as

$$a_z = -2a_x = -2a_y = \frac{-16eU}{m(r_0^2+2z_0^2)\Omega^2} \quad (1\text{-}10)$$

$$q_z = -2q_x = -2q_y = \frac{8eV}{m(r_0^2+2z_0^2)\Omega^2} \quad (1\text{-}11)$$

with e as the electrical charge [40] [41]. Because the QIT is cylindrically symmetric, the directions x and y can be combined in a radial direction r.

An ion is considered to be stably trapped when the ion motion is contained within the trapping volume for some length of time. This motion in both the r and z directions consists of a secular frequency and several other frequencies that make up the micromotion. The secular frequency can be calculated by

$$\omega_{u,n} = \left(n + \frac{1}{2}\beta_u\right)\Omega \text{ for } 0 \leq n < \infty \quad (1\text{-}12)$$

$$\omega_{u,n} = -\left(n + \frac{1}{2}\beta_u\right)\Omega \text{ for } -\infty < n < 0 \tag{1-13}$$

where ω_u is the secular frequency in the direction r or z in radians per second, n is the order of angular frequency, and β_u is the secondary trapping parameter. The value of this secondary trapping parameter for the QIT can be approximated by [25]

$$\beta_u \approx \sqrt{a_u + \frac{1}{2}q_u^2} \tag{1-14}$$

but can also be calculated by the recursion formula [39]

$$\beta_u^2 = a_u + \frac{q_u^2}{(\beta_u+2)^2 - a_u - \frac{q_u^2}{(\beta_u+4)^2 - a_u - \frac{q_u^2}{(\beta_u+6)^2 - a_u - \cdots}}} + \frac{q_u^2}{(\beta_u-2)^2 - a_u - \frac{q_u^2}{(\beta_u-4)^2 - a_u - \frac{q_u^2}{(\beta_u-6)^2 - a_u - \cdots}}}. \tag{1-15}$$

An ion's motion can be considered stable when both β_r and β_z are between 0 and 1.0. If the ion's stability is outside this range for β_r, the ion is ejected radially, and if it's outside the range for β_z, the ion is ejected axially. Graphing the region where the ion motion is stable on a plot of a_z vs. q_z gives us a stability diagram (Figure 1-2). When any of the voltage settings (V, U, or Ω) is varied, an ion's β_u shifts, and the ion can be ejected when the stability parameters cross one of the boundaries of the stability diagram.

In using an ion trap for mass analysis, there are several methods that researchers developed. The first mode of operation is the forward scan with boundary ejection [42] [43]. In this case, ions are trapped at low RF amplitude. As the RF amplitude is increased, the q_z stability parameter also increases and approaches the boundary of the stability diagram. This results in ions with lower mass-to-charge ratio being ejected first and ions with higher *m/z* being ejected later.

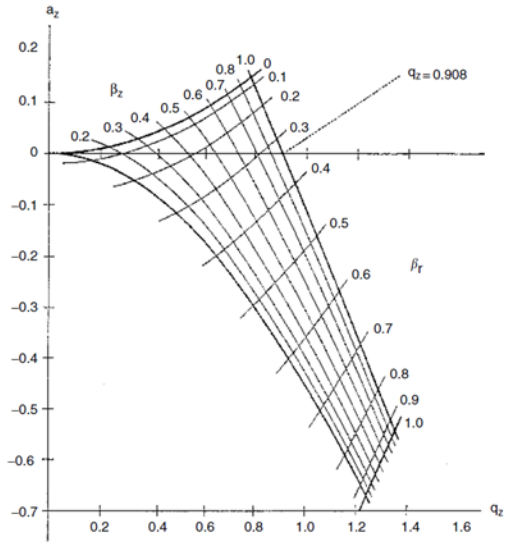

Figure 1-2: Stability diagram in (a_z, q_z) space in both r and z directions the near origin for the three-dimensional QIT; the iso-β_r and iso-β_z lines are shown in the diagram. The q_z axis intersects the β_z = 1 boundary at q_z = 0.908, which corresponds to q_{max} in the mass-selective instability mode. Conventially, the stability diagram in (a_z, q_z) space is presented. (Reproduced from R. E. March and J. F. J. Todd, Quadrupole Ion Trap Mass Spectrometry, Second Edition, Hoboken, NJ: Wiley-Interscience, 2005. [25])

While still using this forward scan, resonant ejection can also be used to eject ions that are not at the boundary of the stability diagram [38]. An auxiliary AC voltage is applied to the endcap electrodes when the scan starts. When ions of the same *m/z* have their secular motion in resonance with the AC, they gain enough energy from the supplementary field to be ejected from the trap. This method also improves resolution as the ions are bunched as they are being ejected.

Another operation mode is the reverse scan [44]. The RF amplitude is set high enough so that the ion of the lowest *m/z* is just inside the β_z = 1 boundary. The DC voltage can be increased, and the RF amplitude and DC Voltage are decreased together for the ion to be ejected at the β_z = 0 boundary. Resonant ejection with AC can also be used without varying the DC voltage. This allows for ions of higher *m/z* to be ejected first and the ions with lower *m/z* to be ejected later.

Another useful mode is tandem analysis [38]. After all ions are initially trapped, ions at one *m/z* value are selected for further analysis and the rest of the ions are ejected. This can be done by apex isolation where an ion's a_z and q_z stability parameters are increased by adjusting both the RF amplitude and DC offset. When the stability of the ion of interest is near the upper apex of the stability diagram, ions outside that narrow range are ejected. Another method of ion isolation is a sweep of supplementary AC signal where the sweeping AC frequency skips the frequency of the ion of interest so that all other ions are ejected. The selected ion can then undergo fragmentation by collision-induced dissociation (CID), and the resulting ions can be analyzed by either forward or reverse scan. CID is implemented by applying an AC signal to the endcap electrodes as a tickle voltage.

The stability of ion motion can also be visualized by just considering the secular motion of an ion. This simplifies to a particle experiencing harmonic motion in a parabolic well. This harmonic motion can be expressed in the pseudopotential well model as both [39]

$$\left\langle \frac{d^2u}{dt^2} \right\rangle_{1\ rf\ cylcle} = \left\langle \frac{d^2L}{dt^2} \right\rangle_{1\ rf\ cylcle} = \frac{-\Omega^2}{4}\left(a_u + \frac{1}{2}q_u^2\right)L \tag{1-16}$$

$$\frac{d^2L}{dt^2} = -\omega_{u,0}^2 L \tag{1-17}$$

where L is the fundamental secular motion. For an ion to remain trapped, its kinetic energy cannot exceed the threshold to escape the pseudopotential well. When ions are generated inside the trap by either electron ionization (EI) or chemical ionization (CI), only the ions that have less kinetic energy than this threshold are trapped while the rest either hit an electrode or escape the trap. When ions are generated externally and transferred to the trap, collisions with the

background gas reduce the kinetic energy of the ions. Ions that don't lose enough kinetic energy can continue through the trap without being trapped in the pseudopotential well.

1.2.3 Higher Order Field Components

In an ideal QIT, the electric field for a quadrupolar potential distribution would be a linear function in any direction measured. This is not the case for real traps. Where an ideal QIT would have perfectly hyperbolic shaped electrodes that extend to infinity, real traps have truncated electrodes with exit slits, manufacturing defects within given tolerances, and possible misalignment of electrodes. These differences make changes to the electric fields that disrupt the linearity [45].

One way to mathematically represent the resulting field is to consider it to be a sum of mostly a linear field with contributions from higher-order fields [25]. This can be represented by the equation

$$\Phi(\rho,\theta,\varphi) = \Phi_0 \sum_{n=0}^{\infty} \left(A_n \frac{\rho^n}{r_0^n} P_n(\cos\theta) \right) \tag{1-18}$$

where ρ, θ, and φ are spherical coordinates, Φ_0 is the potential applied to the electrodes, n represents the order of the field component, A_n is the weighting factor for each order n, and P_n is a Legendre polynomial of order n. These orders come from solutions to the Laplace equation with the same symmetry as the trap. The fields are named for their order number: monopole (n = 0), dipole (n = 1), quadrupole (n = 2), hexapole (n = 3), octopole (n = 4), decapole (n = 5), dodecapole (n = 6), and so on. These can also be classified as either even- (n = 0, 2, 4, 6, …) or odd- (n = 1, 3, 5, …) ordered multipoles. For a pure quadrupole, this equation simplifies to

$$\Phi_{r,z} = \Phi_0 A_2 \frac{r^2 - 2z^2}{2r_0^2}, \tag{1-19}$$

but when considering orders n = 2 to n = 6, the equation is

$$\Phi_{r,z} = \Phi_0 \left(A_2 \frac{r^2 - 2z^2}{2r_0^2} + A_3 \frac{3r^2 z - 2z^3}{2r_0^3} + A_4 \frac{3r^4 - 24r^2 z^2 + 8z^4}{8r_0^4} + A_5 \frac{15r^4 z - 40r^2 z^3 + 8z^5}{8r_0^5} + A_6 \frac{5r^6 - 90r^4 z^2 + 120r^2 z^4 - 16z^6}{16r_0^6} \right). \quad (1\text{-}20)$$

These multipole contributions become important when looking at the effect on trapped ion motion. In a pure quadrupole, the motion in the r and z directions are independent from each other, and each direction's frequency is independent from its amplitude. The a_z and q_z stability parameters are the only factors determining if the ion is stably trapped. Also, the frequencies that make up the ion motion besides the secular frequency consists of basic sidebands including $\Omega - \omega_z$, $\Omega + \omega_z$, and $2\Omega - \omega_z$ [45].

With higher-order multipole contributions, the axial and radial frequencies become coupled to each other, and the frequency and amplitude are no longer independent. The ion also experiences overtones in the frequencies that make up its motion. This can cause the ion to take up energy from the RF drive which increases its secular amplitude, and so the secular frequency also shifts. This shift in frequency can cause the ion motion to adopt a beat pattern. This can also cause resonance lines of instability to appear in the stability diagram. The field at the exact trapping center resembles that of a quadrupole, but as an ion deviates from the trapping center, it is affected by more of the effects of other field contributions. While a pure field of one of these multipoles can be used as an ion trap or an ion guide [46] [47], pure higher-order fields haven't proved useful for mass analysis [48] [49]. As contributions to a linear field, these can either have beneficial or detrimental effects on trapping and ejecting ions [50].

In the case of even multipoles, such as the octopole, there are resonance lines in the stability diagram seen at $\beta_z = ½$, $\beta_z + \beta_r = 1$, and $\beta_r = ½$. Because of the coupling of the amplitude and frequency of ion motion, the amplitude of the ion motion can keep the ion trapped

when approaching some resonant lines. This can either be beneficial in the case of reducing the effects of resonant lines or detrimental in the case of resonant ejection.

In the case of odd multipoles such as the hexapole, resonance lines can be seen at $\beta_z = ⅔$ and $2\beta_r + \beta_z = 2$. The secular frequency of an ion can increase or decrease depending on whether the ion located above or below the radial plane. This can cause ions to be ejected through one endcap electrode rather than both endcap electrodes. The overtone frequencies of ion motion include values of $n\omega_z$, $-\Omega + n\omega_z$, $\Omega - n\omega_z$, $\Omega + n\omega_z$, and $3\Omega - n\omega_z$.

1.2.4 Ion Trap Miniaturization

The ion trap dimensions affect the stability of trapped ions inversely as seen in Equations 1-10 and 1-11:

$$a_z = \frac{-16eU}{m(r_0^2+2z_0^2)\Omega^2} \tag{1-10}$$

$$q_z = \frac{8eV}{m(r_0^2+2z_0^2)\Omega^2}. \tag{1-11}$$

When reducing r_0 and z_0, the same stability parameters for a given ion can be maintained by reducing the voltages U and V, increasing the RF frequency Ω, or both. The lower voltages allow for lower power electronics [51]. The increased frequency allows for faster mass analysis times [52]. Another benefit of a smaller mass analyzer is that higher pressure helps collisionally cool and trap ions; this allows for a less powerful vacuum pump [53] [54].

There are two main problems with miniaturizing ion traps. One issue is space-charge effects. When ions are confined to a small space, their charges cause a mutual repulsion and limit the number of ions that can be contained [55]. This can also cause issues with resolution, accuracy, sensitivity, and dynamic range [56]. Another issue is the limitations in

electrode manufacturing tolerances. With smaller dimensions, the tolerances must be tighter in order to produce the same field shape accuracy as the original size [57]. With these main issues for miniaturization, researchers have developed other ion trap designs that have increased ion capacity and/or electrode shapes easier for manufacturing.

1.3 Different Ion Trap Geometries

The use of ion traps has expanded to many applications. With this, several designs of ion traps have been developed to improve either performance or manufacturing. The original QIT used hyperbolic electrode shapes in order to produce a perfect quadrupolar potential distribution [20]. Some ion trap designs, such as the cylindrical ion trap (CIT) [58] and rectilinear ion trap (RIT) [59], simplified their electrode shapes, and the traps' performances were maintained as long as the fields at the traps' centers were linear. Other trap designs such as the linear ion trap (LIT) [60] and toroidal ion trap [61] increased the trapping volume for a given trap size in order to increase their signal.

1.3.1 Quadrupole Ion Trap

Before utilizing mass-selective ejection for mass analysis, the QIT was operated in other modes. When the QIT (Figure 1-1) was developed, the first method of mass analysis was mass-selective detection [62] [24]. In this mode, the stable ion motion is sensed by the endcap electrodes. While this method is non-destructive by keeping the ions trapped during analysis, the mass range and resolution were limited. Only a few years after the invention of the QIT, mass-selective storage was able to trap ions of a single *m/z* value [25] [63].

It wasn't until the 1980's that Finnigan Corporation operated the QIT in mass-selective ejection [42] [43] [64]. Their first design had mass range and resolution limitations. When they introduced helium gas at about 1 mtorr to the vacuum system in order to couple the QIT with gas chromatography (GC), the mass resolution and sensitivity improved. Later in development, they also saw slight mass shifts for particular ion species of a sample. With experimentation, they saw that spacing out the endcap electrodes reversed this mass shift effect. This extra spacing countered the even higher-order fields introduced by the exit holes in the endcap electrodes and by the truncation of the electrodes. This spacing of the electrodes remained a trade secret since the instrument's release in 1984 until an announcement was made in 1992 to inform users of this non-ideal geometry [65].

1.3.2 Cylindrical Ion Trap

While the operation of the QIT was being explored, a simplified version of the ion trap was also being utilized. In 1962 Langmuir et al. [58] developed the cylindrical ion trap (CIT) as an ion containment device. Instead of hyperbolic electrode shapes, the CIT consisted of a cylindrical ring electrode and planar endcap electrodes, which would be easier for trap manufacturing (Figure 1-3 (a)). Its performance was first demonstrated in 1973 by Benilan and Audoin [66], and further explanation of how its performance was different from the QIT was provided in 1977 by Bonner et al. [67]. Because the field deviates from linearity when further from the trapping center, the stability of a trapped ion depends on its position [68]. The stability diagram also differs from that of the QIT slightly (Figure 1-3 (b)) [69] [68]. In 1998 Wells et al. [69] performed the first mass-selective instability scan using a CIT.

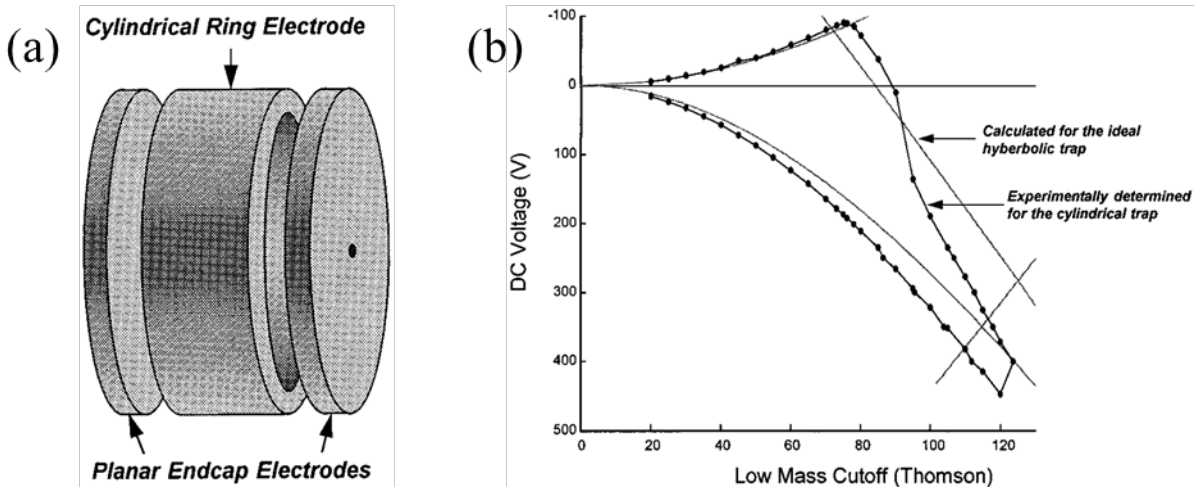

Figure 1-3: The Cylindrical Ion Trap. (a) Concept of a cylindrical ion trap as an approximation to the hyperbolic Paul trap. (b) Stability Diagram determined for a CIT with z_0 = 0.897 cm and r_0 = 1.0 cm by monitoring the abundance of *m/z* 84 from Kr as a function the amplitude of the RF and DC potentials applied to the ring electrode. Axial modulation at 460 kHz, 4 V. (Adapted from J. M. Wells, E. R. Badman and R. G. Cooks, "A Quadrupole Ion Trap with Cylindrical Geometry Operated in the Mass-Selective Instability Mode," *Anal. Chem.*, vol. 70, no. 3, pp. 438–444, 1998. [69])

Because the electrode shapes have been simplified, the CIT design can be easily miniaturized [57]. In 1998 Badman et al. [70] made a miniature CIT with a trapping radius of 2.5 mm. While their resolution was poorer than a full-sized trap at $\Delta m/z$ = 1.4, the signal intensity and signal-to-noise proved that the miniature design was still useful. In 1999 Kornienko et al. [71] miniaturized the CIT further with a trapping radius of 0.5 mm with an improved resolution at $\Delta m/z$ = 0.25. In 2010 Jesseph et al. [72] demonstrated that this size of CIT can be used for ion isolation and CID for tandem analysis. Wu et al. [73] used simulations to optimize the performance of the CIT by adjusting the electrode spacing. With ion trap miniaturization, the signal intensity decreases with the trapping capacity. In order to maintain good signal, an array of CITs can be used to multiply the number of trapped ions that can be analyzed [74] [75] [76] [77] [78].

1.3.3 Linear Ion Trap

One solution to increase the ion capacity of a trap is to change the dimensions of the trapping region. In the case of the QIT and the CIT, ions are trapped within a three-dimensional (3D) field. For the linear ion trap (LIT) (Figure 1-4), QMF rod electrodes can be adapted to trap ions within linear fields in a two-dimensional (2D) field with electrodes at either end to keep ions within the length of the rods [79] [80]. Additional benefits of the LIT include the ease of coupling to other mass analyzers [81] and higher trapping efficiency of externally-generated ions [25].

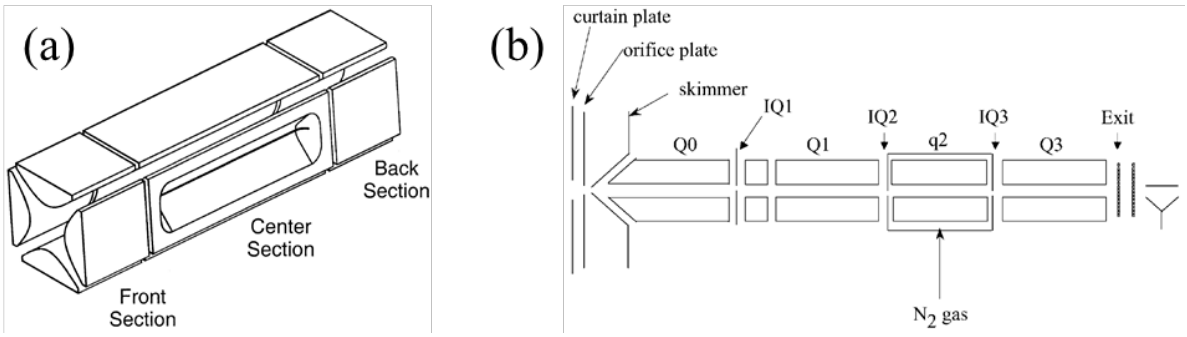

Figure 1-4: The Linear Ion Trap. (a) Basic design of the two-dimensional linear ion trap. (Adapted from J. C. Schwartz, M. W. Senko and J. E. P. Syka, "A Two-Dimensional Quadrupole Ion Trap Mass Spectrometer," *J. Am. Soc. Mass Spectrom.*, vol. 13, no. 6, pp. 659–669, 2002. [56]) (b) Schematic portrayal of the experimental apparatus based in the ion path of a triple quadrupole mass spectrometer. The linear ion trap mass spectrometer was created using either q2 or Q3. (Adapted from J. W. Hager, "A New Linear Ion Trap Mass Spectrometer," *Rapid Commun. Mass Spectrom.*, vol. 16, no. 6, pp. 512–526, 2002. [82])

Before the present-day design of the LIT, several ion storage devices used a similar concept that trapped in ions in a circular or racetrack configuration [83] [84] [85]. In the late 1980's, two research groups trapped ions in the collision cell of a tandem QMF to study and enhance ion-molecule reactions [86] [87] [88]. As a mass spectrometer, ions can be ejected either perpendicular to the central axis [60] [89] or axially [90]. In 1994 Bier and Syka [60] filed a patent for the Thermo Finnigan (Thermo Scientific) LIT (Figure 1-4 (a)), and in 2002 Schwartz et al. [56]

demonstrated its performance. In this design, ions are ejected radially through one of the electrodes. In 1998 Hager filed a patent for the MDS SCIEX (AB SCIEX) LIT (Figure 1-4 (b)) [90], and in 2002 he demonstrated its performance [82]. In this arrangement of QMF sections, either of the last two sections can be operated as an ion trap, and an auxiliary AC applied can excite the ion motion of the matching secular frequency causing the ions to be ejected axially.

1.3.4 Rectilinear Ion Trap

Another ion trap design uses the expanded ion capacity of the LIT and the simplified electrode shapes of the CIT. This rectilinear ion trap (RIT) consists of two pairs of planar electrodes which provide the 2D trapping field and one pair of endcap electrodes (Figure 1-5) [25] [91]. In 2003 Ouyang and Cooks [59] filed for a patent for the RIT, and the group subsequently demonstrated its performance [92] [93] [94]. In 2006 Tabert et al. [95] developed a multiplexed RIT analyzer to analyze four samples at the same time. In 2008 Peng at al. [96] used the RIT to eject mass-selected ions and deposit them on a surface.

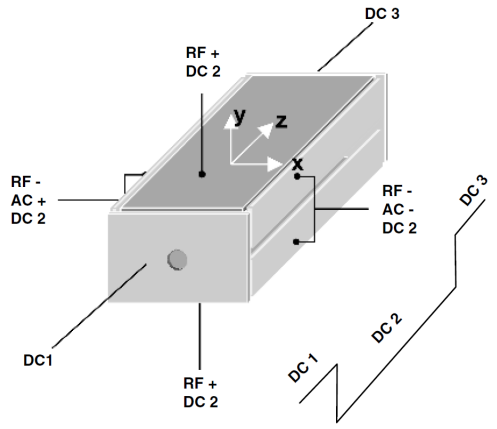

Figure 1-5: Configuration of the rectilinear ion trap and its operational mode. (Reproduced from Z. Ouyang, G. Wu, Y. Song, H. Li, W. R. Plass and R. G. Cooks, "Rectilinear Ion Trap: Concepts, Calculations, and Analytical Performance of a New Mass Analyzer," *Anal. Chem.*, vol. 76, no. 16, pp. 4595–4605, 2004. [92])

1.3.5 Toroidal Ion Trap

As another way to increase ion capacity, the electrodes for the LIT can be curved so that the two ends can be joined together and the ions are trapped in a ring or torus [97]. Lammert et al. [61] first developed the toroidal ion trap as a mass spectrometer with two variations (Figure 1-6). The first design called the symmetric toroidal ion trap (Figure 1-6 (a)) took the cross section of the stretched QIT and displaced the axis of rotation to outside the trapping region of the trap. This design suffered from poor resolution because of the additional fields contributed by the curvature of the device. To improve the performance of the device, the endcaps were spaced further out and the asymptotic angles were adjusted to be steeper for the inner electrode and less steep for the outer electrode. This asymmetric toroidal ion trap (Figure 1-6 (b)) contained fields more similar to the QIT and demonstrated unit mass resolution. This asymmetric design was used for miniaturization [98] and commercialized as part of a portable GC-MS [99].

1.3.6 Cylindrical Toroidal Ion Trap

In 2012 Taylor and Austin [100] took the toroidal ion trap and applied the concept of using simplified electrodes similar to the CIT and RIT (Figure 1-7). This simplified or cylindrical toroidal ion trap also applied the RF to the endcap electrodes instead of the central and ring electrodes so that the ions could be ejected radially inward to the detection components inside the central electrode without the need of focusing the ions. This design demonstrated better resolution than the asymmetric toroidal ion trap while using a reverse scan with resonant ejection. They also demonstrated the tandem analysis capabilities.

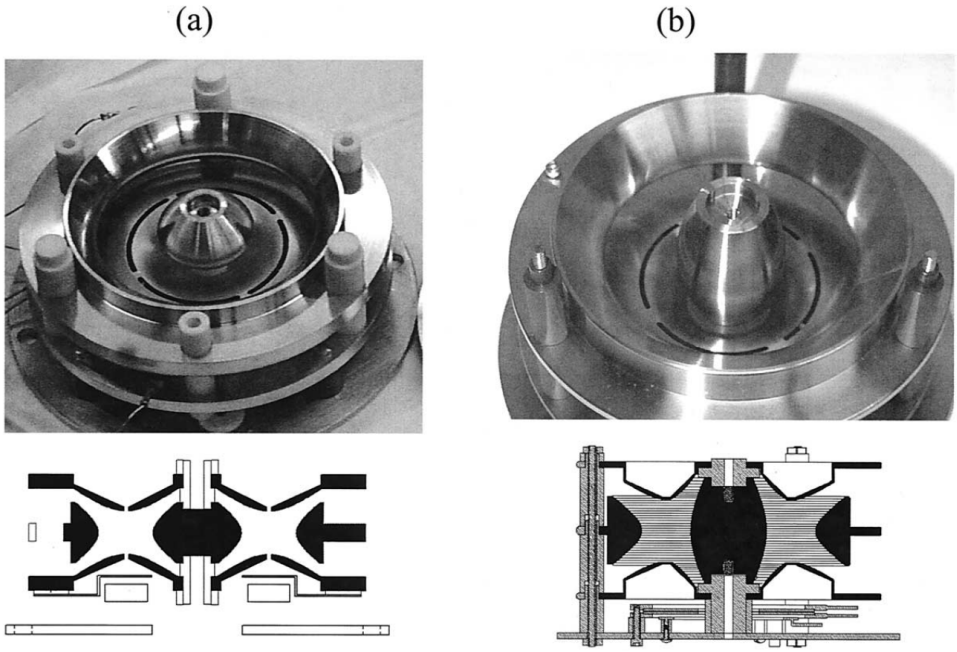

Figure 1-6: Photographs (filament endcap removed) and line drawings of the analyzer components for the (a) symmetric toroidal ion trap and the (b) asymmetric toroidal ion trap. (Reproduced from S. A. Lammert, W. R. Plass, C. V. Thompson and M. B. Wise, "Design, Optimization and Initial Performance of a Toroidal RF Ion Trap Mass Spectrometer," *Int. J. Mass Spectrom.*, vol. 212, pp. 25–40, 2001. [61])

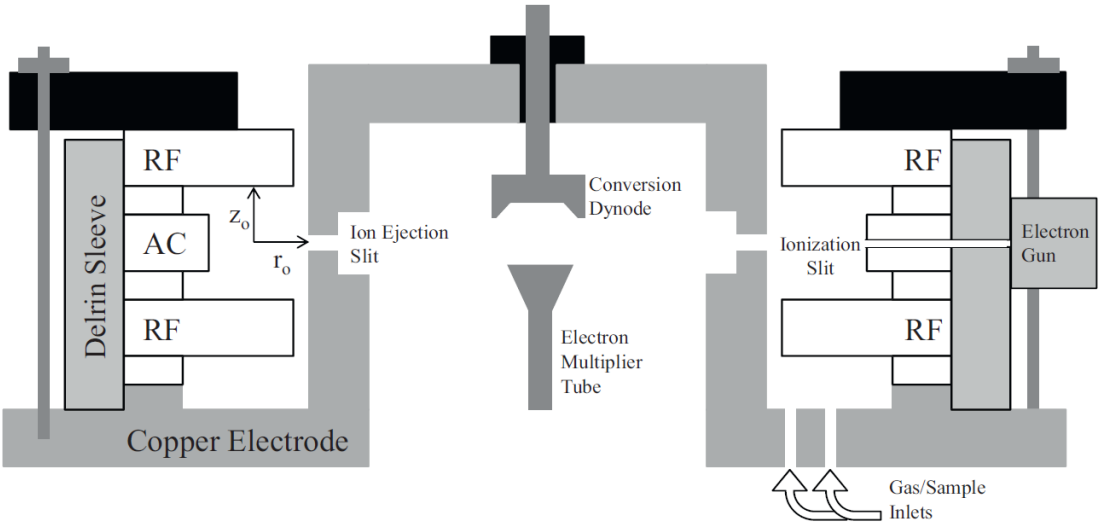

Figure 1-7: Cross-sectional illustration of the design used to construct the prototype simplified toroidal ion trap mass analyzer. Not drawn to scale. (Reproduced from N. R. Taylor and D. E. Austin, "A Simplified Toroidal Ion Trap Mass Analyzer," *Int. J. Mass Spectrom.*, Vols. 321–322, pp. 25–32, 2012. [100])

1.4 Simulation Programs

One way to compare the theoretical performance of several ion trap designs is recording the electric fields as well as observing the ion motion. While it is not possible to record all of the ion motion data *in situ*, computer simulations can calculate the expected ion motion resulting from the RF fields produced by electrodes input by the user [25]. Not only can computer simulations compare the performance of existing ion traps, but they can also be used to determine the performance of proposed ion traps. In this way, ion trap developers can explore many factors affecting the performance of an ion trap before manufacturing and assembling one design. These factors include electrode shape and size, voltage settings (RF frequency, RF amplitude, DC offset, supplementary AC), and pressure of the background gas. By adjusting these factors, ion traps can be optimized for commercial use. There have been three computer programs used for simulating ion motion in ion traps: ITSIM, ISIS, and SIMION [101].

1.4.1 ITSIM

Ion Trajectory Simulation (ITSIM) was developed by R. Graham Cooks' group [102], and the program has been used for resonant ejection [103], ion injection with buffer gas [104], and visualizing ion trajectories [105]. It was originally developed for DOS operating systems, but later was developed for Windows operating system [106]. Users can change all experimental conditions both prior and during a simulation, and the simulation can run a large number of ions.

1.4.2 ISIS

Integrated System for Ion Simulation (ISIS) was developed by Raymond E. March's group which consisted of modules for the direct integration of the Mathieu equation, the field interpolation method, and simulation program for quadrupolar resonance [107] [108]. The program

has been used for kinetic energy studies [109] [110] [111], effects of fields during axial modulation and mass-selective isolation [112] [113], and analysis of resonantly excited ions [114].

1.4.3 SIMION

Ion and Electron Optics Simulation Package (SIMION) was developed in 1973 by Don McGilvery, and in 1986 David A. Dahl developed it for the PC [115]. The program has been used to simulate ion motion in several types of mass spectrometers including QMF, QIT, and time-of-flight [116] [117]. It has also been used to study ion injection for ion traps [118] and ion optics for external ion sources [119] [120]. While SIMION provides some example electrode shapes and user programs [121], users may also enter custom electrode shapes and write their own user programs in order to simulate any mass spectrometer.

In SIMION, electrode shapes can be custom made by entering them into a potential array (.PA of .PA#) file. When entering the electrode shape manually, the user must first define the dimensions of the array in grid units (gu) and whether the array will have planar and/or cylindrical symmetry. Grid units can then be selected for the electrode shapes. When creating a .PA# file, electrodes can be given different numbers that can be used later in the voltage controls as identification. Once the array is created, SIMION can refine the array with solving the Laplace equation (Equation 1-3) by finite difference methods.

Once a potential array file has been refined, the user can define the scaling (mm/gu) of the array and create the user programs. These user programs can be used to control various conditions such as the voltage settings, the collisional model with the background gas, and data recording. The user may use Equation 1-7 to define the electric potential of the RF electrodes and implement an RF amplitude ramp for a mass analysis. With a given time step, the field in the

array is recalculated. In order for the simulation to run, at least one particle needs to be present. The user can control the number of particles as well as the mass, charge, initial position, initial velocity, and the start time of the particle. As the field is recalculated at each time step, a particle's position and velocity are also recalculated with the effects of the electric field. The user can also control if another particle is simulated after the current particle "splats" on an electrode surface or array boundary.

For outputting data, the user may select variables for data output by using either the graphical user interface (gui) or the user program. The gui can be used to record data for the flight time, mass, charge, position, velocity, and acceleration of the particle as well as the electric potential and field that the particle experiences. The user program can also be used to record this data as well as any of the variables used in the user program and other reserved variables. The recorded data can either be saved in the same location as the simulation file or in another location.

1.5 Purpose

Because of the high ion capacity of toroidal ion traps, there has been work to evaluate and optimize ion traps with toroidal geometry. The theory for the operation of toroidal ion traps has not been determined because the calculations used for conventional traps cannot be applied directly. In order to understand this theory, SIMION 8.0 can simulate ion motion for both existing toroidal ion trap designs and theoretical toroidal ion trap designs. With this work, it will be possible to improve the toroidal ion trap design and make a miniaturized toroidal ion trap mass spectrometer.

In Chapter 2, SIMION 8.0 maps the potential distribution and simulates ion motion in three existing toroidal ion trap designs. In Chapter 3, simulated ion motion in a trap with the

potential distribution of a harmonic in a toroidal coordinate system explores the field and stability diagram of a pure toroidal quadrupole. In Chapter 4, this toroidal quadrupole is combined with several other toroidal harmonics in order to observe changes and improvements to the stability diagram. In Chapter 5, the cylindrical toroidal ion trap is miniaturized to work towards its use as a portable mass spectrometer. Chapter 6 presents future research for toroidal ion trap optimization and miniaturization.

2 SIMULATIONS OF ION MOTION IN TOROIDAL ION TRAPS

(This chapter has been published as an article: "Higgs, J. M.; Austin, D. E. Simulations of ion motion in toroidal ion traps. International Journal of Mass Spectrometry. 2014, 363, 40–51." [122]. *My individual contribution was creating the electrode shapes for simulation, simulating ion motion, and writing the draft manuscript.)*

2.1 Introduction

The ion trap mass spectrometer has proven to be sensitive while providing tandem analysis with a single instrument [38]. Furthermore, it is an excellent candidate for miniaturization and on-site analysis. Miniaturization of ion traps lowers the requirements of the vacuum system and power, and analysis time is reduced proportionally with increased RF frequency [54] [52] [51]. However, miniaturization and fabrication of smaller electrodes diminish ion capacity. As the trapping volume decreases with miniaturization, space-charge effects decrease ion capacity [24] [123] [55]. Another concern with smaller trap designs is that the tolerance requirements for the hyperbolic electrode shapes become tighter, and manufacturing exact dimensions becomes more difficult [57] [25].

To increase ion trap capacity, Lammert et al. [61] in 2001 developed two designs of a toroidal ion trap mass spectrometer. The trapped ions were spread out in a ring (or a torus) rather than clustered about a single point as in a quadrupole ion trap (QIT). The toroidal ion trap design was based on the cross section of the commercial QIT by rotating the cross section along an axis external to the trapping region. The symmetric toroidal ion trap (Figure 2-1 (a) and (b)) used the same asymptotic slopes for the hyperbolic electrodes as the QIT. The asymmetric toroidal ion

trap (Figure 2-1 (c) and (d)) used different asymptotic slopes for the inner and outer electrodes in order to optimize mass resolution. The asymmetric toroidal ion trap design has been used for miniaturization [98] and has been included in a portable GC-MS system [99].

In 2012 Taylor and Austin [100] developed another toroidal ion trap design (Figure 2-1 (e) and (f)) based on the simplified electrode shapes of the cylindrical ion trap [124] [69] [70]; this modification makes the electrodes easier to manufacture compared to hyperbolic electrodes. Different from previous ion trap designs, this simplified toroidal ion trap employed radial ejection of ions from the trap rather than axial ejection by applying RF to the endcap electrodes and a supplementary ac signal (to resonantly excite radial secular motion) to the inner and outer electrodes. For field comparisons, the radial direction (r) of the simplified toroidal ion trap should be compared with the axial direction (z) of previous ion trap designs.

Lammert et al. [61] determined that the toroidal ion trap design cannot have a pure quadrupole potential due to the major radius (radius of curvature) of the ion trapping region. The asymmetric toroidal ion trap was optimized to be nearly quadrupolar about the trapping center and have the trapping center lined up with the ejection slits. Although they compared the field maps for the symmetric and asymmetric toroidal ion traps, they did not calculate the exact values of higher-order fields. Wang et al. [124] determined that traditional mathematical calculations of higher-order multipoles are incorrect for the toroidal ion trap design due to the field being discontinuous at the axis of rotation. As an approximation, Taylor and Austin [100] used these calculations of higher-order fields to evaluate trapping fields in the simplified toroidal ion trap.

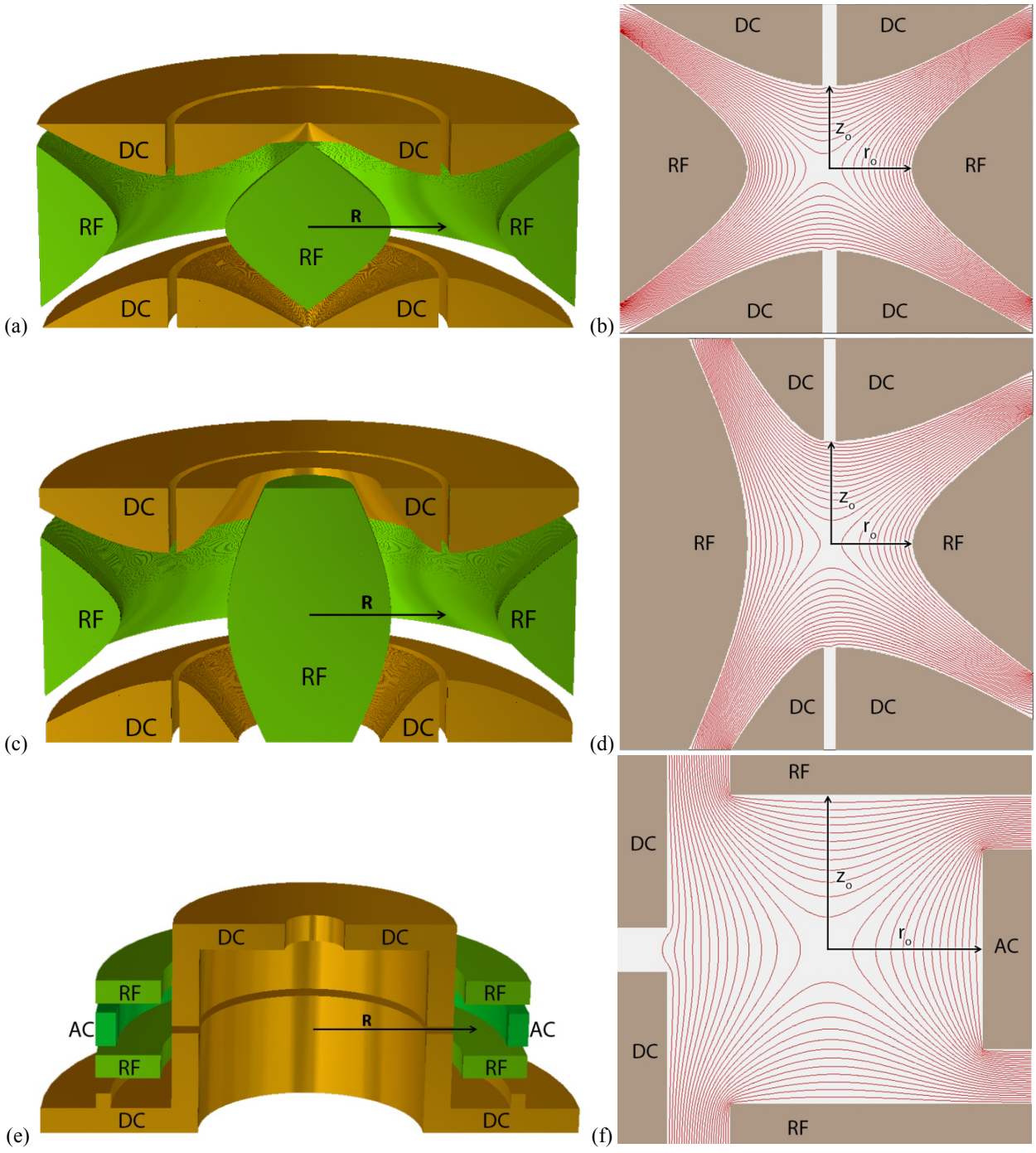

Figure 2-1: Images of the (a) and (b) symmetric, (c) and (d) asymmetric, and (e) and (f) simplified toroidal ion traps from SIMION 8.0 [121]. Dimensions are taken from Lammert et al. [61] and Taylor and Austin [100]. (a), (c), and (e) Full image of trap with DC electrodes, RF electrodes, and major radii (R) labeled. (b), (d), and (f) Trapping region with isopotential lines and DC electrodes, RF electrodes, minor radii (r_0), and endcap separation (z_0) labeled.

For quadrupole ion traps with defects in the electrode shapes (apertures in the endcaps, electrode truncation, etc.), the potential measured across the trapping region is not purely quadrupolar (x^2), but includes monopolar (x^0), dipolar, (x^1), hexapolar (x^3), octopolar (x^4), decapolar (x^5), and other higher-order polar contributions [45]. These multipole contributions cause the potential to deviate from a quadratic function. The electric field is calculated by the derivative of the potential function and can be compared to the QIT linear field to observe deviations. A common method for calculating higher-order multipoles in ion traps includes a high-order polynomial fit to the potential function to determine the contributions of each field contribution. Polynomial fits up to the 44^{th} power have been used in order to improve the accuracy of the lower fields of interest [125].

Computer simulations of ion motion can be used to understand the effects of higher-order multipoles. Franzen [50] demonstrated the benefits and drawbacks of superimposed hexapole and octopole fields in the QIT. He showed that with a certain amount of hexapolar and octopolar fields superimposed on a quadrupolar field, ion ejection proved to be fast and unidirectional. Also, performing Fourier transform on data of ion oscillation quantifies the frequencies and amplitudes of secular motion and micromotion. Simulations performed by Franzen, et al. [45] gave amplitude spectra of ion motion in different types of fields. In a pure quadrupole, the RF driving frequency (Ω = 1 MHz) is not seen due the symmetric nature of the motion's waveform, but only the secular axial frequency (ω_z = 0.27 MHz) and other axial frequencies of $\Omega - \omega_z$, $\Omega + \omega_z$, and $2\Omega - \omega_z$ are seen in the range of 0–2 MHz. When higher-order multipoles are introduced, other frequencies become present. Introducing a hexapole component adds Ω because of the asymmetry of the waveform as well as the harmonic frequencies of $n\omega_z$, $-\Omega + n\omega_z$, $\Omega \pm n\omega_z$, $2\Omega - n\omega_z$, and $3\Omega - n\omega_z$. Decapole and other odd-ordered multipole components give higher intensities of these

higher harmonics. Introducing an octopole component adds only the odd harmonic frequencies of $n\omega_z$, $\Omega \pm n\omega_z$, $-\Omega + n\omega_z$, $2\Omega - n\omega_z$, $-2\Omega + n\omega_z$, and $3\Omega - n\omega_z$. Another effect of higher-order multipoles is coupling of axial and radial motion (ω_z and ω_r). These couplings include taking up energy in one or both directions and exchanging energy between the two directions resulting in a shift of ω_u and/or a change in amplitude.

Another way to examine the influence of higher-order fields is to observe ion motion with stability near the β_z = 1.0 boundary. In 2001 Sudakov [126] reported that the ion motion adopts a beat envelope near this boundary. Also, pairs of harmonics have approximately equal amplitudes, and the ion motion is governed by higher fields. He determined that any hexapole contributions have the same effect as negative octopole contributions. Negative higher field components cause ions to hit the electrode surfaces when the potential well minima are beyond the trap boundaries. While investigating ion-neutral collisions, background gas dampens the ion motion to an equilibrium state independent of the initial conditions when the gas molecule mass is small compared to the ion mass.

There have been no published reports of simulation studies for any of the toroidal ion trap designs. Whereas the QIT has only two dimensions of ion motion (axial and radial), ions in toroidal ion traps move in three independent dimensions−axial, radial, and tangential, as illustrated in Figure 2-2. This difference allows ions in toroidal traps to move around the major radius of the trapping region. This curvature of the trap can also impose a different electric field than either the QIT or quadrupole mass filter, so ion motion along the ion path in a circle would be a unique aspect of toroidal ion traps.

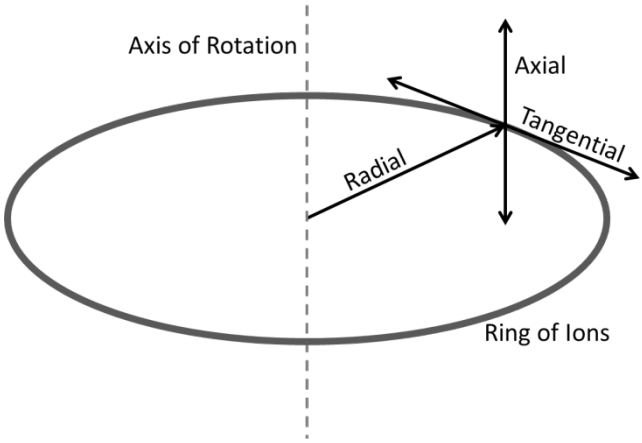

Figure 2-2: The three independent directions of ion motion in toroidal ion traps.

There is a lack of understanding of higher-order field contributions and their effects on ion motion in toroidal ion traps. Such understanding would aid in design, operation, and experiments utilizing ion traps of toroidal geometry. The present study uses potential mapping to compare the higher-order field contributions for the symmetric toroidal ion trap, the asymmetric toroidal ion trap, and the simplified toroidal ion trap. Also, this study employs simulations of ion motion within these traps under various conditions to describe secular frequencies and observe behavior unique to these types of traps.

2.2 Methods

2.2.1 Overview

SIMION 8.0 [121] (Scientific Instrument Services, Inc., Ringoes, NJ) was used for potential mapping and ion motion simulations for the symmetric toroidal ion trap, asymmetric toroidal ion trap, and simplified toroidal ion trap. Data processing for field calculations and secular frequencies was performed with MATLAB (MathWorks, Natick, MA).

2.2.2 Electrode Arrays

Figure 2-1 (b), (d), and (f) shows the cross section of the trapping region of the three toroidal ion traps as viewed in SIMION 8.0 [121]. The dimensions of the full-sized symmetric (R = 25.4 mm, r_0 = 10. mm, z_0 = 7.83 mm, slit width = 0.178 × r_0) and asymmetric (R = 25.4 mm, r_0 = 10. mm, z_0 = 12.5 mm, slit width = 0.15 × r_0) toroidal ion traps came from reference [61], and the dimensions of the simplified toroidal ion trap (R = 36.1 mm, r_0 = 5.91 mm, z_0 = 5.81 mm, slit width = 0.275 × z_0) came from reference [100]. The potential mapping simulations used a scaling of 0.02 mm per grid unit (gu), and the ion motion simulations used a scaling of 0.1 mm/gu. The symmetry of the electrodes was set to cylindrical. The size of the arrays for potential mapping in the symmetric, asymmetric, and simplified toroidal ion traps were 2000 × 2500, 2500 × 2500, and 2500 × 3000 gu, respectively, and the size of the arrays for simulated ion motion were 400 × 500, 500 × 500, and 500 × 600 gu, respectively. The electrodes of the symmetric toroidal ion trap were truncated at 2.46 × r_0 and 2.55 × z_0 from the trapping center, and the electrodes of the asymmetric toroidal ion trap were truncated at 2.46 × r_0 and 2.0 × z_0 from the trapping center. The sizes of the electrodes of the simplified toroidal ion trap were based on the manufactured dimensions with the ring electrodes truncated at 1.75 × r_0 and 1.90 × z_0 from the trapping center.

2.2.3 Field Calculations.

SIMION 8.0 [121] was used to calculate the potential across the trapping region of each toroidal ion trap design. The data was fit with a 25th order polynomial to calculate the contributions of higher-order field contributions as used in previous studies [100] [127] [128]. This polynomial was then used to determine the percent (A_n/A_2 x 100%) of the 3rd, 4th, and 5th order field contributions. The field was calculated by taking the derivative of the potential

function. To show the non-linear contributions, an extrapolation of the central linear region was calculated and subtracted from the potential function. For comparison, the fields were normalized to the trapping field dimensions.

2.2.4 User Programs.

SIMION 8.0 provides example user programs [121] which were modified for this study. The ion trap user programs controlled the voltages and RF frequency applied to the electrodes. All the designs had an RF amplitude of 500 $V_{0\text{-}p}$ for initial simulations, and additional simulations set the RF amplitude to 810 $V_{0\text{-}p}$ for the symmetric toroidal ion trap and 1650 $V_{0\text{-}p}$ for the asymmetric toroidal ion trap to match the q-stability of the m/z 100 ion in the simplified toroidal ion trap according to the standard equation for the QIT. The RF frequencies of the symmetric, asymmetric, and simplified toroidal ion traps were set at 0.990 MHz, 1.038 MHz, and 1.14 MHz, respectively, as reported in their respective studies [61] [100]. These frequencies differ because of differences in capacitance and power supplies used in the studies. The user programs were incorporated with a hard-sphere collision model in agreement with previous studies [129] [130]. The user programs were executed with the random distribution of the ion's initial position and velocity disabled in order to compare results. The potential energy surface of the trapping region was updated every 0.05 μs to approximate a smooth RF waveform. The simulations observed ion motion without collisions (0 Pa) and with collisions at approximately 1 mtorr (1.333 Pa) with helium (4 amu) as the background gas.

2.2.5 Ion Flight Conditions.

The particle for each simulation had a mass-to-charge ratio of m/z 100 with its initial position near the trapping center. We adjusted the variables of the direction of initial velocity

(radial, axial, or tangential) and the total amount of initial kinetic energy (0–10 eV) without collisions for the three toroidal ion trap designs. The position of the ion was recorded with respect to time. For simulations with collisions, initial studies used the same variable conditions as used in the studies without collisions. Subsequent studies started the ion with no kinetic energy while recording the velocity and the kinetic energy with respect to time as well as the time stamps of the collisions. The collision cross section of the ion was set to 2.27×10^{-18} m^2, and observations were made at 273 K and 473 K.

2.2.6 Ion Motion Calculations.

For simulations without collisions, the coordinates of the ion with respect to time were converted to axial, angular, and radial positions, and the average radial position was also calculated. The position of the ion with respect to time was evaluated with MATLAB's Fourier transform function to identify the frequencies of motion with an amplitude spectrum. For simulations with collisions, the average kinetic energy, radial position, velocity, and collisional frequency were calculated by averaging the mean values for ten simulations. The mean free path was calculated from the average values for velocity and collisional frequency.

2.3 Results and Discussion

2.3.1 Field Calculations.

The polynomial equations from the potential mappings of the three designs were used to give numerical values to the 3rd, 4th, and 5th order field contributions of the symmetric, asymmetric, and simplified toroidal ion traps. Figure 2-3(a) shows these potential functions between the DC electrodes for the symmetric, asymmetric, and simplified toroidal ion traps

relative to their dimensions represented by u_0 (z_0 for axial, r_0 for radial). Table 2-1 shows the higher order field contributions calculated from the potential measured in the axial and radial directions. When selecting the boundaries of the polynomial fit for the simplified toroidal ion trap in the radial (ejection) direction, different boundaries resulted in different higher-order field contributions. This can be attributed to toroidal space having no true multipoles. This change in higher-order fields was not as dramatic for the symmetric or asymmetric toroidal ion traps. The polynomials for the potential functions between the RF electrodes gave different values of higher-order fields than the measurements between the DC electrodes (Table 2-1, Figure 2-3 (b)). This difference in higher order-fields is not typical for ion traps; in other cases, it is expected that the values of higher-order fields would be the same no matter where they are measured. Here, the different values of higher-order fields can be attributed to the fact that there are no true multipoles in toroidal space.

Table 2-1: Higher order term contributions calculated from the potential measured between the DC electrodes (ejection direction) and the RF electrodes.

	Symmetric		Asymmetric		Simplified	
Term of Field contribution	Axial (ejection)	Radial	Axial (ejection)	Radial	Radial (ejection)	Axial
A_3/A_2	0.0375%	–11.8%	0.0505%	–0.263%	2.30%	–0.0137%
A_4/A_2	–9.57%	19.4%	1.80%	1.36%	0.581%	–0.576%
A_5/A_2	0.235%	–16.7%	–0.954%	–0.892%	3.56%	0.397%

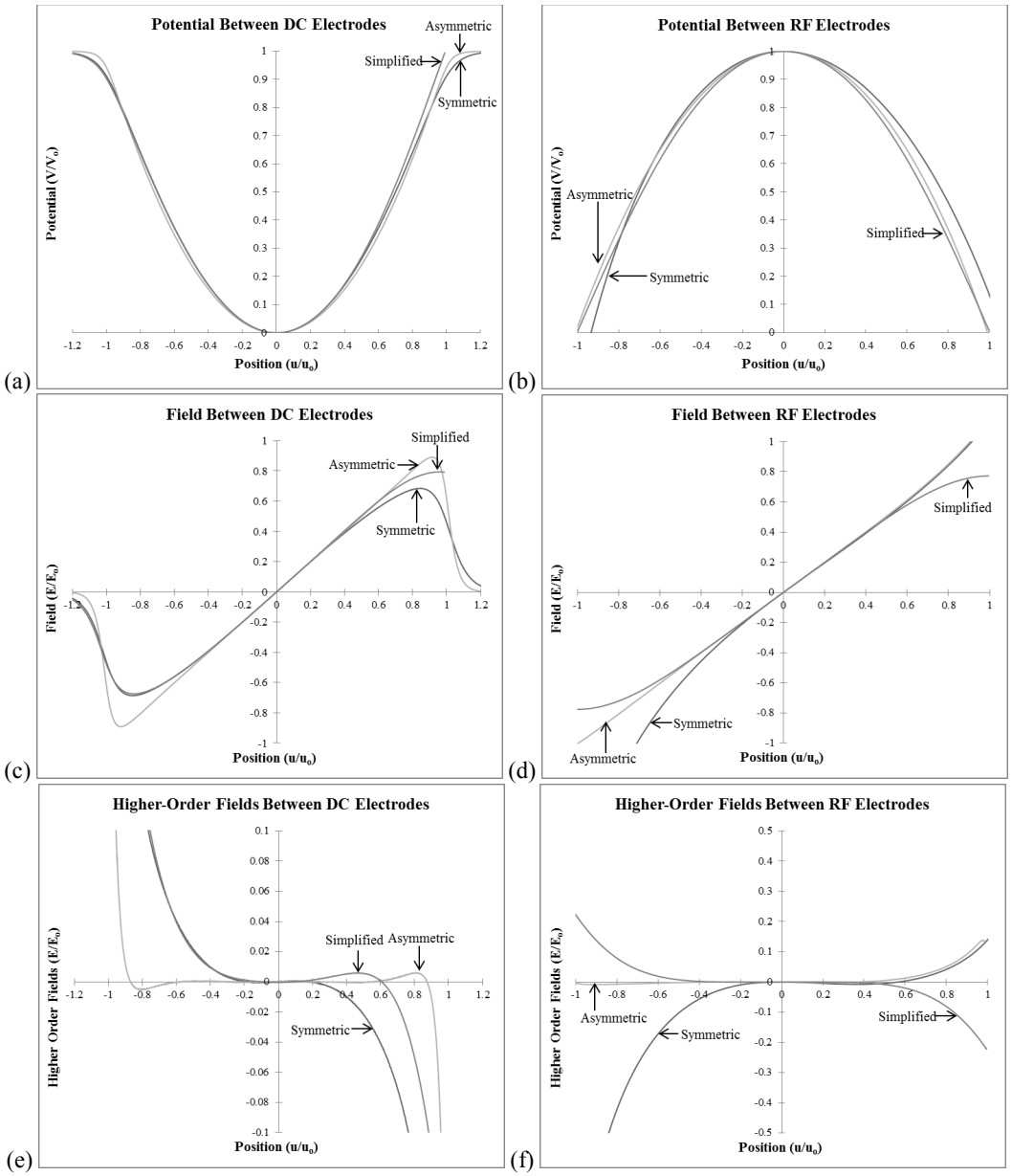

Figure 2-3: The potential, total field, and higher-order fields of the symmetric, asymmetric, and simplified toroidal ion traps. The graphs of potential between (a) the DC electrodes and (b) the RF electrodes compare the potential functions of the three toroidal ion trap designs. The graphs of total field between (c) the DC electrodes and (d) the RF electrodes show the deviations from linearity. Subtracting the linear component from the field between (e) the DC electrodes and (f) the RF electrodes show just the higher-order multipole contributions. Each potential function and field function passes through the saddle points of the traps. The saddle point for the symmetric toroidal ion trap was centered between the DC electrodes, 24.7 mm from the axis of rotation. The saddle point for the asymmetric toroidal ion trap was centered between the DC electrodes, 25.5 mm from the axis of rotation. The saddle point of the simplified toroidal ion trap was centered between the RF electrodes, 36.2 mm from the axis of rotation.

The fields for the symmetric, asymmetric, and simplified toroidal ion traps were compared to show the linearity of the fields near the trapping center. Figure 2-3 (c) and (d) shows the fields, and Figure 2-3 (e) and (f) shows the higher-order fields. The graphs of field calculations for the symmetric and asymmetric toroidal ion traps are comparable to the graphs of the calculations performed by Lammert et al. [61]. Differences between our field calculations and their calculations could be attributed to the difference in size of the major radius of the toroidal ion traps. As indicated by Lammert et al., the actual major radius (2.54 cm) contributes less field distortions from higher-order fields than the smaller major radius (2 cm) used for their calculations. In agreement to the study by Lammert et al. [61], the effects of higher-order fields are less in the asymmetric toroidal ion trap than in the symmetric toroidal ion trap due to the optimized geometry. The linear range for the asymmetric toroidal ion trap is wider than for the symmetric toroidal ion trap in both the axial and radial directions. In the axial direction, the range of linear field in the symmetric toroidal ion trap is about –0.2 to 0.2 z/z_0, and the range of the linear field in the asymmetric toroidal ion trap is about –0.6 to 0.6 z/z_0. As shown by Lammert et al., the symmetric toroidal ion trap has a sub-linear axial field, and the asymmetric toroidal ion trap has a super-linear axial field. In the radial direction, the range of linear field in the symmetric toroidal ion trap is about –0.1 to 0.2 r/r_0, and the range of linear field in the asymmetric toroidal ion trap is about –0.6 to 0.4 r/r_0.

The simplified toroidal ion trap appears to have higher-order fields closer to that of the symmetric toroidal ion trap. The high values of odd-order fields calculated can be seen in the radial field's asymmetry (Figure 2-3 (e)). The linear range in the radial direction is about –0.2 to 0.1 r/r_0, and the linear range in the axial direction is about –0.4 to 0.4 z/z_0. The radial field shows asymmetry with sub-linear field at the inner side of the trapping region and a super-linear

field at the outer side of the trapping region. While these field calculations predict that the simplified toroidal ion trap would have poor performance, its reported performance ($\Delta m = 0.32$) is comparable to that of the asymmetric toroidal ion trap ($\Delta m \approx 0.4$–0.5) [13]. Differences in performance of the simplified toroidal ion trap could be partly attributed to the larger major-to minor-radius ratio (R/r_0) compared with the other toroidal ion trap designs. The relative difference in slit widths (as compared with overall trapping dimensions) among the three designs may also have effects on the electric field profile and on performance.

In quadrupole devices (2-D and 3-D ion traps, as well as quadrupole mass filters), geometrical simplification such as circular rods and cylindrical/planar electrodes results in larger high-order field terms compared with the ideal electrode geometry, and sometimes results in reduced performance. However, none of these three devices represent the "ideal" toroidal geometry, which has yet to be identified. Hence, fields can be compared among the three traps, but cannot be compared with an ideal field.

2.3.2 Simulated Ion Motion Ignoring Collisions.

The simulations of ion motion showed how an ion would behave in the three toroidal ion trap designs in the absence of ion-neutral collisions. The initial velocity of the ion in the simulations was applied in either the axial, radial, or tangential direction. Table 2-2 summarizes the values of secular frequencies, the amplitude of the secular frequencies, and harmonic frequencies seen when varying the direction of initial velocity and the magnitude of initial kinetic energy. The simulations with axial initial velocity and with radial initial velocity were similar to motion seen in a QIT. The simulations with initial tangential velocity (tangent to the circular trapping region) have no analogue in any other ion trap designs because of the difference in symmetry.

Table 2-2: Summary of frequencies observed in ion motion in the radial (R) and axial (Z) directions. The ion used was *m/z* 100. The RF voltage was 500 $V_{0\text{-}p}$.

	Initial Velocity	KE (eV)	Motion	ω_u (kHz)	Amplitude (mm)	Relative Amplitude to ω_u								Other Harmonics; Notes
						$2\omega_u$	$\Omega-2\omega_u$	$\Omega-\omega_u$	Ω	$\Omega+\omega_u$	$\Omega+2\omega_u$	$2\Omega-\omega_u$	$2\Omega+\omega_u$	
Symmetric (Ω = 990 kHz)	Axial	0	R	101.1 ± 0.3	0.8772	0.0178	0.0038	0.1058	0.0042	0.0771	0.0013	0.0024	0.0014	$3\omega_r$, $\Omega-3\omega_r$, $2\Omega-2\omega_r$; Axial motion not significant
		0.01	R	101.1 ± 0.2	1.1665	0.0095	0.0027	0.0776	0.0024	0.0566	0.0012	0.0018	0.0009	$3\omega_r$, $\Omega-3\omega_r$, $2\Omega-2\omega_r$
			Z	100.3 ± 0.2	0.1616	0.0015	0.0007	0.1227	-------	0.0830	0.0003	0.0020	0.0009	$3\omega_z$, $\Omega-3\omega_z$
		0.1	R	101.1 ± 0.2	1.2465	0.0118	0.0019	0.0607	0.0020	0.0397	0.0008	0.0017	0.0009	$3\omega_r$, $\Omega-3\omega_r$, $2\Omega-2\omega_r$
			Z	100.0 ± 0.2	0.7225	0.0013	0.0004	0.0569	-------	0.0384	0.0002	0.0017	0.0009	$3\omega_z$, $\Omega-3\omega_z$
		1	R	100 ± 3	0.9373	0.0154	0.0024	0.0023	0.0017	0.0638	0.0015	0.0023	0.0013	$3\omega_r$, $\Omega-3\omega_r$, $\Omega+3\omega_r$, $2\Omega-2\omega_r$
			Z	97.6 ± 0.4	2.2573	0.0011	0.0005	0.0671	0.0002	0.0577	0.0002	0.0013	0.0006	$3\omega_z$, $\Omega-3\omega_z$, $\Omega+3\omega_z$
		5	R	107.5 ± 0.7	0.5400	0.0294	0.0027	0.0896	0.0052	0.0562	0.0011	0.0020	0.0013	Many harmonics
			Z	76.0 ± 0.7	3.9912	0.0115	0.0016	0.0798	0.0008	0.0632	0.0013	0.0006	0.0009	Many harmonics
	Radial	0	R	101.1 ± 0.4	1.2276	0.0109	0.0026	0.0885	0.0031	0.0524	0.0009	0.0016	0.0007	$3\omega_r$, $\Omega-3\omega_r$, $2\Omega-2\omega_r$; Axial motion not significant
		0.01	R	101.0 ± 0.2	0.8407	0.0005	0.0027	0.0854	0.0035	0.0598	0.0012	0.0017	0.0010	$3\omega_r$, $\Omega-3\omega_r$, $\Omega+3\omega_r$, $2\Omega-2\omega_r$; Axial motion not significant
		0.1	R	100.6 ± 0.2	0.5140	0.0012	0.0018	0.1319	0.0020	0.0876	0.0008	0.0017	0.0010	$3\omega_r$, $\Omega-3\omega_r$, $\Omega+3\omega_r$, $2\Omega-2\omega_r$; Axial motion not significant
		1	R	101.3 ± 0.2	1.3357	0.0114	0.0031	0.0933	0.0037	0.0478	0.0009	0.0017	0.0007	$3\omega_r$, $\Omega-3\omega_r$, $4\omega_r$, $\Omega+3\omega_r$, $\Omega-4\omega_r$, $2\Omega-2\omega_r$; Axial motion not significant
		10	R	116.7 ± 0.3	5.4273	0.0429	0.0083	0.0683	0.0091	0.0425	0.0031	0.0024	0.0012	$3\omega_r$, $4\omega_r$, $5\omega_r$, $6\omega_r$, $7\omega_r$, $8\omega_r$, $9\omega_r$, $10\omega_r$, $11\omega_r$, $12\omega_r$, $\Omega-8\omega_r$, $\Omega-7\omega_r$, $\Omega-6\omega_r$, $\Omega-5\omega_r$, $\Omega-4\omega_r$, $\Omega-3\omega_r$, $\Omega+3\omega_r$, $\Omega+4\omega_r$, $\Omega+5\omega_r$, $2\Omega-4\omega_r$, $2\Omega-3\omega_r$, $2\Omega-2\omega_r$; Axial motion not significant

Table 2-2 Continued

	Initial Velocity	KE (eV)	Motion	ω_u (kHz)	Amplitude (mm)	Relative Amplitude to ω_u								Other Harmonics; Notes
						$2\omega_u$	$\Omega-2\omega_u$	$\Omega-\omega_u$	Ω	$\Omega+\omega_u$	$\Omega+2\omega_u$	$2\Omega-\omega_u$	$2\Omega+\omega_u$	
Symmetric	Tangential	0	R	101.0 ± 0.7	1.0927	0.0109	0.0033	0.0934	0.0025	0.0609	0.0015	0.0015	0.0011	$3\omega_r$, $\Omega-3\omega_r$, $2\Omega-2\omega_r$; Axial motion not significant
		0.01	R	101.1 ± 0.2	0.9306	0.0159	0.0033	0.1103	0.0036	0.0783	0.0010	0.0022	0.0010	$3\omega_r$, $\Omega-3\omega_r$, $2\Omega-2\omega_r$; Axial motion not significant
		0.1	R	101.1 ± 0.2	1.2187	0.0111	0.0023	0.0716	0.0039	0.0431	0.0009	0.0017	0.0010	$3\omega_r$, $\Omega-3\omega_r$, $2\Omega-2\omega_r$; Axial motion not significant
		1	R	101.2 ± 0.2	1.0590	0.0070	0.0022	0.0843	0.0198	0.0554	0.0010	0.0016	0.0010	$3\omega_r$, $\Omega-3\omega_r$, 2Ω; Axial motion not significant
		5	R	103.3 ± 0.4	0.9222	0.0030	0.0007	0.0833	0.1500	0.0581	0.0003	0.0016	0.0008	$3\omega_r$, $\Omega-3\omega_r$, 2Ω; Axial motion not significant
		10	R	108 ± 1	1.1814	0.0045	0.0011	0.0869	0.2124	0.0560	0.0007	0.0021	0.0008	$3\omega_r$, $\Omega-3\omega_r$, 2Ω; Axial motion not significant
Asymmetric (Ω = 1038 kHz)	Axial	0	R	63.5 ± 0.2	0.1530	-------	-------	0.0438	-------	0.0455	-------	0.0006	0.0005	Axial motion not significant
		0.01	R	63.5 ± 0.2	0.1294	0.0039	0.0003	0.0615	0.0013	0.0520	0.0002	0.0007	0.0005	$3\omega_r$
			Z	63.5 ± 0.2	0.2386	0.0026	0.0003	0.0707	-------	0.0536	0.0002	0.0008	0.0006	
		0.1	R	63.5 ± 0.2	0.1526	0.0256	0.0027	0.0391	0.0114	0.0422	0.0015	0.0006	0.0003	$2\Omega-2\omega_r$
			Z	63.5 ± 0.2	0.7590	0.0025	0.0004	0.0667	0.0001	0.0543	0.0002	0.0008	0.0005	
		1	R	63.6 ± 0.4	0.1370	0.2369	0.0320	0.0490	0.1417	0.0383	0.0196	0.0006	0.0004	$3\omega_r$, $4\omega_r$, $\Omega-4\omega_r$, $\Omega-3\omega_r$, $\Omega+3\omega_r$, $\Omega+4\omega_r$, $2\Omega-2\omega_r$
			Z	63.6 ± 0.4	2.5698	0.0029	0.0005	0.0487	0.0002	0.0381	0.0003	0.0006	0.0004	$3\omega_z$, $\Omega+3\omega_z$, $2\ \Omega-3\omega_z$
		5	R	64.3 ± 0.3	0.3930	0.1658	0.0589	0.0473	0.1675	0.0352	0.0272	0.0005	0.0003	$3\omega_r$, $4\omega_r$, $5\omega_r$, $6\omega_r$, $\Omega-6\omega_r$, $\Omega-5\omega_r$, $\Omega-4\omega_r$, $\Omega-3\omega_r$, $\Omega+3\omega_r$, $\Omega+4\omega_r$, $2\Omega-4\omega_r$, $2\Omega-3\omega_r$, $2\Omega-2\omega_r$
			Z	64.2 ± 0.3	5.8174	0.0018	0.0004	0.0513	0.0003	0.0478	0.0003	0.0007	0.0006	$3\omega_z$, $4\omega_z$, $5\omega_z$, $\Omega-5\omega_z$, $\Omega-4\omega_z$, $\Omega-3\omega_z$, $\Omega+3\omega_z$, $2\Omega-4\omega_z$

Table 2-2 Continued

	Initial Velocity	KE (eV)	Motion	ω_u (kHz)	Amplitude (mm)	Relative Amplitude to ω_u								Other Harmonics; Notes
						$2\omega_u$	$\Omega-2\omega_u$	$\Omega-\omega_u$	Ω	$\Omega+\omega_u$	$\Omega+2\omega_u$	$2\Omega-\omega_u$	$2\Omega+\omega_u$	
Asymmetric	Radial	0	R	63.5 ± 0.2	0.1820	-------	-------	0.0355	-------	0.0282	-------	0.0005	0.0004	Axial motion not significant
		0.01	R	63.6 ± 0.2	0.4723	0.0009	-------	0.0523	-------	0.0271	-------	0.0005	0.0004	Axial motion not significant
		0.1	R	63.6 ± 0.2	1.0538	0.0012	-------	0.0460	0.0002	0.0458	-------	0.0007	0.0004	$3\omega_r$, Axial motion not significant
		1	R	64.2 ± 0.2	2.9444	0.0022	-------	0.0494	0.0002	0.0380	-------	0.0006	0.0004	$3\omega_r$, $4\omega_r$, $\Omega+3\omega_r$, $2\Omega-4\omega_r$; Axial motion not significant
		5	R	67.0 ± 0.3	6.1957	0.0226	0.0015	0.0615	0.0035	0.0370	0.0014	0.0007	0.0005	$3\omega_r$, $4\omega_r$, $5\omega_r$, $6\omega_r$, $\Omega-7\omega_r$, $\Omega-6\omega_r$, $\Omega-5\omega_r$, $\Omega-4\omega_r$, $\Omega+3\omega_r$, $\Omega+4\omega_r$, $2\Omega-4\omega_r$; Axial motion not significant
	Tangential	0	R	63.5 ± 0.2	0.1782	0.0005	-------	0.0437	-------	0.0271	-------	0.0005	0.0004	Axial motion not significant
		0.01	R	63.5 ± 0.4	0.1245	-------	-------	0.0718	0.0022	0.0557	-------	0.0006	0.0005	Axial motion not significant
		0.1	R	63.7 ± 0.7	0.1410	-------	-------	0.0640	0.0261	0.0527	-------	0.0006	0.0007	2Ω; Axial motion not significant
		1	R	65.3 ± 0.7	0.3955	-------	-------	0.0497	0.0981	0.0379	-------	0.0008	0.0006	2Ω; Axial motion not significant
		10	R	78.2 ± 0.5	3.3007	0.0084	0.0013	0.0451	0.0738	0.0337	0.0007	0.0005	0.0003	$3\omega_r$, $\Omega-3\omega_r$, $\Omega+3\omega_r$, $4\omega_r$, $\Omega-4\omega_r$, 2Ω; Axial motion not significant
Simplified (Ω = 1140 kHz)	Radial	0	R	260.1 ± 0.3	0.1906	0.0008	0.0008	0.2505	0.0007	0.0993	0.0001	0.0117	0.0030	$3\omega_r$, $4\omega_r$; Axial motion not significant
		0.01	R	260.1 ± 0.2	0.1152	0.0006	0.0009	0.3191	0.0003	0.1249	-------	0.0119	0.0030	Axial motion not significant
		0.1	R	260.2 ± 0.3	0.1271	0.0015	0.0009	0.3193	0.0003	0.1039	-------	0.0153	0.0039	$3\omega_r$; Axial motion not significant
		1	R	260.3 ± 0.3	0.8237	0.0042	0.0036	0.2330	0.0015	0.0745	0.0003	0.0085	0.0026	$3\omega_r$, $\Omega-4\omega_r$, $\Omega-3\omega_r$, $\Omega+3\omega_r$, $2\Omega-3\omega_r$, $2\Omega-2\omega_r$; Axial motion not significant
		10	R	244.8 ± 0.3	1.7016	0.0266	0.0200	0.2436	0.0234	0.0911	0.0032	0.0099	0.0025	$3\omega_r$, $4\omega_r$, $5\omega_r$, $6\omega_r$, $\Omega-4\omega_r$, $\Omega-3\omega_r$, $\Omega+3\omega_r$, $2\Omega-7\omega_r$, $2\Omega-6\omega_r$, $2\Omega-5\omega_r$, $2\Omega-4\omega_r$, $2\Omega-3\omega_r$, $2\Omega-2\omega_r$; Axial motion not significant

Table 2-2 Continued

	Initial Velocity	KE (eV)	Motion	ω_u (kHz)	Amplitude (mm)	Relative Amplitude to ω_u							Other Harmonics; Notes
						$2\omega_u$	$\Omega-2\omega_u$	$\Omega-\omega_u$	Ω	$\Omega+\omega_u$	$\Omega+2\omega_u$	$2\Omega-\omega_u$	$2\Omega+\omega_u$	
Simplified	Axial	0	R	260.2 ± 0.2	0.1635	0.0012	0.0009	0.3498	0.0004	0.1369	0.0002	0.0121	0.0030	$3\omega_r$, $4\omega_r$; Axial motion not significant
		0.01	R	260.2 ± 0.2	0.1753	0.0011	0.0010	0.3285	0.0009	0.1164	-------	0.0128	0.0038	
			Z	260.0 ± 0.2	0.0664	0.0042	0.0036	0.3829	-------	0.1498	0.0007	0.0171	0.0043	$3\omega_z$, $4\omega_z$
		0.1	R	260.1 ± 0.2	0.1507	0.0012	0.0039	0.2514	0.0055	0.0989	0.0005	0.0118	0.0029	$3\omega_r$, $4\omega_r$, $\Omega-3\omega_r$
			Z	259.9 ± 0.2	0.2079	0.0043	0.0055	0.2512	-------	0.0990	0.0007	0.0120	0.0030	$\Omega-3\omega_z$, $\Omega+3\omega_z$, $2\Omega-2\omega_z$
		1	R	260.4 ± 0.3	0.2089	0.0018	0.0208	0.2517	0.0342	0.0987	0.0027	0.0120	0.0029	$3\omega_r$, $4\omega_r$, $5\omega_r$, $6\omega_r$, $7\omega_r$, $\Omega-4\omega_r$, $\Omega-3\omega_r$
			Z	259.6 ± 0.3	0.8717	0.0026	0.0036	0.2521	-------	0.0981	0.0006	0.0120	0.0028	$3\omega_z$, $\Omega-4\omega_z$, $\Omega-3\omega_z$, $\Omega+3\omega_z$, $2\Omega-3\omega_z$, $2\Omega-2\omega_z$
		10	R	275.0 ± 0.3	0.2286	0.0013	0.0003	0.2417	0.1405	0.0892	0.0001	0.0126	0.0035	Many harmonics
			Z	235.6 ± 0.3	3.3690	0.0005	0.0002	0.0191	0.0002	0.0981	0.0002	0.0008	0.0024	Many harmonics
	Tangential	0	R	260.2 ± 0.2	0.1635	0.0012	0.0009	0.3498	0.0004	0.1369	-------	0.0121	0.0030	$3\omega_r$, $4\omega_r$; Axial motion not significant
		0.01	R	260.2 ± 0.2	0.2301	0.0011	0.0010	0.2522	0.0002	0.0987	0.0001	0.0119	0.0030	$\Omega-3\omega_r$, Axial motion not significant
		0.1	R	260.3 ± 0.2	0.1816	0.0012	0.0013	0.2535	0.0033	0.0983	-------	0.0122	0.0029	Axial motion not significant
		1	R	262 ± 3	0.2740	0.0013	0.0013	0.2332	0.0158	0.0918	0.0002	0.0120	0.0030	$3\omega_r$, $\Omega-3\omega_r$, $\Omega+3\omega_r$, 2Ω; Axial motion not significant
		10	R	264.1 ± 0.2	0.3791	0.0016	0.0022	0.2755	0.1277	0.0958	0.0003	0.0104	0.0033	2Ω; Axial motion not significant

By applying minimal initial velocity to the ion, different frequency patterns were seen in each of the toroidal ion traps within the range of 0−2.2 MHz while the ion motion was confined near the trapping center (see Figure 2-4). All three designs included the frequencies ω_u, $\Omega \pm \omega_u$, and $2\Omega \pm \omega_u$ in both axial and radial motion as expected for 2nd order fields. In the symmetric toroidal ion trap at 500 $V_{0\text{-}p}$ (Figure 2-4 (a) and (b)), the frequencies of the axial (direction of ejection) motion included series of higher harmonic sidebands of $n\omega_z$, $\Omega \pm n\omega_z$, and $2\Omega - 2\omega_z$; the frequencies of the radial motion showed the sidebands of Ω, $n\omega_r$, $\Omega \pm n\omega_r$, and $2\Omega - 2\omega_r$. These frequencies indicate the presence of odd-ordered field components. In the asymmetric toroidal ion trap at 500 $V_{0\text{-}p}$ (Figure 2-4 (c) and (d)), the axial (direction of ejection) motion included a small amount of $2\omega_z$ and $\Omega \pm 2\omega_z$, and no additional frequencies were seen in the radial motion. This observation indicates a low level of odd-ordered field contributions. In the simplified toroidal ion trap at 500 $V_{0\text{-}p}$ (Figure 2-4 (e) and (f)), the radial (direction of ejection) motion exhibited Ω, $n\omega_r$, $\Omega \pm n\omega_r$, and the axial motion showed $n\omega_z$, $\Omega \pm 2\omega_z$, and $2\Omega - 2\omega_z$. The magnitude of these frequencies was less than that in the symmetric toroidal ion trap but more than that in the asymmetric toroidal ion trap; this indicates that the effect of odd-ordered field contributions for the simplified toroidal ion trap is between that of the symmetric and asymmetric toroidal ion trap designs. To compare the ion motion with equivalent q-stability, RF amplitude changed in the symmetric and asymmetric toroidal ion traps to match the simplified toroidal ion trap. In the symmetric toroidal ion trap at 810 $V_{0\text{-}p}$ (Figure 2-4 (g) and (h)), there were no additional frequencies seen in the axial and radial directions besides ω_u, $\Omega \pm \omega_u$, and $2\Omega \pm \omega_u$. In the asymmetric toroidal ion trap at 1650 $V_{0\text{-}p}$ (Figure 2-4 (c) and (d)), there were harmonic sidebands of $n\omega_z$, $\Omega \pm 2\omega_z$, and $2\Omega - 2\omega_z$ in the0020axial motion, but no additional frequencies in the radial motion.

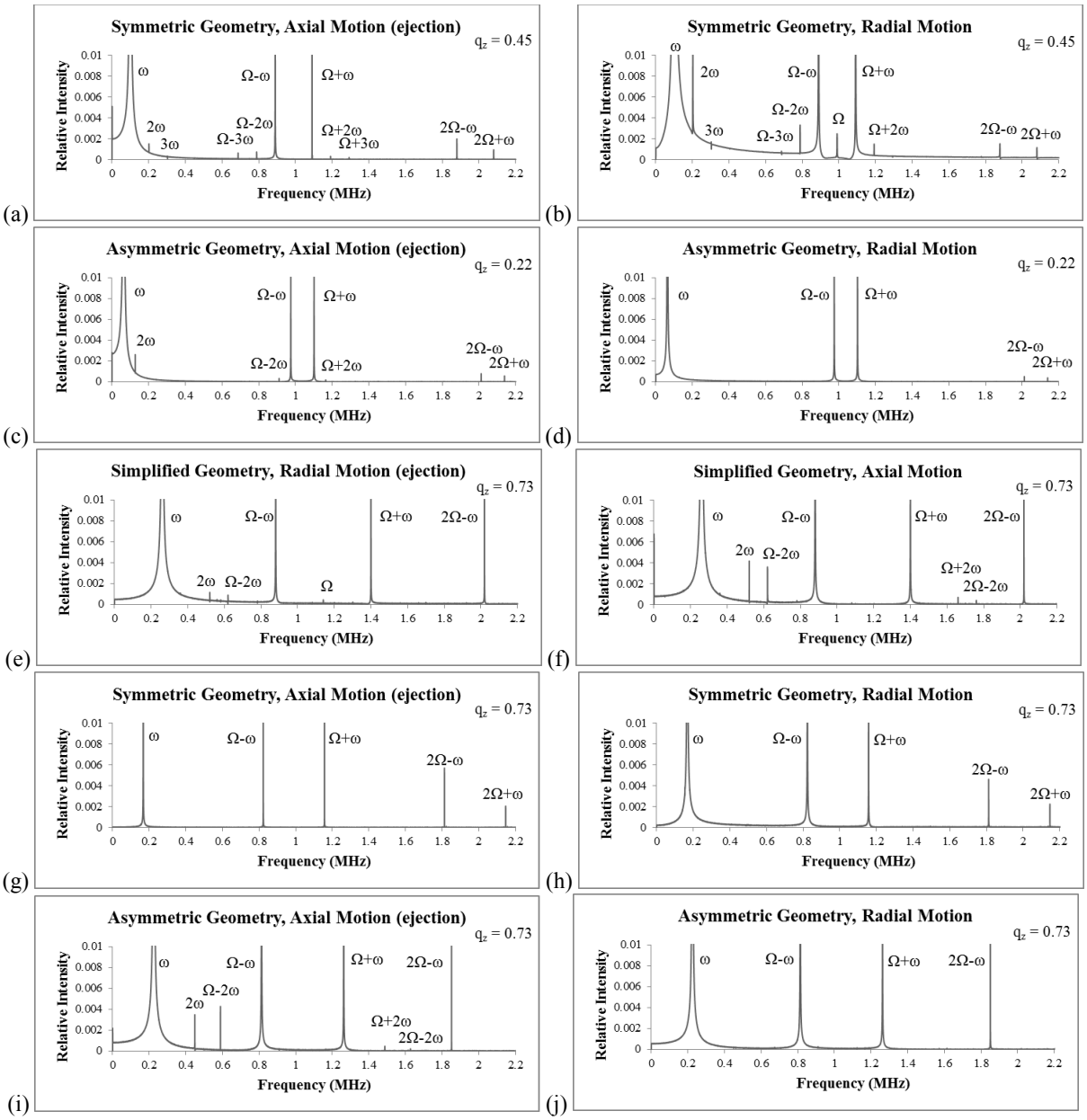

Figure 2-4: Frequencies of motion with minimal initial KE for the plane of ejection (a), (c), (e), (g), and (i) and perpendicular (b), (d), (f), (h), and (j). The ion used was *m/z* 100. The RF voltage was 500 $V_{0\text{-}p}$ for (a)-(f). To compare motion where the ion has the same *q*-stability as in the simplified toroidal ion trap, the RF voltage was 81 $V_{0\text{-}p}$ for (g)-(h) and 1650 $V_{0\text{-}p}$ for (i)-(j). The frequencies used were 0.990 MHz, 1.038 MHz, and 1.14 MHz for the symmetric, asymmetric, and simplified toroidal ion traps, respectively.

Increasing the velocity of an ion in the ejection plane (axial for the symmetric and asymmetric designs, radial for the simplified design) doesn't affect the amount of sideband

frequencies seen except at high initial kinetic energy (KE ≥ 5 eV) for the symmetric and simplified toroidal ion traps. For the symmetric toroidal ion trap, this contributes little effect to the frequencies of motion observed and their amplitudes in both the axial and radial direction except when the initial kinetic energy is ≥ 1 eV, as seen in Table 2-2. At high initial velocities, the frequency ω_z increases while the frequency ω_r decreases. There is also a change in the amplitude of motion. When the initial kinetic energy is 10 eV, the amplitude spectra in both directions become more complicated. This occurs because with higher velocity, the ion can be more displaced from the trapping center and is more susceptible to the field imperfections at the edges of the trapping space. These observations of coupling demonstrate the effects of the higher-order fields present in the symmetric toroidal ion trap. Increasing the initial axial velocity for the asymmetric toroidal ion trap contributes little effect to the relative intensities of the frequencies of the axial motion, but the relative intensities of the even harmonics of the radial motion increase as seen in Table 2-2. At initial kinetic energy of 1 eV, more harmonics appear in the axial motion, and the radial motion shows higher relative intensity of the harmonic frequencies. Also, the frequencies ω_z and ω_r only increase slightly when the initial kinetic energy is 5 eV showing that there is very little coupling expressed here. Increasing the radial velocity for the simplified toroidal ion trap to high kinetic energy (KE ≥ 1 eV) increases the relative intensity of the Ω and harmonic sideband frequencies as seen in Table 2-2. At 1 eV, a few harmonics emerge. At 10 eV, the frequency ω_r is decreased with the addition of several more harmonics.

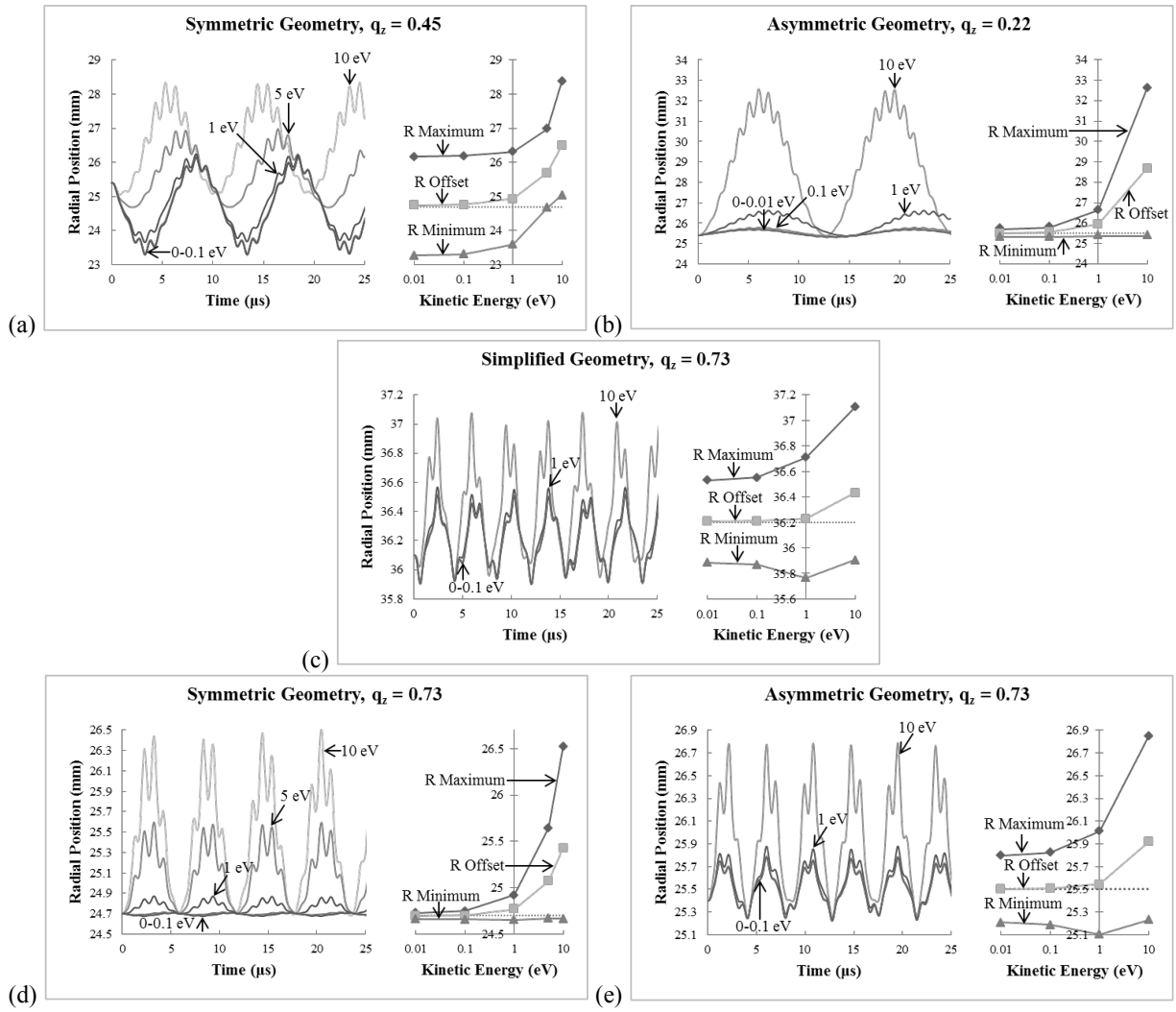

Figure 2-5: Effects of tangential velocity on the ion position in the absence of background gas for the (a) and (d) symmetric, (b) and (e) asymmetric, and (c) simplified toroidal ion traps with initial tangential velocity of varying kinetic energy. As the ion motion shifts outward with increasing kinetic energy, there are changes in the ion's micromotion. Each trap shows different trends in ion position with increasing kinetic energy. The saddle points for the symmetric, asymmetric, and simplified toroidal ion traps are 24.7 mm, 25.5 mm, and 36.2 mm, respectively. The ion used was *m/z* 100. The RF voltage was 500 $V_{0\text{-}p}$ for (a)-(c). To compare motion where the ion has the same *q*-stability as in the simplified toroidal ion trap, the RF voltage was 81 $V_{0\text{-}p}$ for (d) and 1650 $V_{0\text{-}p}$ for (e). The frequencies used were 0.990 MHz, 1.038 MHz, and 1.14 MHz for the symmetric, asymmetric, and simplified toroidal ion traps, respectively.

Increasing the velocity of an ion in the plane perpendicular to the plane of ejection (radial for the symmetric and asymmetric designs, axial for the simplified design) can slightly increase

the relative intensities of the sideband frequencies. For the symmetric toroidal ion trap, this increases the relative intensities of the harmonic sidebands of the radial motion only at high kinetic energies (KE > 1 eV) as seen in Table 2-2. At 10 eV, the frequency of radial motion is increased and many harmonics can be identified. Increasing the radial velocity for the asymmetric toroidal ion trap increases the amplitudes of $n\omega_r$ frequencies slightly as seen in Table 2-2. Also, as the kinetic energy increases, more harmonics can be identified, and the frequency ω_r starts to increase at kinetic energies ≥ 1 eV. Increasing the axial motion of the simplified toroidal ion trap increases the $n\omega_z$, $\Omega \pm n\omega_z$, and $2\Omega \pm n\omega_z$ axial frequencies and the Ω, $n\omega_r$, and $\Omega \pm n\omega_r$ radial frequencies, and more harmonics can be seen in the axial and radial directions as kinetic energy increases as seen in Table 2-2. At high kinetic energy (10 eV), the frequency ω_z decreases as the frequency ω_r increases, and the amplitude spectra also becomes complicated with multiple frequencies. These observations of coupling are similar to the coupling seen in the symmetric toroidal ion trap when axial velocity is applied to the ion.

Increasing the initial velocity of an ion tangentially to the major radius of the trap shows different effects than increasing axial or radial velocities. Increasing the initial tangential velocity for the symmetric toroidal ion trap increases the relative intensity of the Ω frequency and slightly decreases the relative intensity of the $\Omega \pm n\omega_r$ sidebands. At high tangential velocity (KE ≥ 5 eV), the frequency ω_r increases and the 2Ω frequency emerges. Increasing the initial tangential velocity for the asymmetric toroidal ion trap introduces and increases the Ω and 2Ω frequencies. At high velocities (KE ≥ 5 eV), the radial motion contains $n\omega_r$ and $\Omega \pm n\omega_r$ frequencies and the axial motion contains Ω, $n\omega_z$, and $\Omega \pm n\omega_z$ frequencies. Also, the frequency of radial secular motion increases at 10 eV as several harmonics emerge. Increasing the initial tangential velocity for the

simplified toroidal ion trap increases the Ω frequency in the radial motion and $2\omega_z$ and $2\Omega - \omega_z$ frequencies in the axial motion. The frequency ω_r starts to increase around 1 eV.

Also with initial tangential velocity, ion motion is shifted outward showing that the curvature of the trap causes the ion to experience a centripetal-like effect. Figure 2-5 shows the ion motion while increasing tangential velocity and compares the ion's average (offset), maximum, and minimum radial position in reference to the potential saddle point for the three toroidal ion trap designs. At very high tangential velocity (KE = 10 eV), the motion of the ion can become displaced from the saddle point. For the asymmetric toroidal ion trap, the amplitude of ion motion increases more drastically than in the symmetric toroidal ion trap. This change in amplitude affects the ion's maximum radial position more, and the minimum position does not seem to change as much. The simplified toroidal ion trap shows less outward shift than the other two designs. When the simulated ion has the same q-stability (Figure 2-5 (c)-(e)), there is less of an outward shift. This is interesting because the ion is closer to the β_z = 1.0 boundary. This effect demonstrates that the trapping center for an ion is dependent on its tangential velocity in the absence of collisions.

2.3.3 Simulated Ion Motion with Collisions.

With collisional cooling, the background gas can maintain a small range of kinetic energy. This effect dampens the motion of an ion with high kinetic energy and keeps the ion near the trapping center. As seen with previous trap designs, this is also true for toroidal ion traps including when an ion has high initial tangential velocity.

Table 2-3 shows the values for the average radial position, kinetic energy, collisional frequency, velocity, and mean free path for the three toroidal ion trap designs with background gas at 273 and 473 K.

Table 2-3: Average values of radial position, kinetic energy, collisional frequency, velocity, and mean free path at 1 mtorr (0.1333 Pa) with their respective standard deviations. The ion used was *m/z* 100. The RF voltage was 500 $V_{0\text{-}p}$. The frequencies used were 0.990 MHz, 1.038 MHz, and 1.14 MHz for the symmetric, asymmetric and simplified toroidal ion traps, respectively. Note that the collisional frequency and mean free path are calculated from how often the ion had a collision with a neutral molecule.

	Symmetric		Asymmetric		Simplified	
Temperature (K)	273	473	273	473	273	473
Radial Position (mm from axis of rotation)	24.698 ± 0.002	24.701 ± 0.002	25.505 ± 0.001	25.511 ± 0.005	36.2077 ± 0.0002	36.2073 ± 0.0004
Kinetic Energy (eV)	0.07 ± 0.01	0.10 ± 0.02	0.06 ± 0.02	0.10 ± 0.02	0.09 ± 0.02	0.15 ± 0.03
Velocity (mm/μs)	0.33 ± 0.02	0.42 ± 0.04	0.31 ± 0.03	0.38 ± 0.03	0.34 ± 0.02	0.48 ± 0.04
Collisional Frequency (μs^{-1})	0.064 ± 0.001	0.0430 ± 0.0006	0.0637 ± 0.0001	0.043 ± 0.001	0.0655 ± 0.0009	0.045 ± 0.003
Mean Free Path (mm)	5.08 ± 0.06	9.68 ± 0.09	4.85 ± 0.09	8.78 ± 0.08	5.24 ± 0.07	10.7 ± 0.3

The average radial position for each of the toroidal ion trap designs corresponds closely to the position of the saddle point (R = 24.7 mm for symmetric, R = 25.5 mm for asymmetric, and R = 36.2 mm for simplified). As the temperature increases, the average radial position of an ion is shifted slightly outward in the symmetric and the asymmetric toroidal ion traps; this change is larger for the asymmetric toroidal ion trap than the symmetric toroidal ion trap. This effect is not evident in the simplified toroidal ion trap even when considering the reduced standard deviation. This absent effect can be attributed to the larger major to minor radius ratio.

The average kinetic energy at 273 K is similar for an ion in the symmetric toroidal ion trap and in the asymmetric toroidal ion trap. This value for the simplified toroidal ion trap is greater because the minor radius (r_0 = 5.91 mm) here is smaller than that of the symmetric and

asymmetric designs (r_0 = 10. mm). This causes a greater q-stability parameter for the same *m/z* value in the simplified design as well as a greater β_z value closer to the ejection boundary. By increasing the temperature of the ion trap from 273 K to 473 K, the average kinetic energy increases by a factor of 1.4, 1.7, and 1.8 for the symmetric, asymmetric, and simplified toroidal ion traps, respectively.

With increasing temperature and kinetic energy, the average velocity of an ion increases and the collisional frequency decreases. For the symmetric, asymmetric, and simplified toroidal ion traps, the values for velocity increase by a factor of about 1.3, 1.2, and 1.4, respectively, by changing from 273 K to 473 K. The values of collisional frequency decrease by a factor of about 1.5 for each of the toroidal ion trap designs when changing the temperature from 273 K to 473 K. The overall effect of these changes increases the mean free path as expected by the collisional model used for the simulation; the values of the mean free path for the symmetric, asymmetric, and simplified toroidal ion traps increase by a factor of about 1.9, 1.8, and 2.0, respectively, by changing the temperature from 273 K to 473 K. These results may have implications for other curved devices, such as the C-trap used with commercial Orbitrap instruments [131].

2.4 Conclusion

This work used potential mapping, field calculations, and ion simulation to provide theoretical understanding of toroidal ion trap mass spectrometers. In observing higher-order fields, the asymmetric toroidal ion trap was shown to have the least amount of higher-order field effects of the three designs considered. While the simplified toroidal ion trap exhibited fields similar to the symmetric toroidal ion trap, its performance is still comparable to the asymmetric

toroidal ion trap. As more understanding of these toroidal designs becomes available, this knowledge can be utilized to evaluate not only miniaturized versions of toroidal ion traps but other curved quadrupolar devices as well.

3 RADIOFREQUENCY TRAPPING OF IONS IN A PURE TOROIDAL POTENTIAL DISTRIBUTION

(This chapter has been published as an article: "Higgs, J. M.; Petersen, B. V.; Lammert, S. A.; Warnick, K. F.; Austin, D. E. Radiofrequency trapping of ions in a pure toroidal potential distribution. International Journal of Mass Spectrometry. 2016, 395, 20–26." [132]. *My individual contribution was simulating ion motion within the calculated electrode shapes and writing the draft manuscript.)*

3.1 Introduction

Radiofrequency electric fields have been used to trap ions for many applications including spectroscopy, quantum computing, time and frequency metrology, and mass spectrometry. For example, trapped ions have enabled infrared spectra [36] and fluorescence measurements [37] to be obtained from molecular species using both a conventional Paul (quadrupole) trap and also a Paul-Straubel trap [133]. For quantum computing, trapped ions were used as quantum ion gates controlled by laser light [29] [30]. In improving frequency metrology, Be^+ ions have been trapped for a 303 MHz frequency standard [33]. Ion-neutral collisions were studied with a 22-pole trap and measured by a quadrupole mass spectrometer [134]. While higher-order multipole potentials such as the hexapole and octopole have been used for ion storage and ion transport (as, e.g., ion guides [46] [47]), they are not suitable as mass analyzers because of poor resolution [48] [49]. For this reason, only ion traps that are based on quadrupolar potentials have previously been or are currently used for mass analysis.

Quadrupole devices used in mass spectrometry come in two basic geometries depending on whether the potential varies quadratically in three or two dimensions. The former is the basis of quadrupole [20] and cylindrical [58] ion traps, and the latter forms the basis of linear [60] and rectilinear [59] ion traps. Another type of trapping device is the toroidal ion trap [61], which can be regarded either as a linear trap curved back onto itself to form a ring, or as a rotation of the cross section of a 3-dimensional quadrupole about an axis outside the trapping region (Figure 3-1).

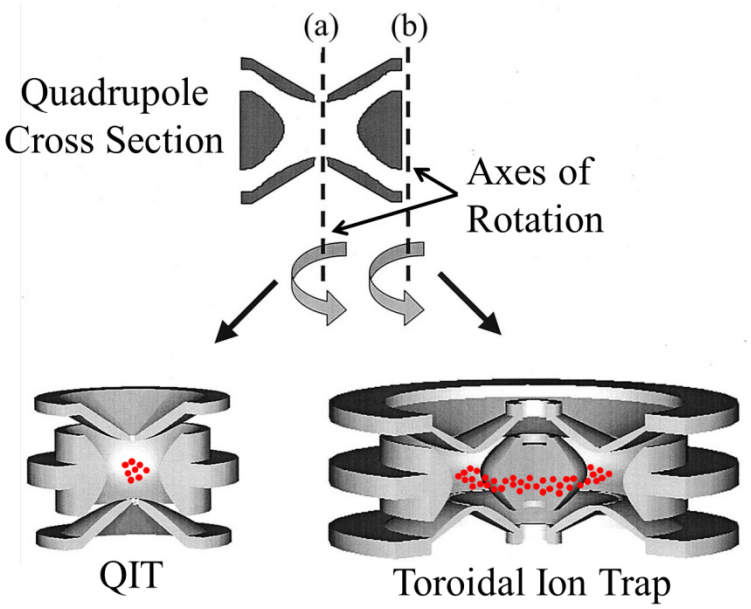

Figure 3-1: Comparison of the QIT and the toroidal ion trap. For the QIT, the rotational axis passes through the trapping center. For the toroidal ion trap, the rotational axis is offset to outside the trapping region. (Adapted from S. A. Lammert, W. R. Plass, C. V. Thompson and M. B. Wise, "Design, Optimization and Initial Performance of a Toroidal RF Ion Trap Mass Spectrometer," *Int. J. Mass Spectrom.*, vol. 212, pp. 25–40, 2001. [61])

A motivation behind the development of the toroidal ion trap [61] was to maintain a large trapping capacity in a device that would be miniaturized for portable mass spectrometry applications. In a toroidal trap, the trapping center is a ring, allowing more ions to be stored than in a conventional quadrupole ion trap (QIT), where the trapping center is just a point. The initial

report of the toroidal trap included two designs. The first had a cross section that was identical to the cross section of the QIT, but with an external rotational axis. However, this device, termed the "symmetric" toroidal ion trap, gave poor performance due to electric field perturbations resulting from the toroidal curvature. A second design remedied the curvature effects by using an asymmetric cross section—with different electrode asymptotes on the inner vs. outer electrodes. This geometric correction allowed mass resolution and accuracy similar to other ion traps. A miniaturized version of the asymmetric toroidal ion trap has now been used as the basis of a portable GC-MS system [98] [99]. Taylor and Austin [100] presented a simplified version of the toroidal ion trap using only cylindrical and planar electrodes which are easier to fabricate than hyperbolic electrodes.

Previously, we have reported simulation studies with the symmetric, asymmetric, and simplified designs for toroidal ion traps [122]. These simulations determined the electric fields in the trapping region as well as the effects of higher-order fields on ion motion. These results confirmed that the asymmetric design had the least amount of higher-order fields compared to the other two designs. The findings also showed that the fields of the simplified design more closely resemble that of the symmetric design even though its reported performance is closer to the asymmetric design.

However, it was also observed [122] [124] that neither the conventionally defined quadrupole nor Cartesian multipoles generally are adequate to completely describe the potentials in toroidal traps. If the potential distribution in a toroidal trap were quadrupolar, the potential must vary as the square of the distance from the trapping center. This would result in the following inconsistencies:

1. The potential cannot indefinitely increase quadratically because it will run into the rotational axis—at that point the potential would be non-differentiable;
2. Moving in any linear direction from the trapping center the potential will be perturbed by curvature effects;
3. There is no a priori reason for the multipoles to all be centered at the same radial distance (e.g., at the trapping center).

This first point may be considered by using the Poisson Equation for a closed volume with a contained charge (the central electrode), but the other two effects cannot be handled this way. The second point will be the case for all higher-order multipoles as well as the quadrupole. Thus the potential in a toroidal ion trap cannot be described by a quadrupole or by a sum of Cartesian multipoles except in the local vicinity of the trapping center.

It may be possible to evaluate the local field using a perturbation approach [135], but for a toroidal ion trap a solution based on a toroidal coordinate system may be more appropriate and useful. Any electric potential distribution in a closed volume must satisfy the Laplace equation, $\nabla^2\Phi = 0$. Conveniently, the Laplace equation has a separable solution in a toroidal coordinate system. In a rectangular geometry, the quadrupole field can be represented as a simple polynomial. The analogous toroidal quadrupole and higher-order solutions are given by a combination of hyperbolic trigonometric functions and associated Legendre functions. Despite their complexity, these functions can be evaluated using a suitable numerical programming package such as MATLAB (Mathworks, Inc.).

The first step in applying this model to the toroidal ion trap is to examine the behavior of ions in time-varying toroidal harmonic fields. In this paper, we use SIMION simulations to determine the behavior of ions in the toroidal harmonic most closely analogous to the

quadrupole. Specifically, we examine whether trapping is even possible, the conditions for trapping, and the resulting ion motion within the field.

3.2 Theory

The toroidal coordinate system (Figure 3-2) is defined in terms of three parameters, (σ, τ, ϕ), where τ is the natural logarithm of the ratio of the distances d_1 and d_2 from a given point to the nearest and farthest points on the focal ring with radius a, σ is the angle between these two lines d_1 and d_2, and ϕ is the azimuthal angle of the point in the plane of the defining circle [136]. The toroidal coordinates form an orthogonal coordinate system, with respect to which the Laplace equation is separable.

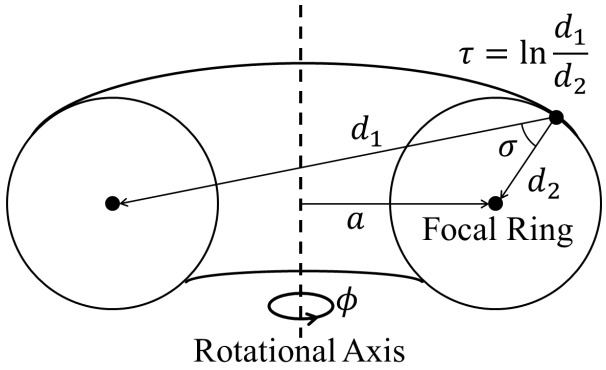

Figure 3-2: Toroidal coordinate system, (σ, τ, ϕ), with a torus containing a focal ring of radius a.

Because the toroidal coordinate system is separable, there is a complete family of solutions to Laplace equations that can be expressed in a product form. For the toroidal coordinate system, the separable solution has the form [137]

$$u(\sigma,\tau,\phi) = \sqrt{\cosh(\tau)-\cos(\sigma)}\, f(\sigma)g(\tau)h(\phi) \tag{3-1}$$

The factors are defined by

$$f(\sigma) = \cos(v\sigma) \text{ and } \sin(v\sigma) \tag{3-2}$$

$$g(\tau) = P^{\mu}_{v-\frac{1}{2}}(\cosh(\tau)) \text{ and } Q^{\mu}_{v-\frac{1}{2}}(\cosh(\tau)) \tag{3-3}$$

$$h(\phi) = \cos(\mu\phi) \text{ and } \sin(\mu\phi) \tag{3-4}$$

where $P^{\mu}_{v}(x)$ and $Q^{\mu}_{v}(x)$ are associated Legendre functions of the first and second kind, respectively, and v and μ are integers.

Some of the degrees of freedom in the general separable solution can be eliminated based on the configuration of typical ion traps. The first kind Legendre functions become infinite as τ approaches infinity, which occurs on the central circle of the toroidal geometry (the trapping center in the present study). These functions are not required when expanding fields in the interior of an ion trap, so only the second kind associated Legendre functions are used. We assume any device would be rotationally symmetric, so $\mu = 0$. With respect to the coordinate σ, the field distribution can be symmetric, $f(\sigma) = \cos(v\sigma)$, or antisymmetric, $f(\sigma) = \sin(v\sigma)$, or a combination of both terms. This symmetry corresponds to reflection of the plane containing the trapping center. The toroidal trap is axially symmetric, which means that the symmetric σ distribution would be chosen, but the antisymmetric σ distributions could be useful for certain effects such as excitation or ejection in the axial direction. The remaining parameter is the order of the toroidal harmonic $v = 0, 1, 2, \ldots$ and is analogous to the A_n term that defines the series of multipoles in conventional traps. Solutions to Laplace's equation of this separable form are referred to as toroidal harmonics or toroidal multipoles. The toroidal harmonics are calculated using the 'hypergeom' function in the MATLAB Symbolic Math toolbox based on an identity for the associated Legendre function in terms of the generalized hypergeometric function [137].

Figure 3-3 shows the symmetric and antisymmetric second kind toroidal harmonics of orders one to four [138]. The order one toroidal harmonic is analogous to a dipole field, but can be either radial or axial depending on whether the symmetric or antisymmetric σ distribution is considered. The second-order toroidal harmonic ($v = 2$) of the second kind has a behavior near the defining circle (the trapping center) that is analogous to the quadrupole potential used in linear ion traps and quadrupole mass filters and similar to the potential near the trapping center of the toroidal ion trap. However, this second-order solution also exists as symmetric or antisymmetric forms, as shown in Figure 3-3. This symmetric solution, hereinafter referred to simply as the "toroidal quadrupole," will be used for all simulations in the present work. Higher order toroidal harmonics correspond to more complex variations of the electric fields, and may be useful to adjust the trapping potential as the octopole and other multipoles are used on conventional traps. The existence of both symmetric and antisymmetric solutions add a new flavor to the mix and may be useful in trapping and analyzing ions. Note that the geometry of this toroidal quadrupole is significantly different from any reported toroidal ion trap. The toroidal quadrupole is simply a theoretical construct representing a single solution to the Laplace Equation in toroidal coordinates.

3.3 Methods

Simulations of ion motion within the toroidal quadrupole (with applied RF) were performed using SIMION 8.0. Simulations included the following: observing the parameters affecting trapping, mapping a stability diagram, frequency analysis of ion secular motion, and modeling the effect of collisions with background gas.

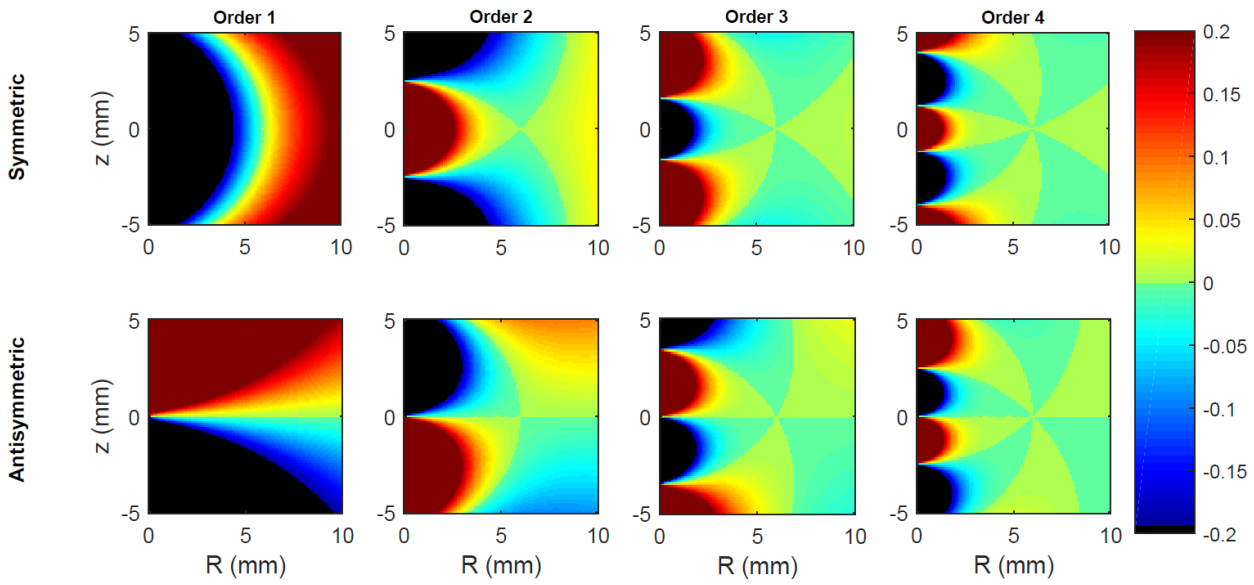

Figure 3-3: Symmetric and antisymmetric toroidal harmonics of the second kind.

The potential distribution representing the toroidal quadrupole (Figure 3-4) was determined using Matlab and input into SIMION using a geometry file. Matching isopotential surfaces (positive and negative relative to the trapping center) were selected to represent electrodes (Figure 3-4 (a)). The SIMION potential array was 401 × 400 gu (grid units) in size with cylindrical symmetry. The scaling for the array was 0.05 mm/gu, the major radius (R_0) of the trapping center was 6.00 mm, and the trapping center was 2.05 mm from the central electrode, 4.00 mm from the outer electrode, and 2.90 mm from either of the axial electrodes as measured in the z direction. Because all toroidal surfaces are closed, it was possible to select the SIMION array size so that none of the electrodes required any truncation (Figure 3-4 (b) and (c)), something not possible with the Cartesian quadrupole or multipoles. The second kind associated Legendre function is singular at $\tau = 0$, which leads to a complicated behavior for equipotential surfaces near the z axis, but in a real device the electrode shape could be simplified or truncated with only a negligible effect on the potential behavior in the trapping region.

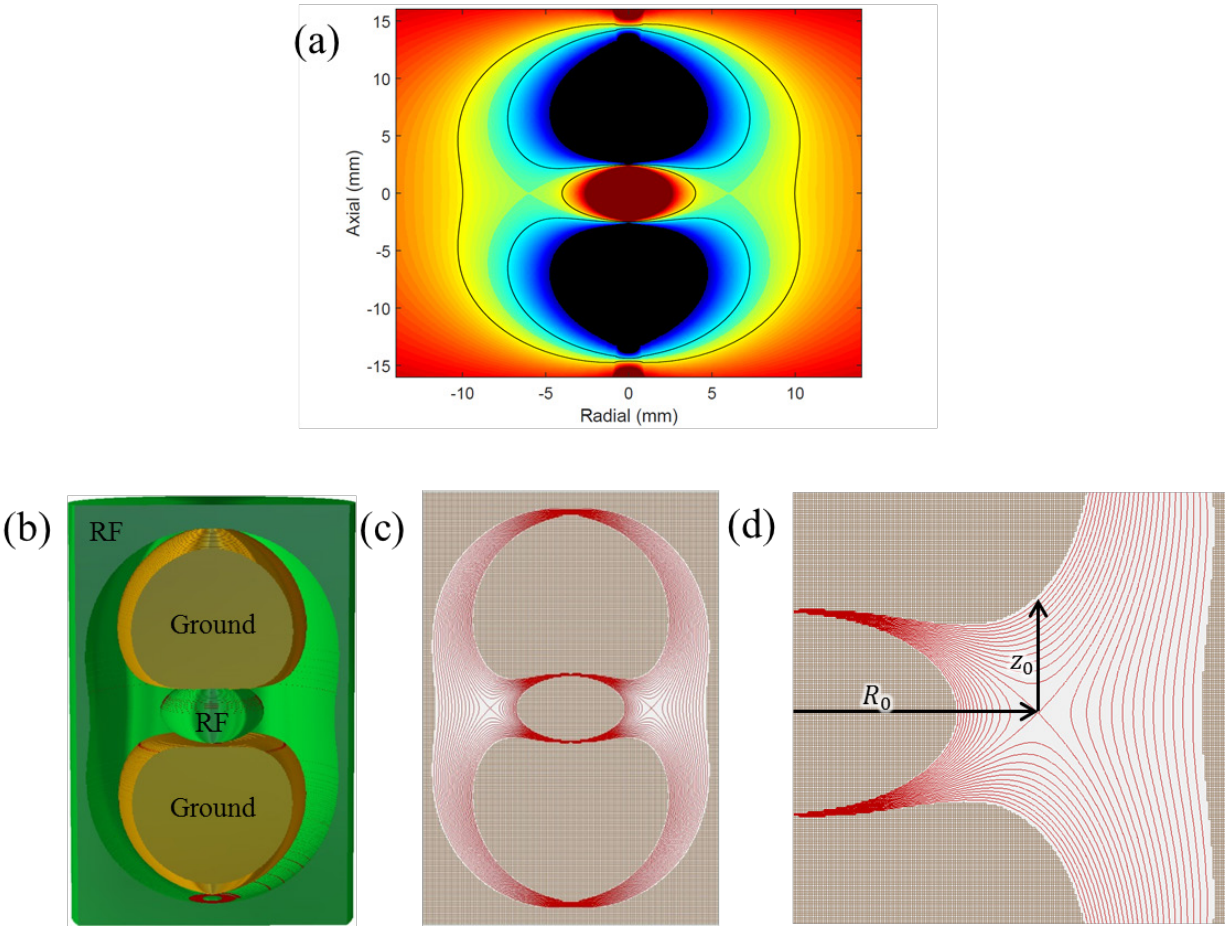

Figure 3-4: Isopotential contours and surfaces of the toroidal quadrupole: (a) the toroidal quadrupole potential, black lines indicating the isopotential surfaces chosen to be electrodes; (b) 3D representation of the electrodes; (c) cross-section of the electrodes with isopotential contour lines; (d) close-up view of the trapping region.

To compare with previous studies, the profile of the potential across the trapping region was calculated in the r and z directions (Figure 3-4 (d)), passing through the trapping center (R_0 = 6.00 mm, z = 0). Position was normalized relative to the major radius (R_0 = 6.00 mm) and distance between the axial electrodes (z_0 = 2.90 mm). The field along these lines was calculated by taking the derivative of the potential.

The example user programs for SIMION 8.0 were modified for these simulations. An RF frequency of 2.0 MHz was applied to the inner and outer radial electrodes with variable RF amplitude and DC offset. The electrodes were set to ground or RF as shown in Figure 3-4 (b). The potential energy surface of the electrodes was updated every 0.05 μs. For simulations considering ion-neutral collisions, a hard-sphere collision model was used at approximately 1 mtorr (1.33 Pa) with helium (4 amu) as the background gas. The user programs were modified to automatically run consecutive simulations over a range of parameters including the RF amplitude and DC offset.

Ion trajectory simulations used ions with *m/z* of 100, 200, or 300. All ions used are singly charged. Ion initial positions were set at the trapping center except for simulations that recorded the time the ion remained trapped with varying ion position. The RF phase and ion start time were set to 0 with no distribution. For convenience, the particle's initial kinetic energy was set to 0.1 eV, and the initial velocity was set to the axial direction. Additional simulations without collisions started the particle with 0 eV but offset from the trapping center. For simulations that included collision effects, the collision cross section of the particle was set to 2.27×10^{-18} m^2 and the temperature was 273 K.

The stability diagram was determined by changing the RF amplitude and DC offset between simulations. An ion was considered stable when its trapping exceeded 100 μs. When the ion was not stable, SIMION recorded which electrode the particle hit.

In order to monitor the frequencies of ion motion, the position of an *m/z* 100 ion was recorded while the RF amplitude was 200 $V_{0\text{-}p}$ and the DC offset was 0 V. MATLAB's Fourier function was used to convert the position of the particle with respect to time to an amplitude spectrum of the frequencies of motion.

3.4 Results and Discussion

3.4.1 Shape of the Trapping Potential and Electric Field.

Figure 3-5 (a) and (c) shows the potential in the radial direction along the $z = 0$ mm plane and in the axial direction along the $R_0 = 6.00$ mm cylinder. Note that the axial potential is measured in a straight line coincident with the trapping center and parallel to the rotational axis, and not along the curve of constant σ ($\sigma = \pi/2$). Figure 3-5 (b) and (d) shows the corresponding electric field. The radial direction exhibits a potential well that is skewed from the ideal parabolic shape. The radial field differs from that of a conventional quadrupole device because there is no region where the field is linear. The field here also has an asymmetric profile which is also the case with the symmetric and cylindrical toroidal ion traps [122]. Ion motion in the radial direction is expected to differ from simple harmonic motion because of these features. The potential in the axial direction is approximately parabolic with a linear range between $z = -0.2$ and 0.2. It is important to note that these potentials are derived from a pure toroidal harmonic and not from a device that is non-ideal due to truncation, electrode shape, or electrode position, as is usually the case when calculating potentials or fields to characterize device performance. The potential of the toroidal quadrupole is similar to, but not exactly the same as the Cartesian quadrupole. As such, the ion motion is expected to differ from that in a conventional quadrupole device.

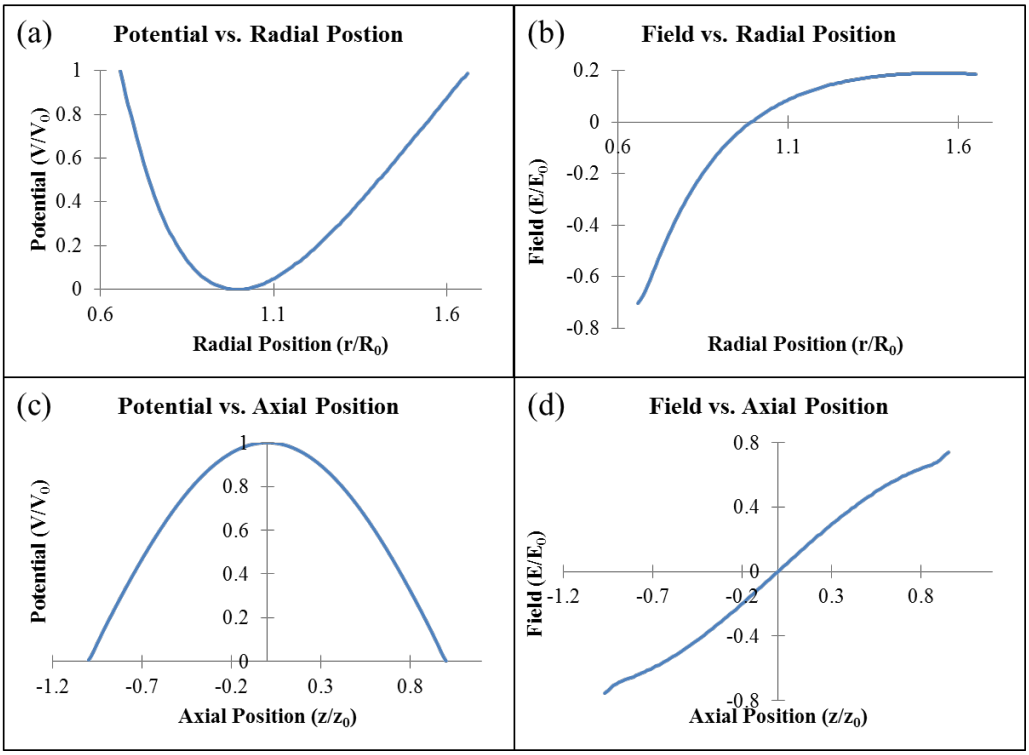

Figure 3-5: The potential and field across the trapping region crossing at (a and b) z = 0 mm radially and (c and d) R_0 = 6.00 mm axially.

3.4.2 Stability of ions in the toroidal quadrupole.

Simulations compared the length of time an ion can be trapped as a function of RF amplitude for both the toroidal quadrupole and a conventional (Cartesian) quadrupole in the absence of background gas. The results, shown in Figure 3-6, show that ion trapping time is nearly equivalent between the two types of traps, with a few notable differences. The toroidal quadrupole shows a narrow region with significantly reduced trapping time at RF voltages roughly 0.85 time the voltage representing the boundary. The trapping time at very low RF amplitudes also differs between the two traps: trapping times in the toroidal quadrupole start to increase at the same voltage as the QIT, but then plateau briefly before jumping to the maximum value. At a few specific RF amplitudes the QIT shows sharp features with trapping time >10 s; such features are

absent in the toroidal quadrupole. Note that the *m/z* used in the Cartesian quadrupole simulation was chosen so that the boundary occurs at the same RF amplitude in both cases.

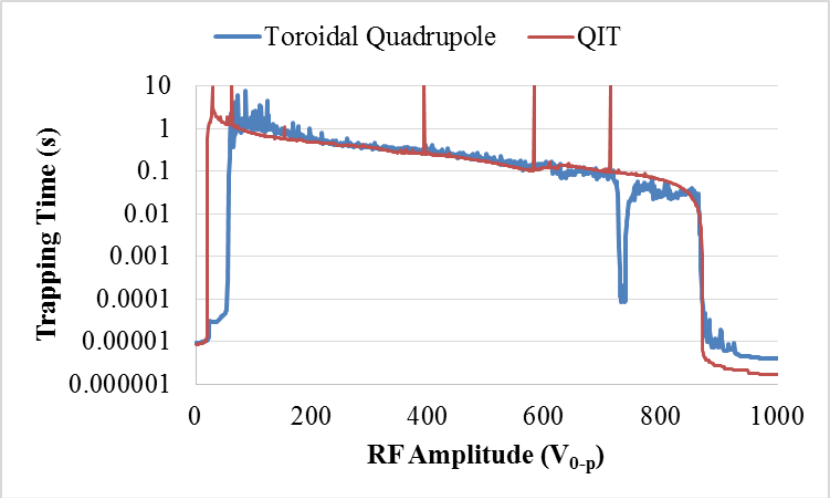

Figure 3-6: Ion trapping time as a function of RF amplitude and initial ion position for the toroidal quadrupole and the QIT. For the toroidal quadrupole, the ion (*m/z* 200) started at the trapping center (z = 0 mm and R_0 = 6.00 mm) with 0.1 eV applied to initial axial velocity. For the QIT, the ion (*m/z* 164) started at the trapping center (z = 0 mm and r = 0 mm) with the same initial kinetic energy. The DC offset was set to zero V for both traps. The ion *m/z* was normalized so that the boundary would fall at the same RF voltage. The trapping time was limited to 10 s.

Figure 3-7 (a) shows the stability region (trapping time > 100 μs) for ions of *m/z* 100, *m/z* 200, and *m/z* 300 in the absence of collisions. Figure 3-7 (b) shows the stability region for these same ions when considering collisions with 1 mtorr of helium at 273 K. When considering collisions, the stability region is widened presumably due to the dampened ion motion. Many of the features of the stability diagrams are persistent at different *m/z* values, but are not commonly seen on stability diagrams of other types of ion traps. The top and bottom and the right edges of the stability regions show some jaggedness, including an interesting, sharp incursion at the apex. These jagged features may inhibit the use of apex isolation and boundary ejection. There is also a

large chasm running through the stability region. In the absence of collisions, this chasm separates the stability diagram into two distinct regions. Collisions reduce the width of this chasm and provide a narrow region connecting the two portions of the stability region.

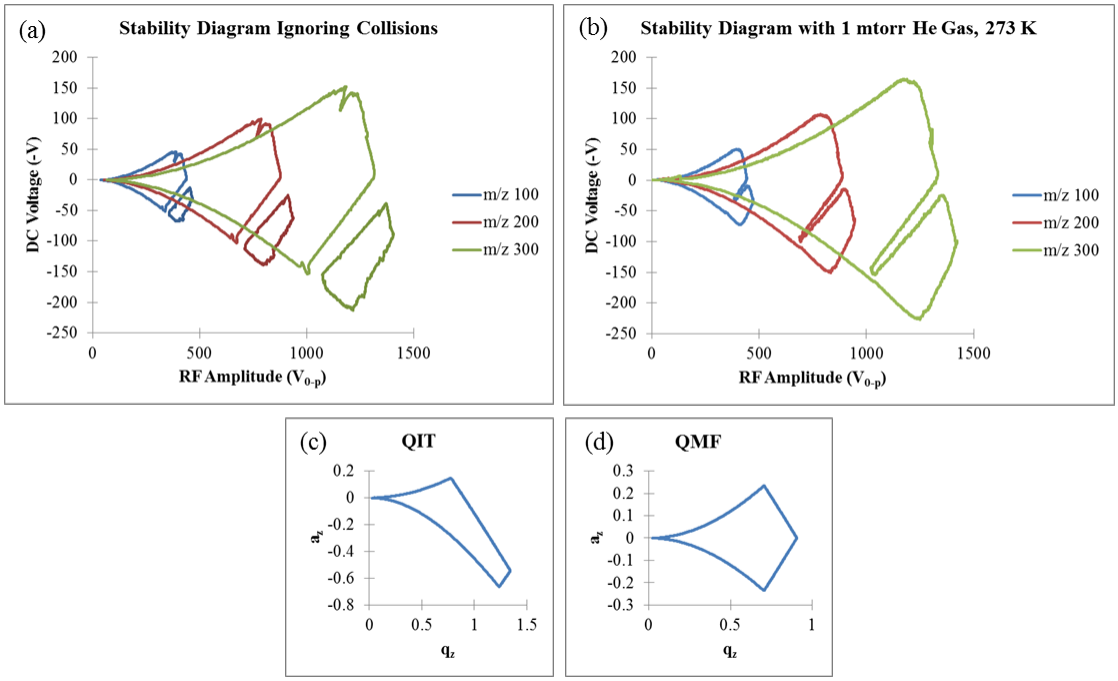

Figure 3-7: Stability diagrams for ions of *m/z* 100, *m/z* 200, and *m/z* 300 lasting at least 100 µs starting at z = 0 mm and R_0 = 6.00 mm with 0.1 eV applied to axial velocity (a) without collisions and (b) with collisions. For comparison, stability diagrams for the (c) QIT and (d) QMF are also included.

There are similarities between the general shapes of the toroidal stability diagram and those of the conventional QIT (Figure 3-7 (c)) and quadrupole mass filter (QMF) (Figure 3-7 (d)). The stability region of the toroidal quadrupole shows elongation that resembles the high-q, negative-a region of QIT stability, but the cut-off due to the chasm shows geometrical resemblance to the QMF stability. The similarities of this toroidal harmonic stability diagram to

both the QIT and the QMF imply that the toroidal quadrupole may exhibit aspects of both a 3D trap and a 2D trap.

Figure 3-8 shows the direction an ion of *m/z* 300 would be lost when not lasting 100 μs while ignoring collisions. There is a region above and to the left of the stability region that is dominated by inward radial losses while other areas are mostly outward radial losses. There are some boundaries of the stability region that are not sharp, in particular those at higher voltages. Using these regions for boundary ejection mass analysis would result in poor resolution similar to the conclusions made by Hägg and Szabo when investigating the use of hexapole and octopole fields for mass analysis [48] [49]. Because boundary ejection may not give the best performance for mass analysis, it may be beneficial to perform resonant ejection.

Figure 3-8 also shows a long, narrow incursion of instability originating midway up the right side of the stability region and intersecting the DC = 0 line at an RF amplitude 0.85 of the boundary. This incursion occurs at the same point as the drop in trapping time seen in Figure 3-6.

Finally, Figure 3-8 shows some additional regions where ions are stably trapped: a small, diffuse region to the right of the main stability region, and a pattern of several small, nebulous regions above the main stability region. These are not likely to be useful for ion trapping experiments, but it is interesting that they exist.

The left half of Figure 3-8 shows sharp stability boundaries and well-behaved ejection directions, similar to conventional ion traps. However, the diffuse boundaries on the right side of the figure correspond to a "chaotic" looking pattern of axial and radial (outward) ejection. The origin of this behavior is not clear.

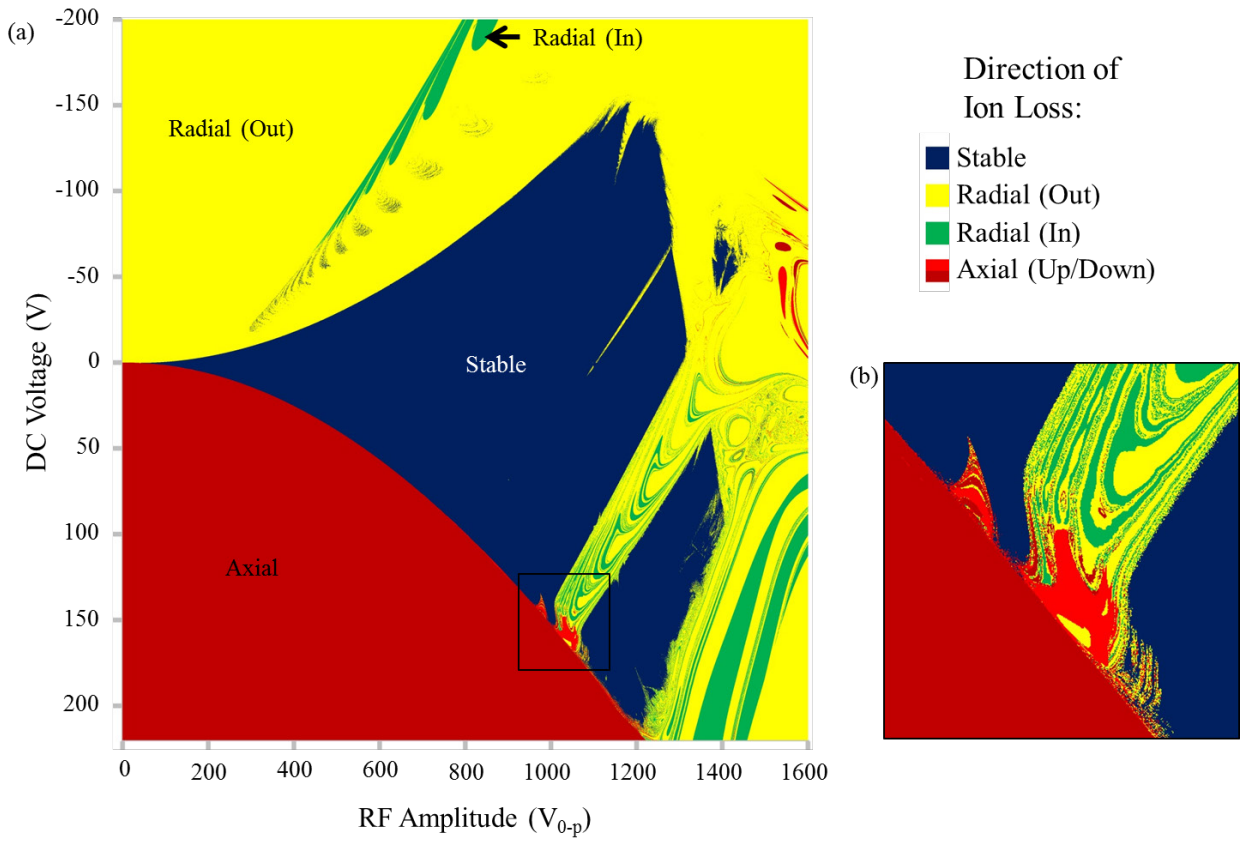

Figure 3-8: (a) Stability region of ions (*m/z* 300) in the toroidal quadrupole as a function of applied RF and DC voltages. For ions outside the regions of stability, the direction of ion loss is shown. (b) Magnification of the small region that contains part of the chasm. [Corrected figure.]

3.4.3 Ion Motion.

The frequency spectra of ion secular motion (Figure 3-9) show how the toroidal quadrupole field affects the ion motion. The secular frequencies of ω_r = 249.6 kHz and ω_z = 252.3 kHz had absolute amplitudes of 0.035166 mm and 0.212623 mm, respectively. In comparison with simulations of an ion of the same *m/z* value starting at the trapping center in existing toroidal ion traps [122], the ion motion has higher secular frequencies than in the symmetric (ω_r in the range of 100−117 kHz, ω_z in the range of 76−100 kHz) and asymmetric (ω_r in the range of 63−78 kHz, ω_z in the range of 63−64 kHz) toroidal ion traps but has close

values to that in the cylindrical toroidal ion trap (ω_r in the range of 244−278 kHz, ω_z in the range of 259−260 kHz). The radial secular frequency amplitude is much smaller in the toroidal quadrupole than in the three toroidal ion trap designs (symmetric: 0.8−1.2 mm, asymmetric: 0.15−0.18 mm, cylindrical: 0.16−0.19 mm). The axial secular frequency amplitude is similar to that in the symmetric (0.16 mm) and asymmetric (0.24 mm) toroidal ion trap designs, but it is also larger than that in the cylindrical toroidal ion trap (0.066 mm).

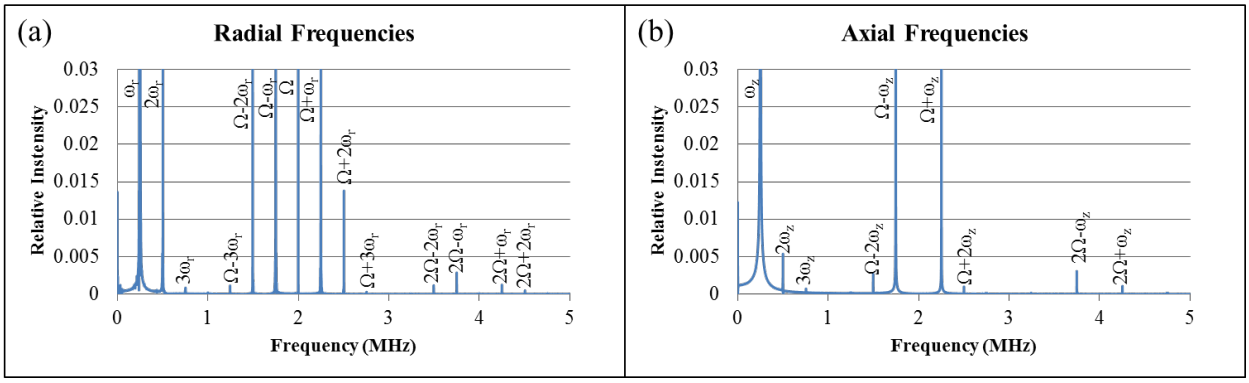

Figure 3-9: Frequency spectra of secular motion in the (a) radial and (b) axial directions for an ion of *m/z* 100 with RF amplitude of 200 $V_{0\text{-}p}$ and DC offset of 0 V.

The numbers of observed frequencies in ion motion and the relative amplitude of additional harmonics are greater in the toroidal quadrupole than in the existing toroidal ion trap designs. The identifiable harmonic frequencies of motion include $n\omega_r$, $\Omega \pm n\omega_r$, and $2\Omega \pm n\omega_r$ in the radial direction and $n\omega_z$, $\Omega \pm n\omega_z$, and $2\Omega \pm 2\omega_z$ in the axial direction. These frequencies could also be observed in the ion motion simulation for the symmetric toroidal ion trap, but there weren't as many seen in the asymmetric or the cylindrical toroidal ion trap designs.

3.5 Conclusion

These simulations show that ions can be trapped in a radiofrequency potential distribution corresponding to a toroidal harmonic, analogous to trapping in a quadrupole or other Cartesian multipole. The stability diagram for the quadrupole-like toroidal harmonic shows features that resemble the stability of both the 3-D quadrupole ion trap and the linear (2-D) quadrupole. Although the equations that have been developed for quadrupole devices cannot be readily applied to toroidal devices, a set of toroidal harmonics satisfies the Laplace equation and may be helpful. It is anticipated that these harmonics may provide the key to understanding and optimizing the performance of the toroidal ion trap. Future studies will explore other aspects of ion behavior in the toroidal harmonics, including mass analysis. The effects of higher-order toroidal harmonics will also be investigated.

4 FIELD OPTIMIZATION OF TOROIDAL ION TRAP MASS ANALYZERS USING TOROIDAL MULTIPOLES

(This chapter has been submitted for publication as an article: "Higgs, J. M.; Warnick, K. F.; Austin, D. E. Field Optimization of Toroidal Ion Trap Mass Analyzers Using Toroidal Multipoles. International Journal of Mass Spectrometry." My individual contribution was simulating ion motion within the calculated electrode shapes, processing the data, and writing the draft manuscript.)

4.1 Introduction

Ion traps use radiofrequency (RF) fields to trap ions for several purposes. For instance, spectroscopic studies have used ion traps to obtain spectra from ions in the gas phase [139] [140]. Quantum optics can observe fluorescence resulting from macroscopic quantum jumps of trapped ions [141]. Ion traps can also be used as logic gates for quantum computing [142]. Gas phase reactions involving trapped ions can explore pathways of collisionally induced dissociation (CID) reactions [143]. While these applications can use various ion trap designs, only devices based on a quadrupolar potential distribution have proven to be useful for mass analysis and mass spectrometry.

Paul [20] [62] developed the quadrupole ion trap (QIT) for ion storage and mass analysis. Various trap designs have been developed since then to accomplish increased ion capacity and/or ease in fabrication. The linear ion trap (LIT) confines the ions about a line as opposed to about a single point, thereby increasing the number of ions that can be trapped and analyzed [60]. The cylindrical ion trap (CIT) used cylindrical and planar electrodes, which are simpler to machine

than the hyperbolic electrode shapes of the QIT [58]. The rectilinear ion trap (RIT) also uses planar electrodes while also increasing the ion capacity like the LIT [59].

Lammert et al. [61] recently developed a toroidal ion trap to increase ion capacity by trapping the ions in a ring (or torus). They started with a "symmetric" toroidal ion trap design whose trapping region had the same cross section as the QIT. This design showed poor mass resolving power due to the fields introduced by the curvature of the trap. Another design, the "asymmetric" toroidal ion trap, adjusted the electrode shapes to have different asymptotic slopes for the central electrode and the outer ring electrode in order to correct the fields. This design has been miniaturized [98], and it has been used in a commercial, portable GC-MS system [99]. In 2012 Taylor and Austin [100] simplified the electrode shapes of the toroidal ion trap so that all the electrodes were cylindrical or planar, analogous to the CIT.

Simulations to quantify the fields and observe their effects on ion motion have been used for comparing performance and improving conventional ion trap designs. Fields that deviate from the linearity found in a perfect QIT can result from imperfections in the electrode shapes such as electrode truncation, exit slits, and manufacturing tolerances. These may have both beneficial and detrimental effects on the performance of the trap as a mass analyzer. For the QIT, CIT, LIT, and RIT, the trapping potential can be expressed as the sum of different multipole contributions added to the dominant quadrupolar potential. These contributions can be calculated by taking a high-ordered polynomial fit of the potential distribution where each term represents a specific multipole contribution (A_1: dipole, A_2: quadrupole, A_3: hexapole, A_4: octopole…) [125]. For ion traps with a toroidal geometry, this method is not mathematically valid [124]. To be defined as a quadrupole in a Cartesian coordinate system, the potential distribution must vary as the square of the distance from the trapping center. This is not possible in toroidal devices

because the potential cannot continue increasing when it meets the axis of rotation, and also because the potential does not increase quadratically when measured in a linear direction other than axially or radially.

In order to analyze the fields for these toroidal devices, we have previously compared the electric fields and simulated ion motion in three designs of ion traps: the symmetric toroidal ion trap, the asymmetric toroidal ion trap, and the cylindrical-electrode toroidal ion trap [122]. The study concluded that the asymmetric design had the best performance because its fields were closest to an ideal quadrupole. Interestingly, the cylindrical-electrode design had fields closer to that of the symmetric design even though its reported performance was as good as the asymmetric design. As an additional approach, we have also simulated ion motion in a potential distribution of a mathematically pure harmonic in a toroidal coordinate system [132]. After mapping the potential distributions of several of the orders of the symmetric toroidal harmonics of the second kind (Figure 4-1), we used the second order for simulations, referred to as the toroidal quadrupole. In the immediate vicinity of the trapping region, the potential of this toroidal quadrupole closely resembles the potential in a LIT. In mapping the stability diagram of this toroidal quadrupole, there were several resonance lines and jagged edges that would possibly make this design difficult to use in mass analysis. These resonance lines may correspond to those seen in QITs with significant higher order fields superimposed such as the hexapole and octopole.

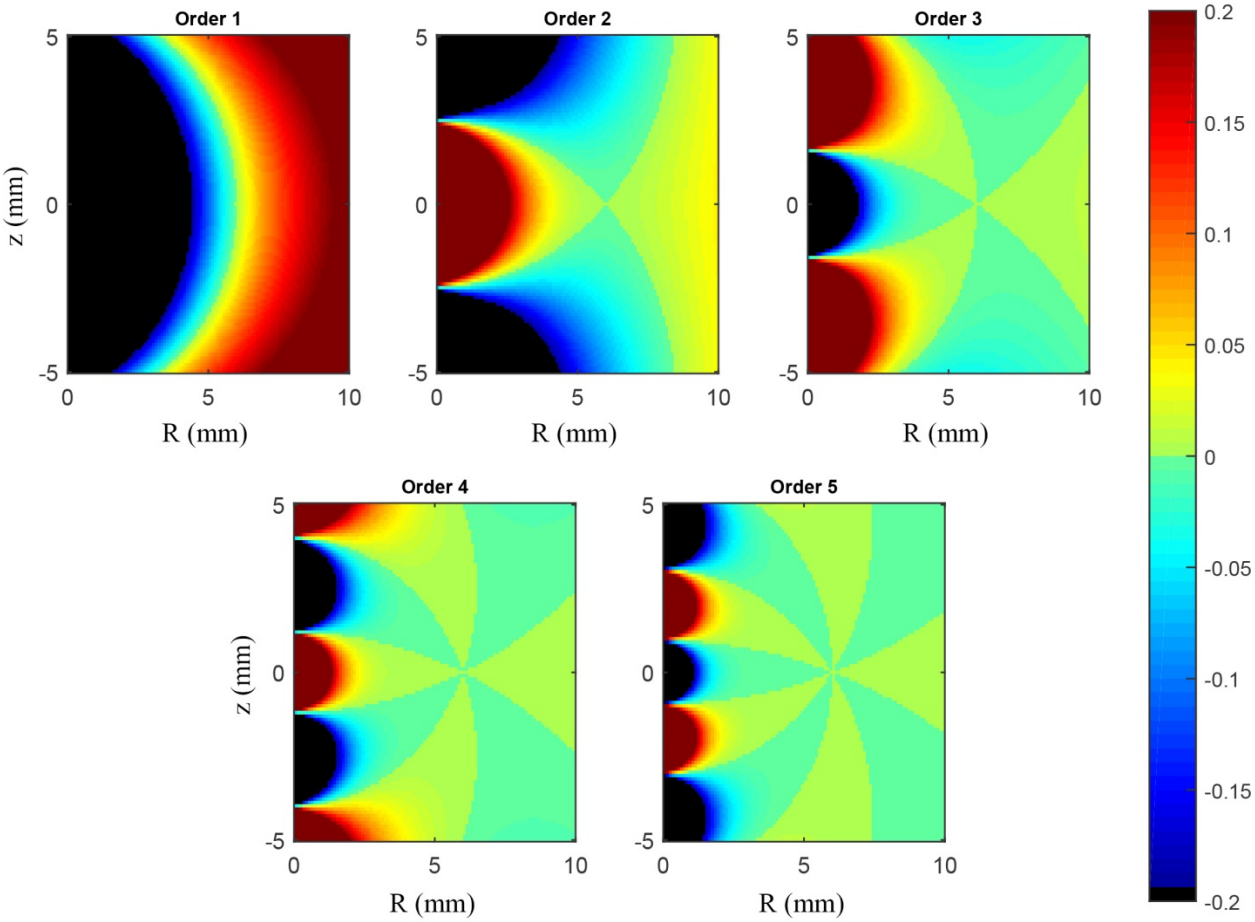

Figure 4-1: Symmetric toroidal harmonics of the second kind.

Kotana and Mohanty [144] used three methods of computing the multipole coefficients in a toroidal coordinate system for various ion traps of toroidal geometry, and all three methods gave similar results. They also presented Mathieu stability parameters and compared the secular frequencies of what they calculated and what they observed. Kotana and Mohanty [145] have also mapped out stability diagrams for the two toroidal ion trap designs first presented by Lammert's group. They found resonance lines at $\beta_r = ⅔$ and $\beta_r + 2\beta_z = 2$ (labeled as $\beta_z = ⅔$) with the stability diagrams of both designs and $\beta_r + \beta_z = 1$ for the symmetric toroidal ion trap. Lines like these are indicative of non-linear (higher-order) fields being present in the trap, and ions are ejected at the

resonance line rather than the boundary during mass analysis [45]. For the QIT, resonance lines at $\beta_z = ⅔$ and $2\beta_r + \beta_z = 2$ indicate the presence of hexapole contributions [45] [146].

Because the features seen in the stability diagrams of toroidal ion traps thus far show features indicative of higher-order fields, there must be a way to remove or reduce these features. For the commercial QIT, introducing positive even-order multipoles by spacing out the endcaps and stretching the trap corrected for the imperfections caused by the electrode truncation and exit slits and improved performance [45]. Numerous groups have optimized performance of other RF ion traps by manipulation of the higher order terms of the trapping potential [38] [25]. One example of this is the optimization of the CIT by adjusting the octopole and dodecapole field contributions [73]. As another example, the mass resolution for a quadrupole mass filter (QMF) was also improved when adjusting the hexapole and octopole field contributions [147]. If introducing some amounts of higher-order fields can improve the performance of conventional, Cartesian-coordinate traps, perhaps adding different amounts of higher-order fields for the toroidal coordinate to the toroidal quadrupole could improve its performance.

In this paper, we use contributions of different toroidal harmonic fields added to the toroidal quadrupole to observe changes in the features seen in the stability diagram. These simulations test whether the adverse features can be corrected or eliminated by addition of higher-order fields, thereby indicating a route to optimization of toroidal ion traps.

4.2 Theory

The toroidal coordinate system is defined by three parameters (σ, τ, ϕ) in relation to a focal ring of radius a. For a given point in a toroidal coordinate system, τ is the natural logarithm of the ratio of the lengths d_1 and d_2 of the lines from the point to the nearest and farthest points on the

focal ring, σ is the angle between these two lines, and ϕ is the azimuthal angle in the plane of the focal ring [136]. This coordinate system was described previously in relation to ion traps [132].

The separable solution of the Laplace equation in a toroidal coordinate system has the form [137]

$$u(\sigma,\tau,\phi) = \sqrt{\cosh(\tau)-\cos(\sigma)}\, f(\sigma)g(\tau)h(\phi) \tag{4-1}$$

The factors are defined by

$$f(\sigma) = \cos(v\sigma) \text{ and } \sin(v\sigma) \tag{4-2}$$

$$g(\tau) = P^{\mu}_{v-\frac{1}{2}}(\cosh(\tau)) \text{ and } Q^{\mu}_{v-\frac{1}{2}}(\cosh(\tau)) \tag{4-3}$$

$$h(\phi) = \cos(\mu\phi) \text{ and } \sin(\mu\phi) \tag{4-4}$$

where $P^{\mu}_{v-\frac{1}{2}}(x)$ and $Q^{\mu}_{v-\frac{1}{2}}(x)$ are the associated Legendre functions of the first and second kind, respectively, v represents the toroidal harmonic order for the solution and ranges from zero to infinity, and μ is an integer controlling the azimuthal variation of the harmonic. To make the solution symmetric above and below the trapping region, $f(\sigma)$ uses only the cosine function. Because the device geometry is rotationally symmetric, $\mu = 0$. The first kind Legendre functions are singular on the central circle of the toroidal trap, so we use only the second kind Legendre functions to expand fields in the trap.

The general solution for the field in the trapping region, with these symmetry conditions and discarding the order zero term, is given by the toroidal harmonic expansion

$$u(\sigma,\tau,\phi) = \sum_{v=1}^{\infty} A_v \sqrt{\cosh(\tau)-\cos(\sigma)}\cos(v\sigma)Q^{0}_{v-\frac{1}{2}}(\cosh(\tau)) \tag{4-5}$$

where the coefficient A_v represents the contribution of each v to the total potential distribution. These potential distributions can be calculated using the 'hypergeom' function in the MATLAB

Symbolic Math toolbox based on an identity for the associated Legendre function in terms of the generalized hypergeometric function [137].

4.3 Methods

4.3.1 Overview

Electrode arrays were calculated by varying the A_ν coefficient of different toroidal multipoles in relation to the toroidal quadrupole. The potential distributions for these arrays were mapped, and the calculated electric fields were compared. Simulated ion motion at certain ranges of RF amplitude and DC offset was used to map portions of the stability diagram that showed the jagged apex, the β_r = ½ resonance line, and the wide canyon at β_r = ⅔ in order to observe the effect that the additional multipoles had on these non-ideal features (Figure 2). These regions are potentially important for apex isolation, for containing product ions in a dissociation experiment, and for ion ejection using voltage or frequency scanning.

4.3.2 Electrode Array Calculations

The electrode arrays were calculated using MATLAB. Each array had different contributions of toroidal dipole (T1), hexapole (T3), octopole (T4), and decapole (T5) added to the toroidal quadrupole (T2) with A_2 = 1. The values of the A_ν coefficients of the added toroidal multipoles are given in Table 1. For values when A_ν = 0, the pure toroidal quadrupole was used. The electrode shapes for these combined distributions were selected by matching positive and negative isopotential lines (Supplemental Figure 4-1). The array with the toroidal dipole contribution used only A_1 = 0.25 because of the drastic changes to the electrode shapes with greater A_1 values as well as negative A_1 values. These arrays were then transferred to SIMION 8.0

where the potential distributions produced by the electrodes were recorded and ion motion was simulated with varying RF and DC voltages.

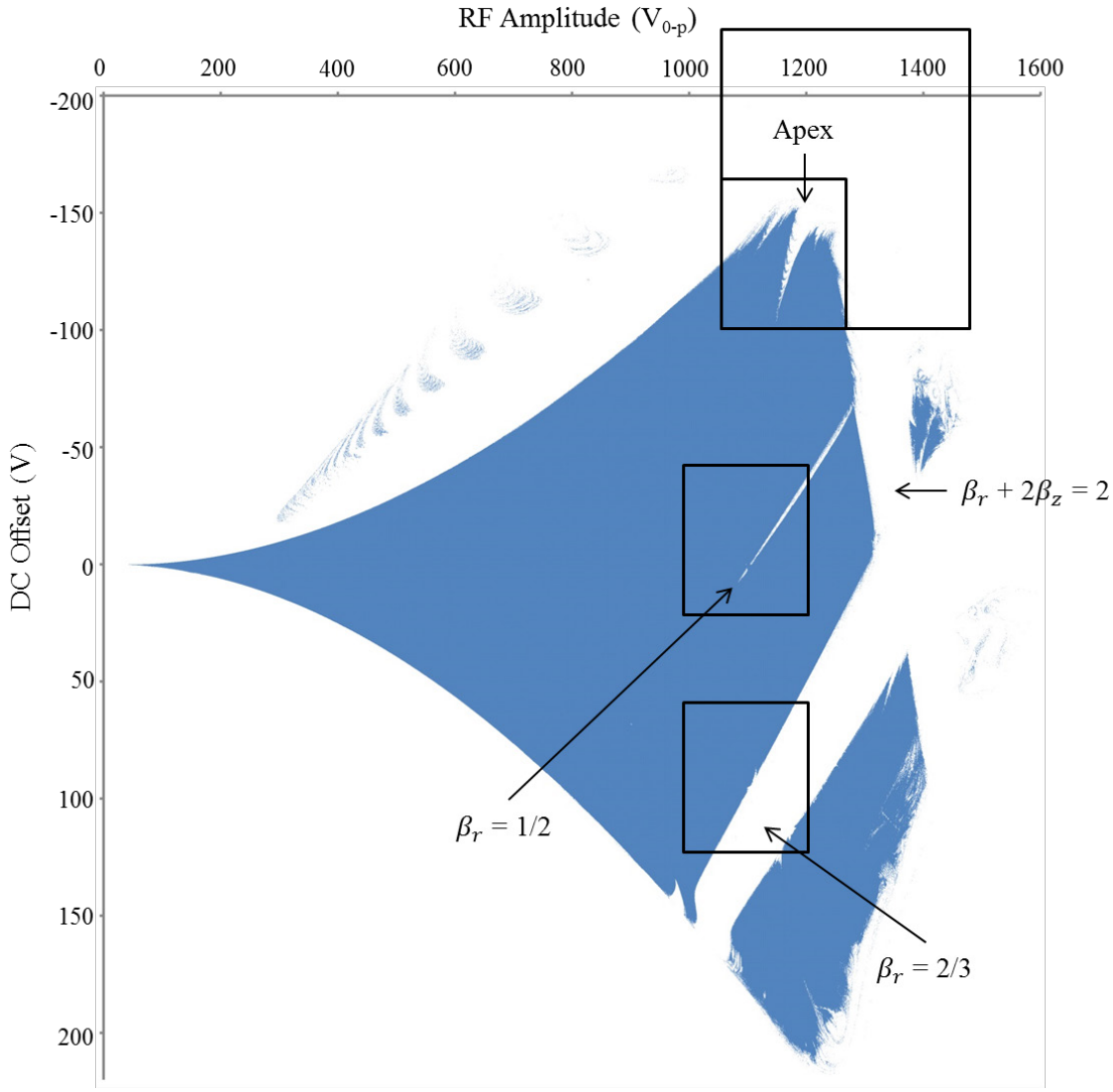

Figure 4-2: Stability diagram of the toroidal quadrupole for an ion of *m/z* 300. The apex and resonance lines $\beta_r = ½$, $\beta_r = ⅔$, and $\beta_r + 2\beta_z = 2$ are indicated. The boxes represent the voltage regions viewed. For the apex, the initial voltage ranges were RF amplitudes of 1050 to 1250 $V_{0\text{-}p}$ and DC offsets of –160 to 100 V, and the expanded voltage ranges were RF amplitudes of 1050 to 1450 $V_{0\text{-}p}$ and DC offsets of –220 to –100 V. For the $\beta_r = ½$ resonance line, the voltage ranges were RF amplitudes of 1000 to 1200 $V_{0\text{-}p}$ and DC offsets of –40 to 20 V. For the $\beta_r = ⅔$ resonance band, the voltage ranges were RF amplitudes of 1000 to 1200 $V_{0\text{-}p}$ and DC offsets of 60 to 120 V.

Table 4-1: Coefficients A_v added to a toroidal quadrupole with $A_2 = 1$. For values when $A_v = 0$, the pure toroidal quadrupole was used.

	A_v		
Harmonic	Minimum	Maximum	Step Size
Toroidal Dipole (T1)	0	0.25	0.25
Toroidal Hexapole (T3)	0	5	0.25
Toroidal Octopole (T4)	–4	0.5	0.5
Toroidal Decapole (T5)	0	5	1

4.3.3 SIMION

Each array was sized to 641 × 280 grid units (gu) with a cylindrical symmetry and a scaling of 0.05 mm/gu. The major radius of these trap designs was set to 6 mm.

The potential both radially and axially was recorded by flying a neutral particle passing through the saddle point. The field was calculated by taking the derivative of the potential distribution. The field was then compared to a linear field that was extrapolated from the points around the trapping center and the deviations from the extrapolated linear field were recorded as R^2 values.

For ion simulations, user programs were used to control the electrode voltages. The RF frequency was set to 2.0 MHz with a PE update of 0.05 μs. The RF amplitude and DC offset were determined by the region of the stability diagram observed. The ranges for these regions are indicated in Figure 2 with a step size of 0.5 $V_{0\text{-}p}$ for the RF and 0.125 V for the DC. These regions of interest include the apex, part of the resonance line at β_r = ½, and part of the wide canyon at β_r = ⅔. The values of the resonance lines and the wide canyon were calculated with the recorded secular frequency.

The simulations were performed with a singly-charged ion of *m/z* 300 with 0.1 eV kinetic energy applied to its axial velocity. The voltage settings were changed for each ion. An ion lasting at least 100 μs was considered stably trapped.

4.4 Results and Discussion

4.4.1 Analysis of Field Linearity

Analysis of the potential distribution of the pure toroidal quadrupole showed fields that were not perfectly linear as demonstrated previously [132]. This deviation from linearity is due to curvature effects. Most notably, the radial potential distribution had an asymmetric profile with a steeper distribution going towards the axis of rotation and a more gradual distribution going towards the outside of the trap. For ion traps with Cartesian-based geometries, a multipole expansion of the field could be used to compare linearity. In order to compare traps with toroidal fields, a Cartesian multipole expansion cannot account for asymmetries and curvature effects of the toroidal geometry. Instead, we used R^2 values comparing the axial and radial field components to a linear extrapolation of the field at the trapping center. The linearity of the radial and axial field components had R^2 values of 0.5233 and 0.9560, respectively. The values of linearity for the pure toroidal quadrupole and the other harmonic contributions are shown in Figure 4-3. For this case, term R^2 is a statistical measure of how close the calculated field is to the extrapolated linear field at the trapping center. R^2 values closer to 1.0 are considered to be more linear. Because the electrode shapes differed when adding multipole contributions to the quadrupole, the number of points used for the R^2 was not constant. For the pure quadrupole, 118 radial points and 121 axial points were used. In the axial direction, the restoring force does not point directly to the trapping center, hence

the calculated field component is not the same as the total field at those points. This is in contrast to ion traps with Cartesian geometries (QIT, LIT, etc.).

For the toroidal dipole, only the A_1 = 0.25 was studied. With this contribution, there was a shift in the radial position of the trapping center of about 2 mm. While there wasn't a noticeable difference in the linearity of the radial field (R^2 = 0.5241 with 89 points), the axial field's linearity increased to an R^2 value of 0.9998 with 45 points.

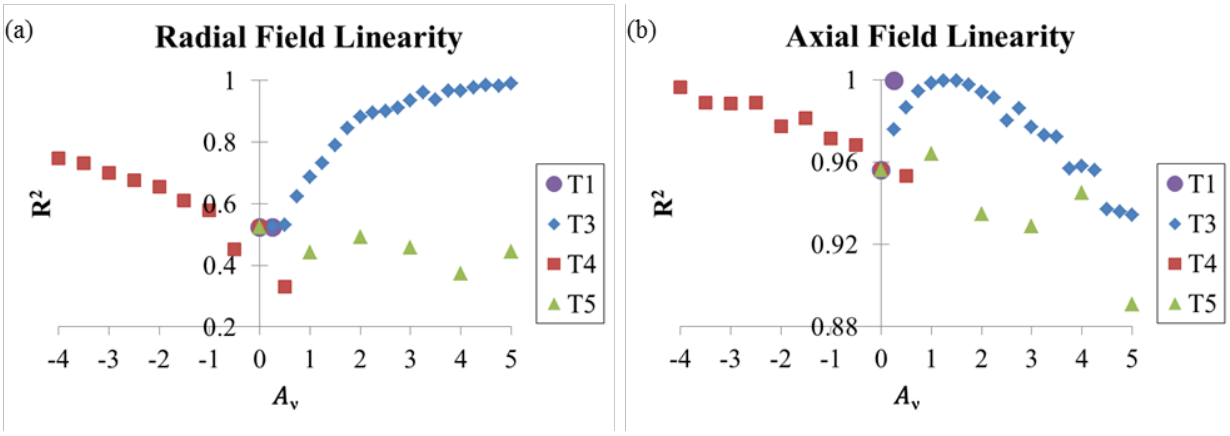

Figure 4-3: R^2 values for the field linearity in both radial (a) and axial (b) directions for traps with different A_v values added to the toroidal quadrupole. Circles represent the toroidal dipole (T1), diamonds represent the toroidal hexapole (T3), squares represent the toroidal octopole (T4), and triangles represent the toroidal decapole (T5).

When evaluating the fields of T3 contributions, there was a noticeable increase in the linearity of the radial field. The radial field linearity greatly increases when increasing the contribution from A_3 = 0 to 2, resulting in an R^2 value of 0.8820 with 75 points at A_3 = 2. The radial linearity increases at a slower rate with the contribution values of A_3 = 2 to 5, ending in a R^2 value of 0.9887 with 75 points. The axial field's linearity increased with the A_3 values up to

about 1.25 and then decreased after that point. The maximum R^2 value was 0.9997 with 98 points for A_3 = 1.25.

Increasing the negative toroidal octopole contribution also increased the linearity of the field. At A_4 = -4, the R^2 value for the radial field was 0.7481 with 92 points, and the R^2 value for the axial field was 0.9966 with 113 points.

For contributions of toroidal decapole, there was no clear trend in the R^2 values of the radial field, but the R^2 values appear to be decreasing slightly. For the axial field, there seems to be a trend of slightly decreasing R^2 values with increasing toroidal decapole contributions.

4.4.2 Toroidal Hexapole Contribution

The toroidal hexapole contributions caused the most change to the stability diagram. With additions of toroidal hexapole, the apex shifted enough to take it out of the initial region studied (Supplemental Figure 4-2). For these simulations, the region was expanded (Figure 4-2, larger box around apex) (Supplemental Figure 4-3). To quantify changes in the jagged features at the apex and to quantify changes in the ion ejection along the nonlinear resonance bands, we calculated the fraction (as a percentage) of stable points in the selected regions. We also calculated the fraction of stable points in an area corresponding to the extrapolated stability boundaries at the apex (Figure 4-4(a)). The β_z = 1 boundary was not seen in the voltage range viewed for A_3 values of 0 to 1 and of 5, so the fraction of stable points in the theoretical apex region was not calculated for these toroidal hexapole contributions. The A_3 value of 2.75 had the highest fraction of stable points with 38.66% of the total region and 99.13% of the theoretical apex region.

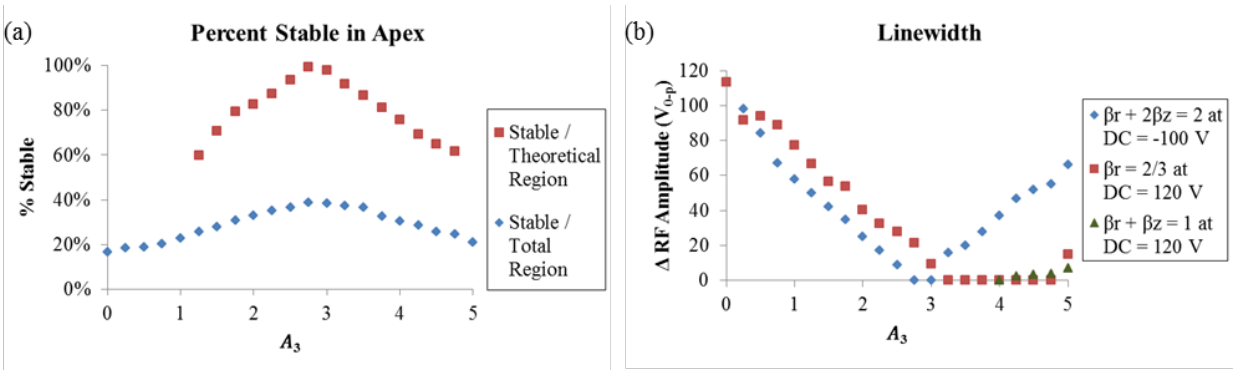

Figure 4-4: Effects of toroidal hexapole contribution to toroidal quadrupole in terms of A_3. (a) Percent stable points within the entire area scanned (diamonds) and within the theoretical region extrapolated from the $\beta_r = 0$ and $\beta_z = 1$ boundaries (squares). (b) Widths of resonance lines in term of ΔRF amplitude ($V_{0\text{-}p}$). The line $\beta_r + 2\beta_z = 2$ (diamonds) was measured at DC offset of –100 V, and the lines $\beta_r = ⅔$ (squares) and $\beta_r + \beta_z = 1$ (triangles) were measured at 120 V.

The jagged features at the apex decreased when the A_3 values varied from 0 to 2.75, and they increased A_3 values varied from 3 to 5. As the $\beta_r + 2\beta_z = 2$ resonance line decreased, the portion of the stability diagram on the right of this line became visible. We measured the width of this line at DC = –100 V (Figure 4-4(b)). The resonance line was no longer seen at DC = –100 V when the toroidal hexapole contribution was 2.75 and 3. For the contributions of 2.75 and 3, the resonance was seen to extend approximately 32 DC V and 52 DC V, respectively, from the stability diagram's apex. As the line increased at larger toroidal hexapole contributions, the portion on the right side of the resonance line diminished.

In the region with the $\beta_r = ½$ resonance line, the width of this line diminished with increasing toroidal hexapole contributions, and was outside the range by $A_3 = 1$ (Supplemental Figure 4-4). The higher toroidal hexapole contributions viewed did not show the line return.

In the region with the $\beta_r = ⅔$ resonance line, this resonance line diminished, disappeared by $A_3 = 3.5$, and started to reappear by $A_3 = 4.75$ (Figure 4-4(b)) (Supplemental Figure 4-5).

Also, the $\beta_r + \beta_z = 1$ resonance line appeared at $A_3 = 4.25$ and increased in size with increasing A_3. Figure 4-4(b) shows the width of the resonance lines at DC = 120 V for both the $\beta_r = ⅔$ and $\beta_r + \beta_z = 1$ resonance lines.

4.4.3 Toroidal Dipole, Octopole, and Decapole Contributions

The electrode geometry and stability diagram were very sensitive to the addition of toroidal dipole. For $A_1 = 0.25$, none of the ions within the specified voltage ranges were stable. In looking at the full range of the pure toroidal quadrupole stability diagram (RF amplitude = 0 to 1600 $V_{0\text{-}p}$, DC offset = –200 to 220 V), the stability diagram for the toroidal dipole contribution spanned less than half the voltage ranges of the pure toroidal quadrupole (RF amplitude = 0 to 700 $V_{0\text{-}p}$, DC offset = –70 to 90 V), and the area was only about one-sixth the size (Figure 4-5). In addition, the resonance lines at $\beta_r = ½$, $\beta_r = ⅔$, and $\beta_r + 2\beta_z = 2$ are narrower relative to the stability diagram, and additional stability regions are visible to the right of the $\beta_r + 2\beta_z = 2$ resonance line.

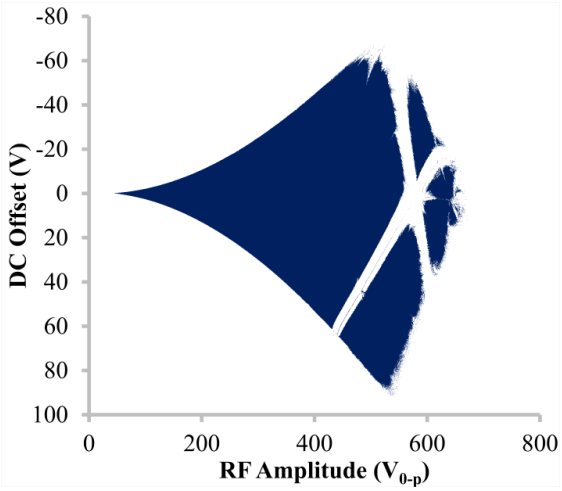

Figure 4-5: Stability diagram of $A_1 = 0.25$ added to the toroidal quadrupole. Note that this stability diagram is significantly smaller than that of the pure toroidal quadrupole.

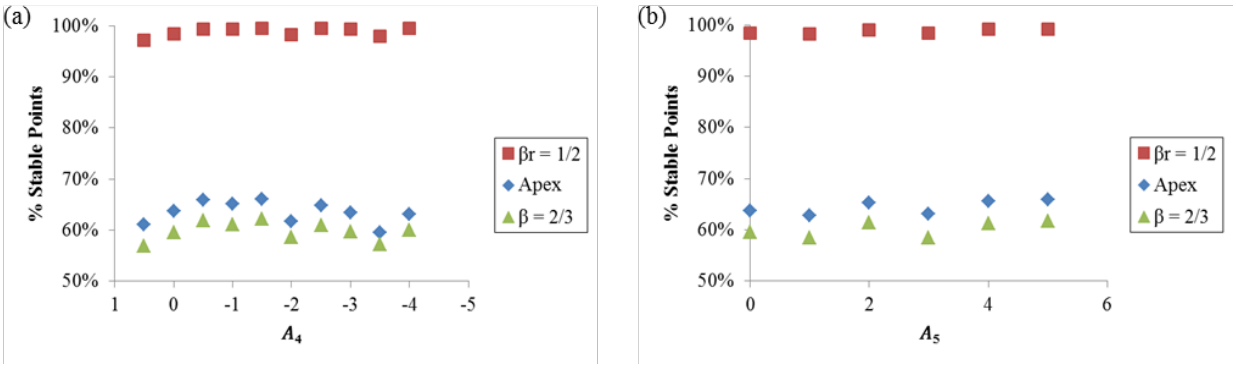

Figure 4-6: Fractions (as percentages) of stable points in the three viewed regions for adding toroidal (a) octopole and (b) decapole to the toroidal quadrupole.

When adding toroidal octopole and toroidal decapole contributions, there was no clear trend in any of the features of the stability diagram (Supplemental Figure 4-6 through Supplemental Figure 4-11). When looking at the overall fraction of stable points of the three regions observed, $A_4 = -1.5$ and $A_5 = 5$ had the highest fraction of stable points (Figure 4-6).

4.5 Conclusions

We have explored adding different harmonic fields to the toroidal quadrupole to observe the effects on the fields and the stability of trapped ion motion. The toroidal octopole and toroidal decapole showed trends in the linearity of the fields, but they showed no clear trend in the ion motion stability. Toroidal dipole contributions change the electrode geometry enough to reduce the overall size of the stability diagram. Toroidal hexapole contributions showed the greatest differences in the stability diagram.

While the toroidal dipole, octopole, and decapole contributions did not prove to be useful in improving the performance of the toroidal quadrupole, the toroidal hexapole contributions show promise. The linearity of the axial field was optimized $A_3 = 1.25$, and a maximum in the

linearity of the radial field was not reached within the A_3 range studied. Improvements to the stability diagram were seen within a range of toroidal hexapole contributions. Because the optimization of different features in the stability diagram occurred at different toroidal hexapole contributions, it may not be possible to obtain a stability diagram with no resonance lines when adding only toroidal hexapole contributions to the toroidal quadrupole. Although the other higher-order terms did not make a noticeable contribution by themselves, it is possible that these, combined with the toroidal hexapole, will further improve performance. Future work will involve exploring the mass analysis capabilities of the most optimal toroidal hexapole contributions to the toroidal quadrupole.

4.6 Supplementary Figures

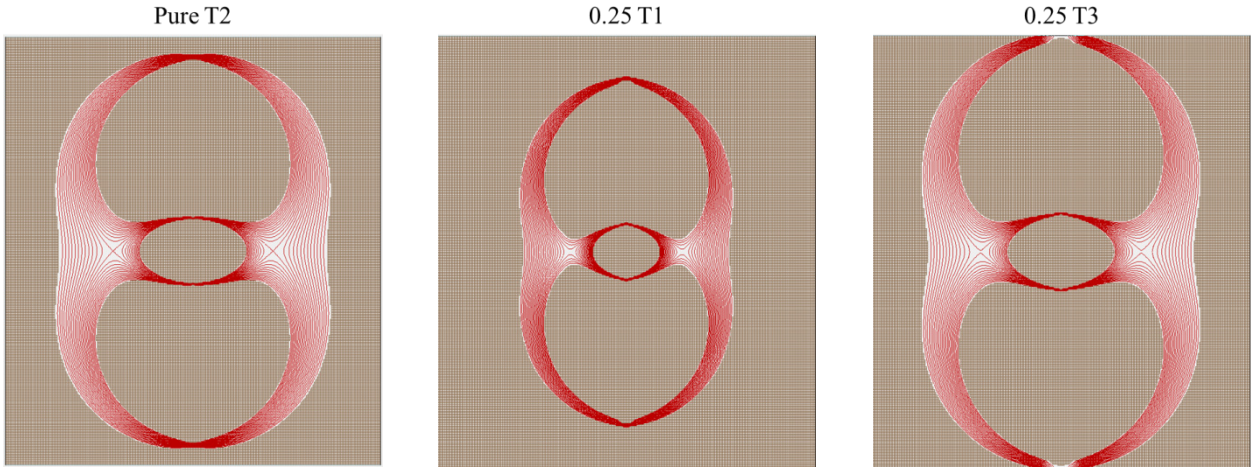

0.5 T3

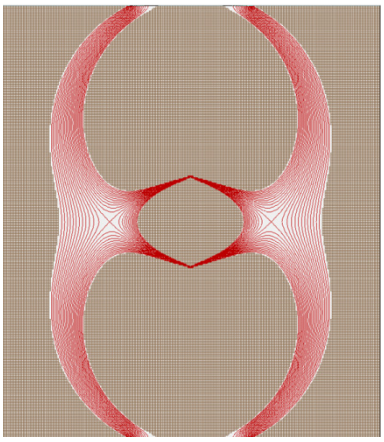

0.75 T3

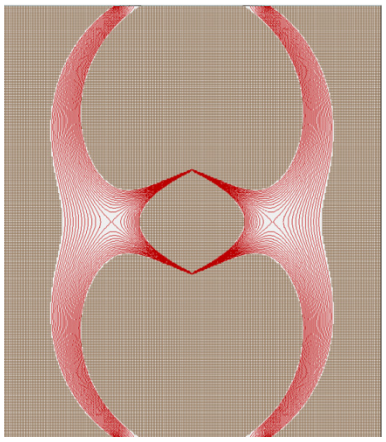

1 T3

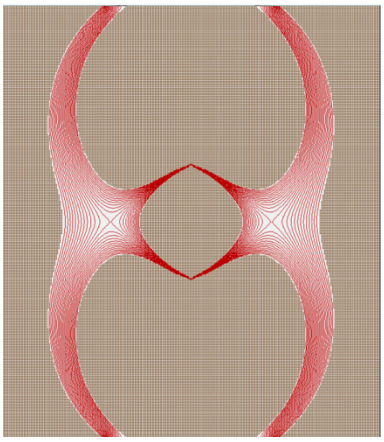

1.25 T3

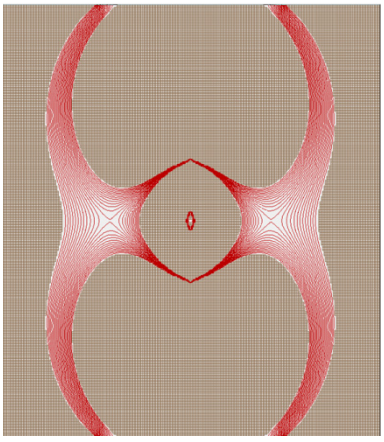

1.5 T3

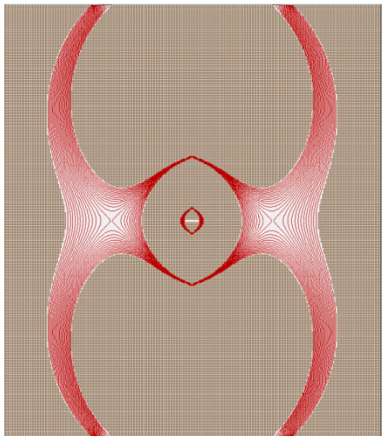

1.75 T3

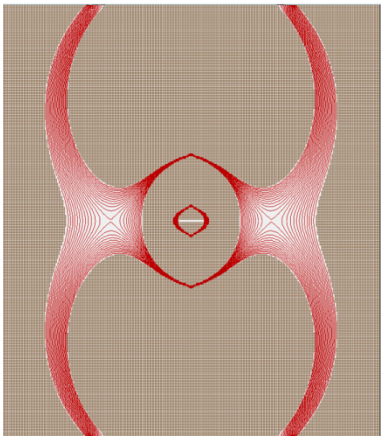

2 T3

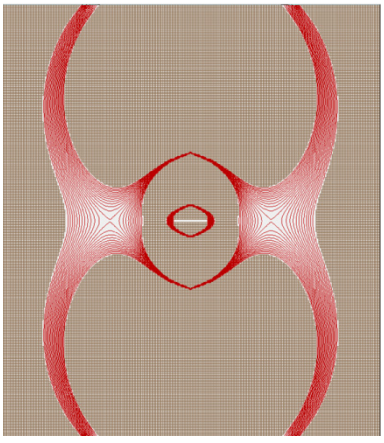

2.25 T3

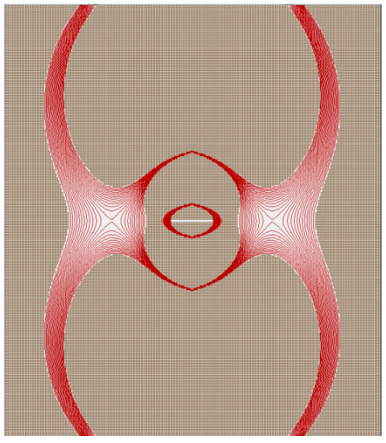

2.5 T3

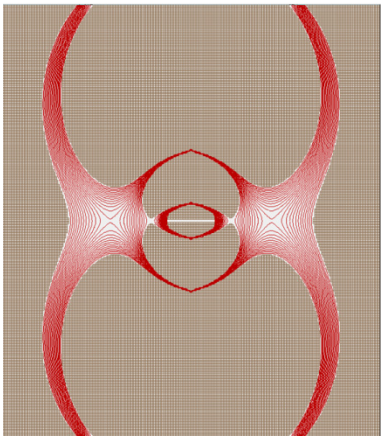

2.75 T3

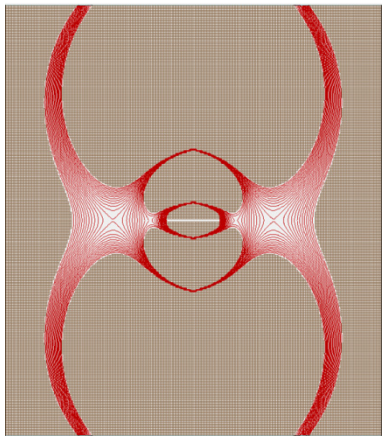

3 T3

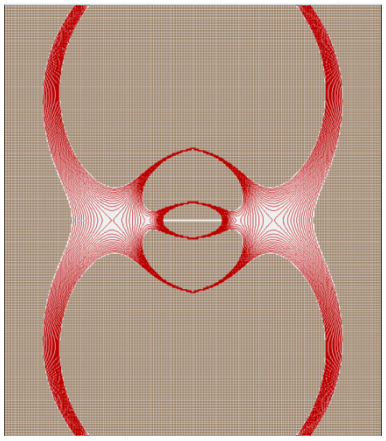

3.25 T3

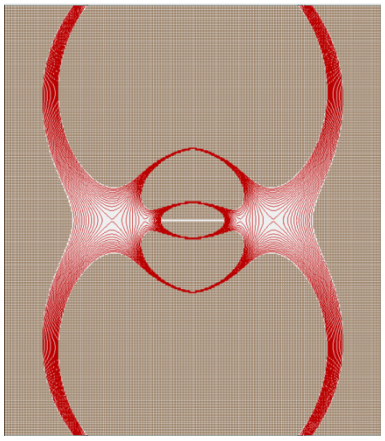

3.5 T3

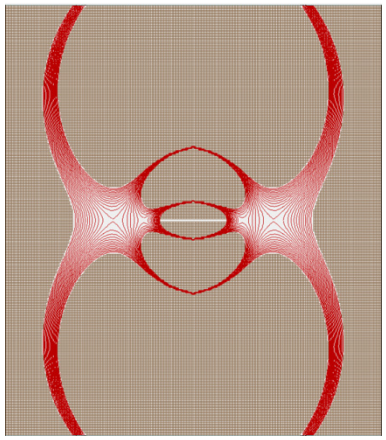

3.75 T3

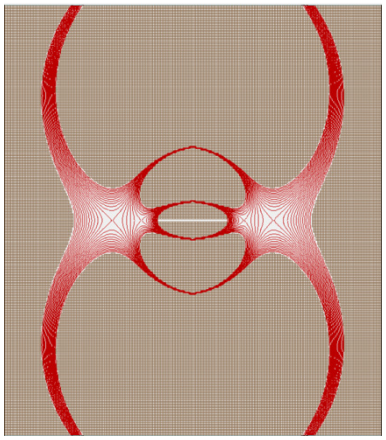

4 T3

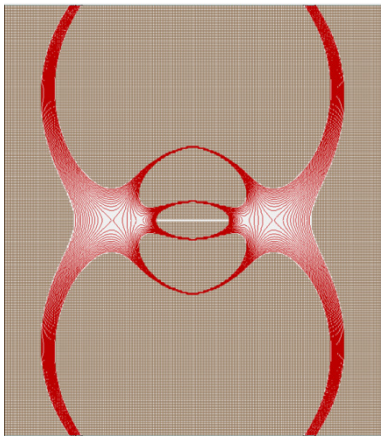

4.25 T3

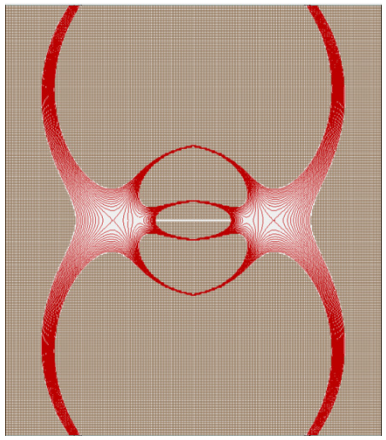

4.5 T3

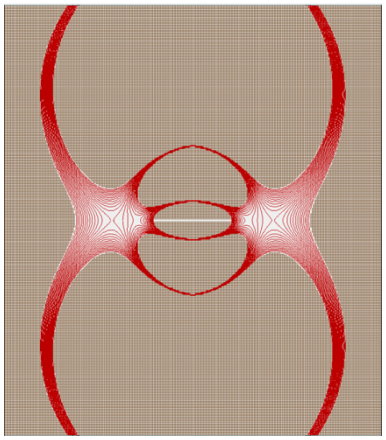

4.75 T3

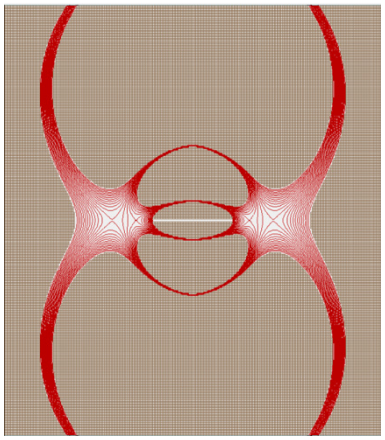

5 T3

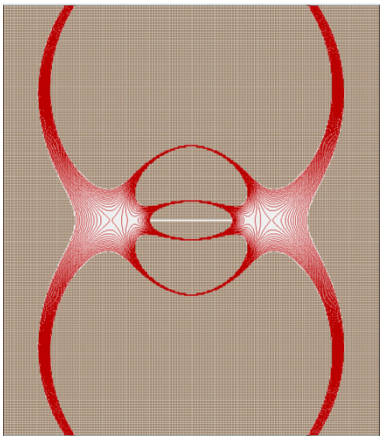

0.5 T4

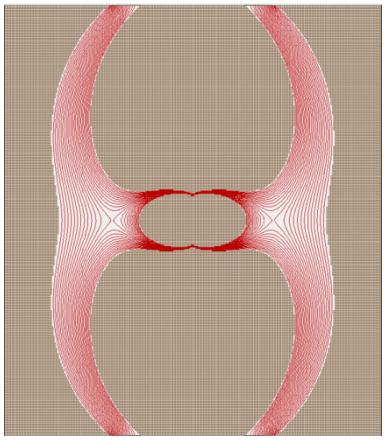

-0.5 T4

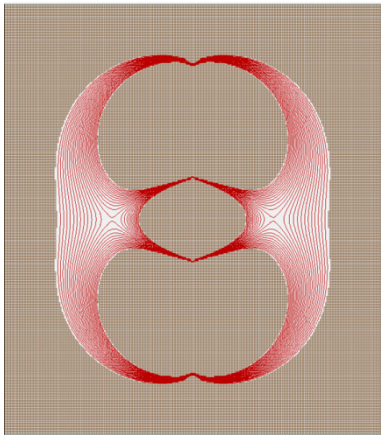

-1 T4

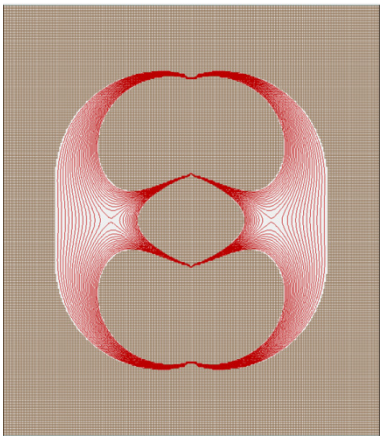

-1.5 T4

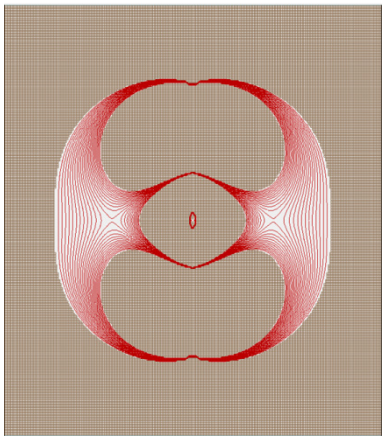

-2 T4

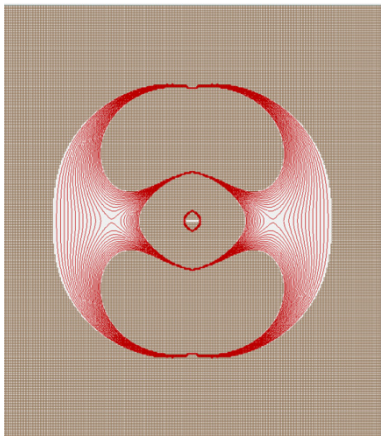

-2.5 T4

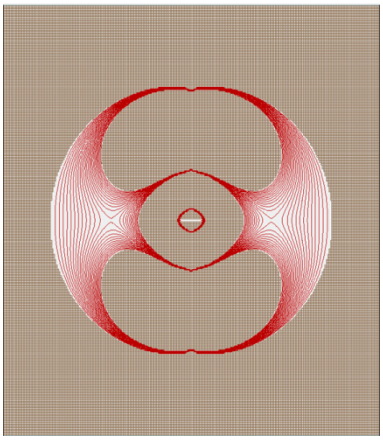

-3 T4

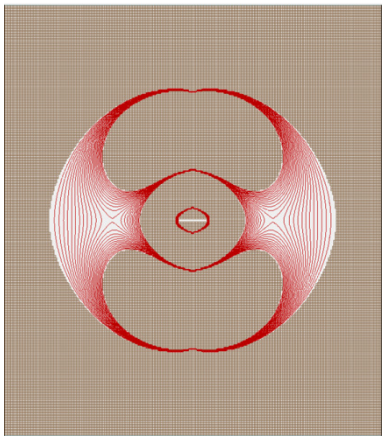

-3.5 T4

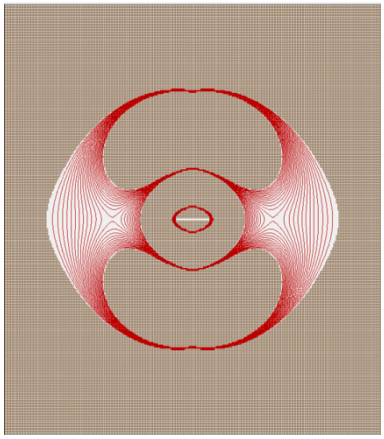

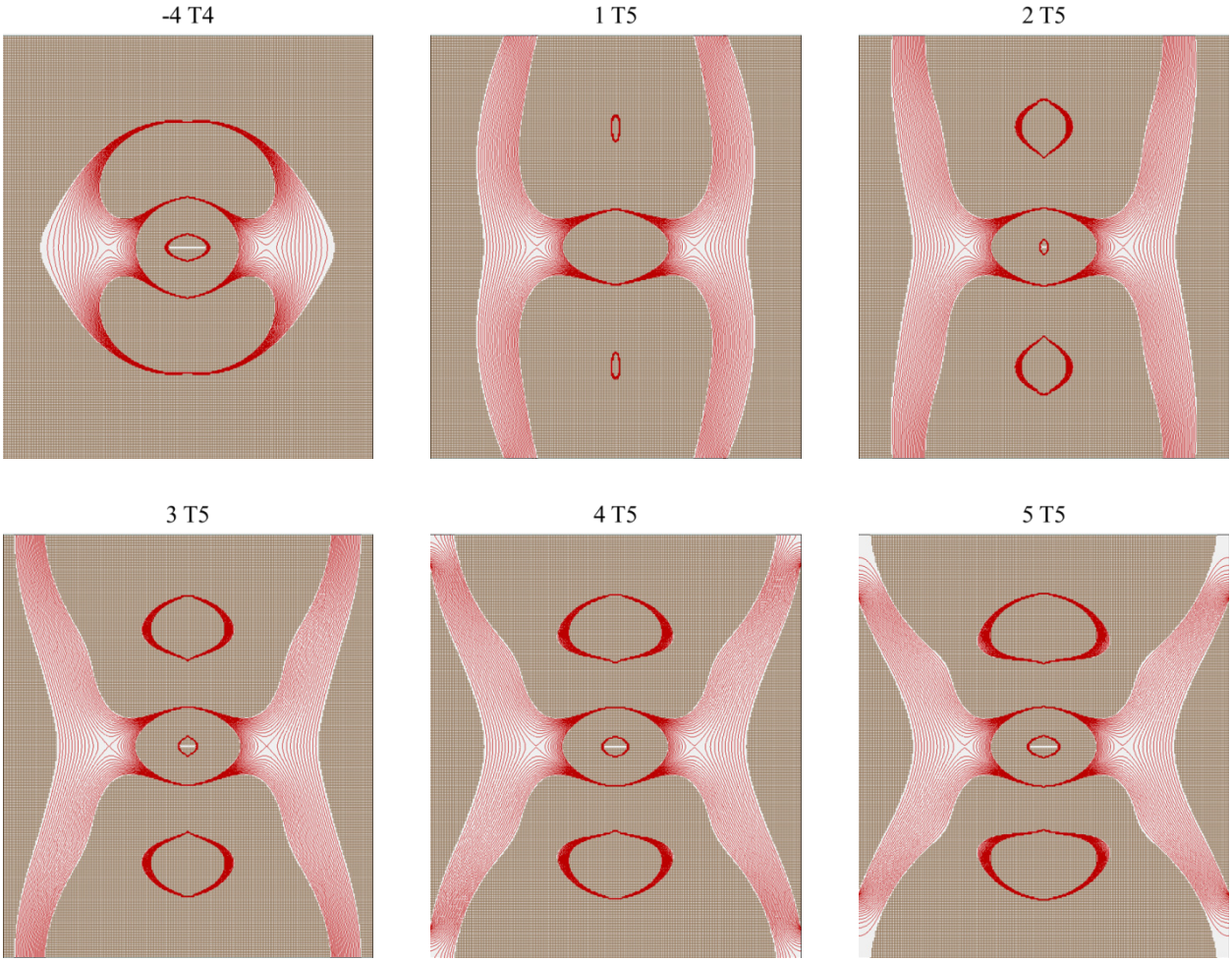

Supplemental Figure 4-1: Potential arrays of the toroidal quadrupole (T2) with added toroidal dipole (T1), toroidal hexapole (T3), toroidal octopole (T4), and toroidal decapole (T5). A_2 = 1, and A_ν is indicated with each array.

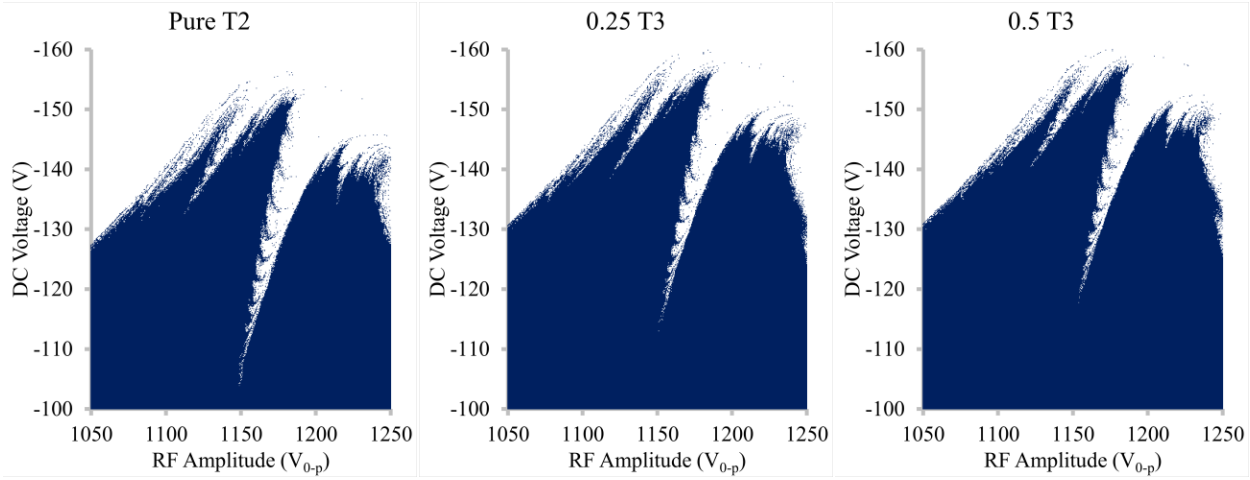

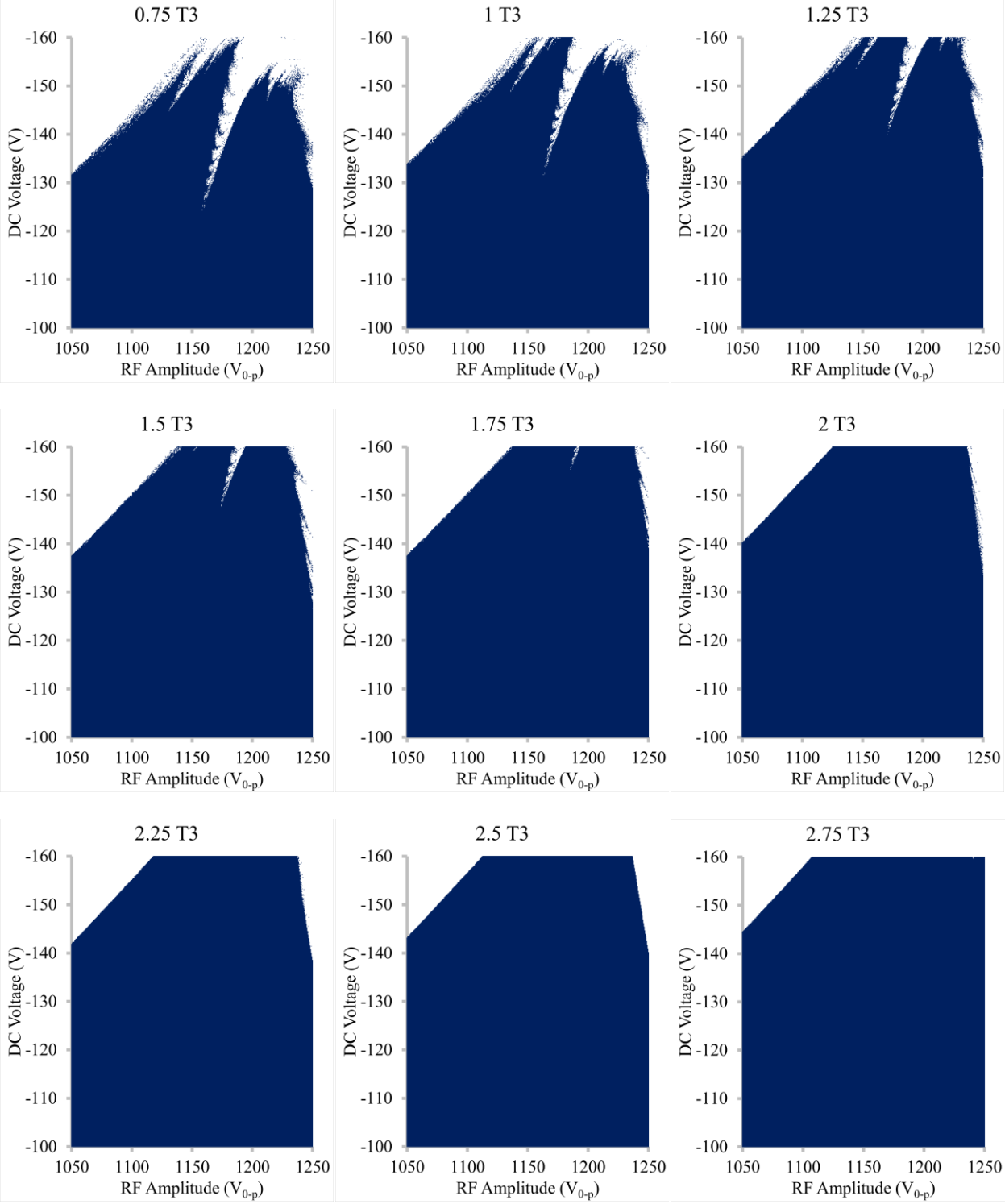

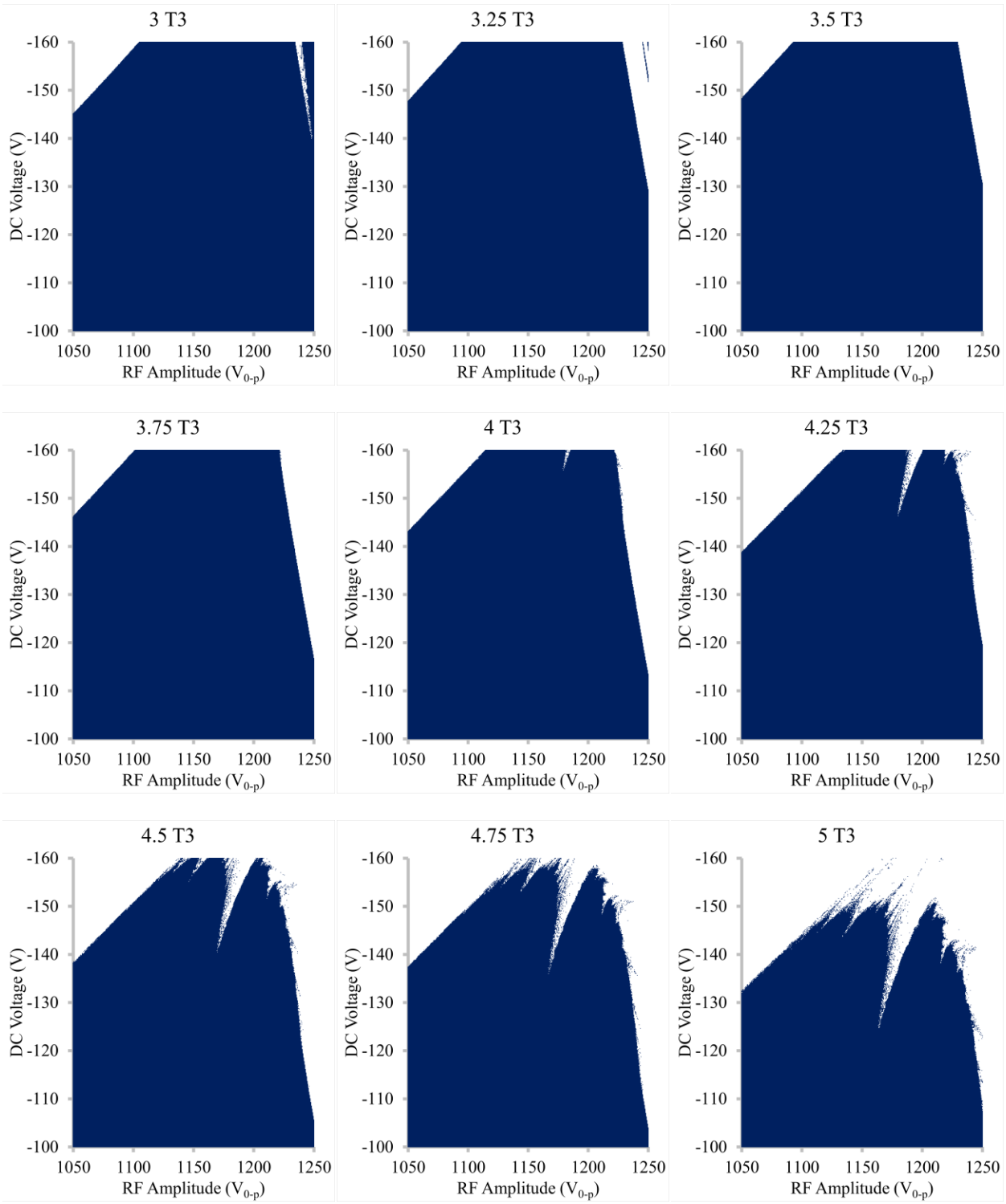

Supplemental Figure 4-2: Apex of the stability diagram upon adding toroidal hexapole (T3) with A_3 ranging from 0 to 5.

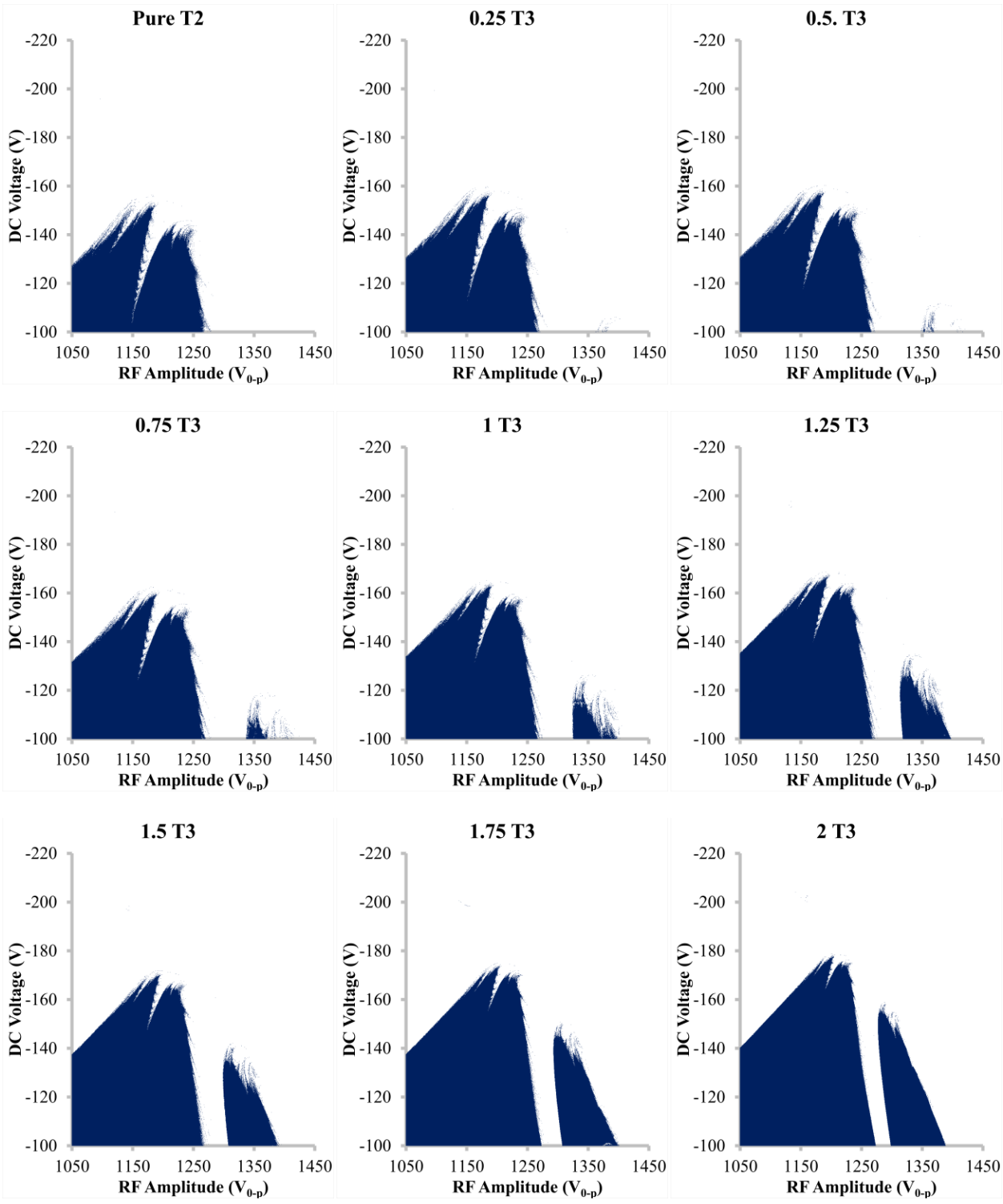

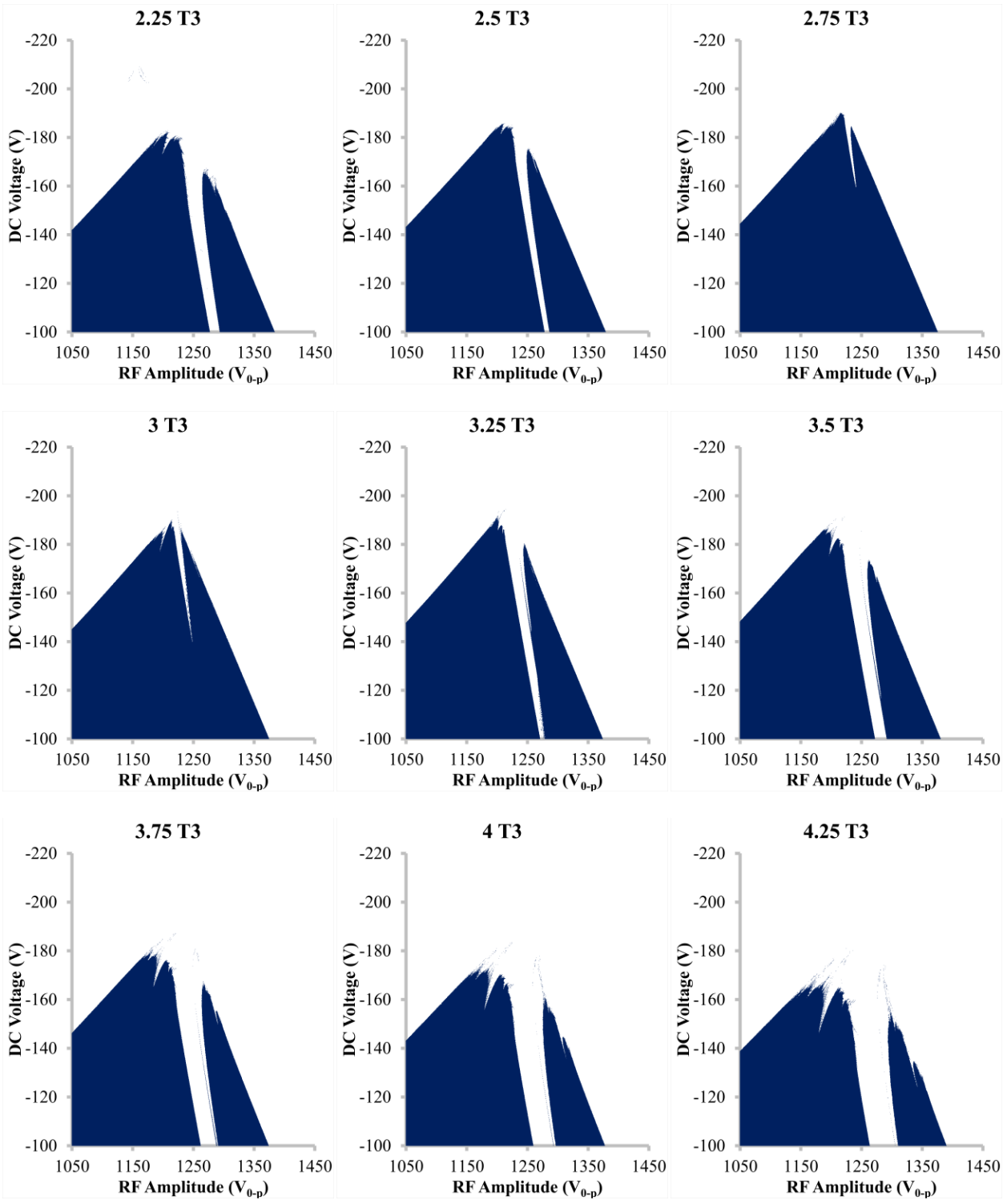

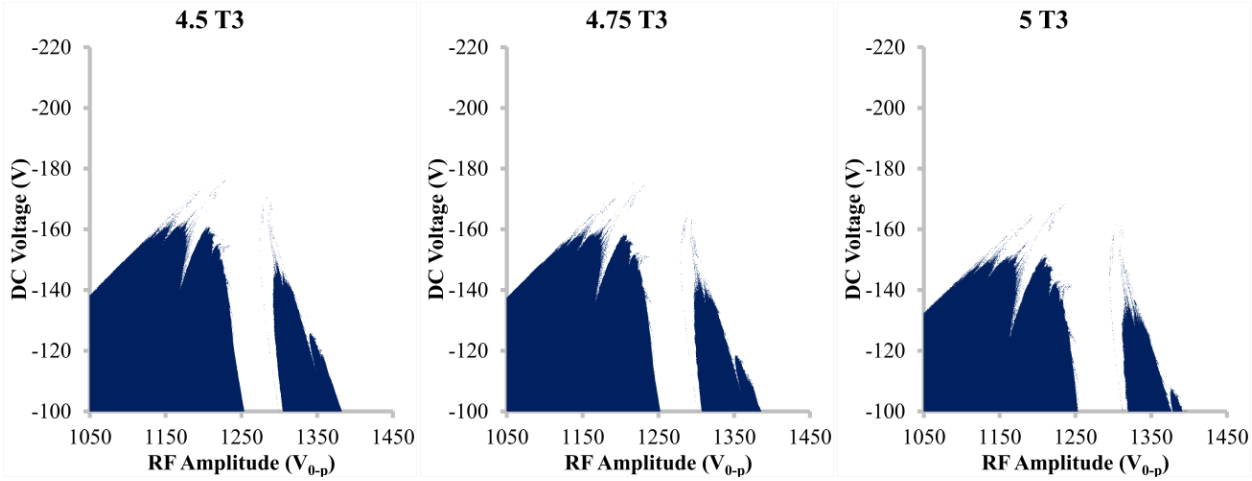

Supplemental Figure 4-3: Expanded view of apex of the stability diagram upon adding toroidal hexapole (T3) with A_3 ranging from 0 to 5.

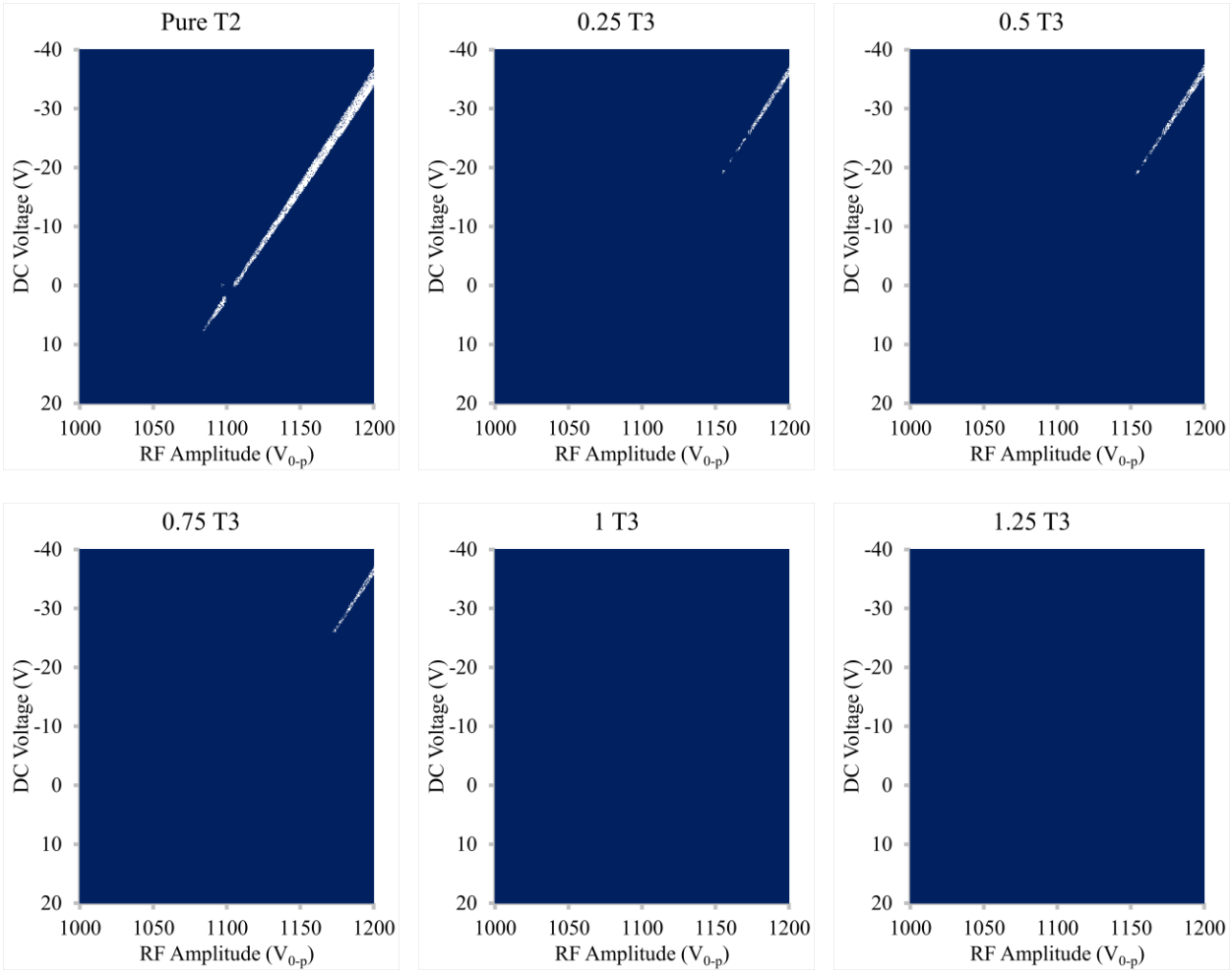

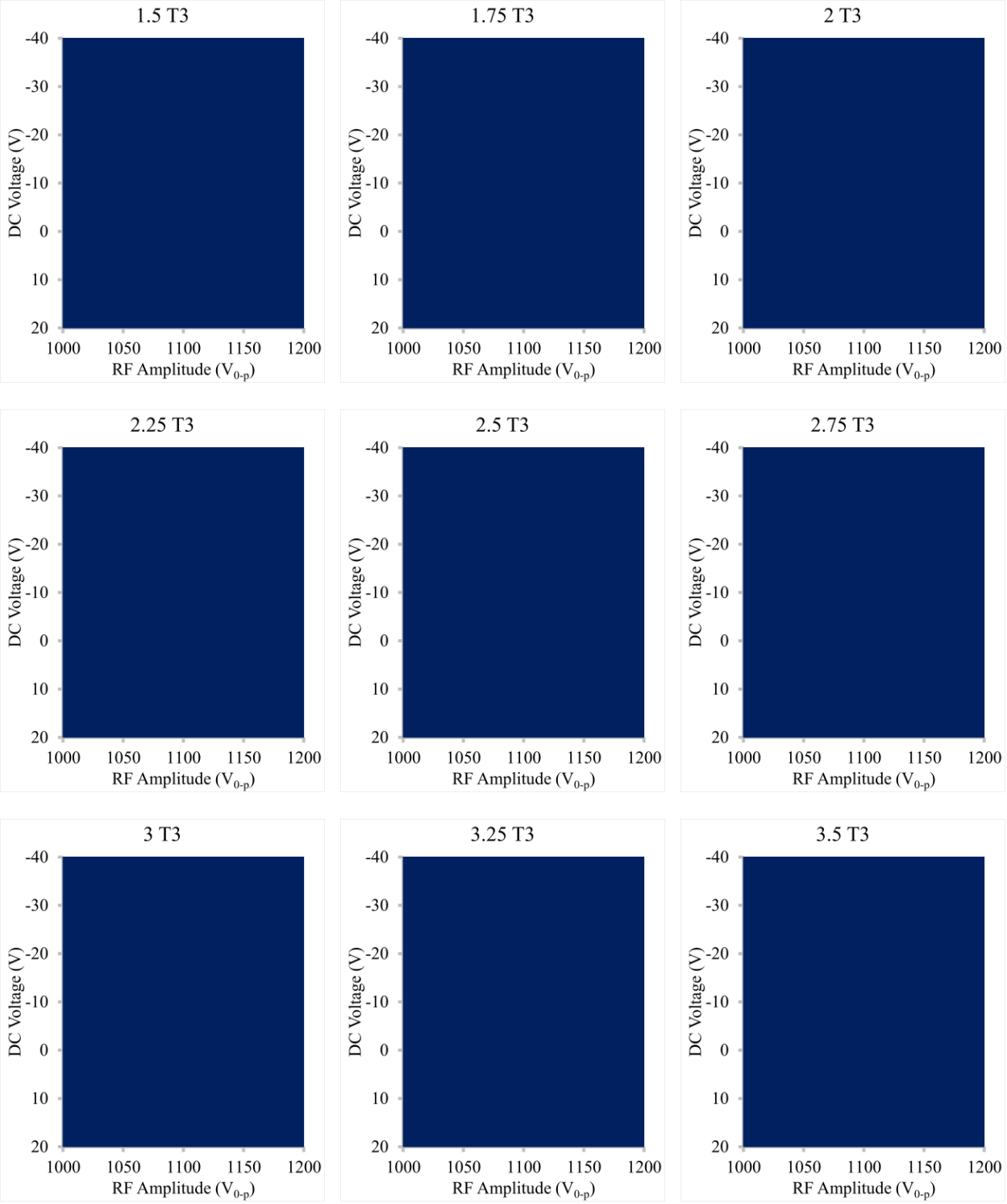

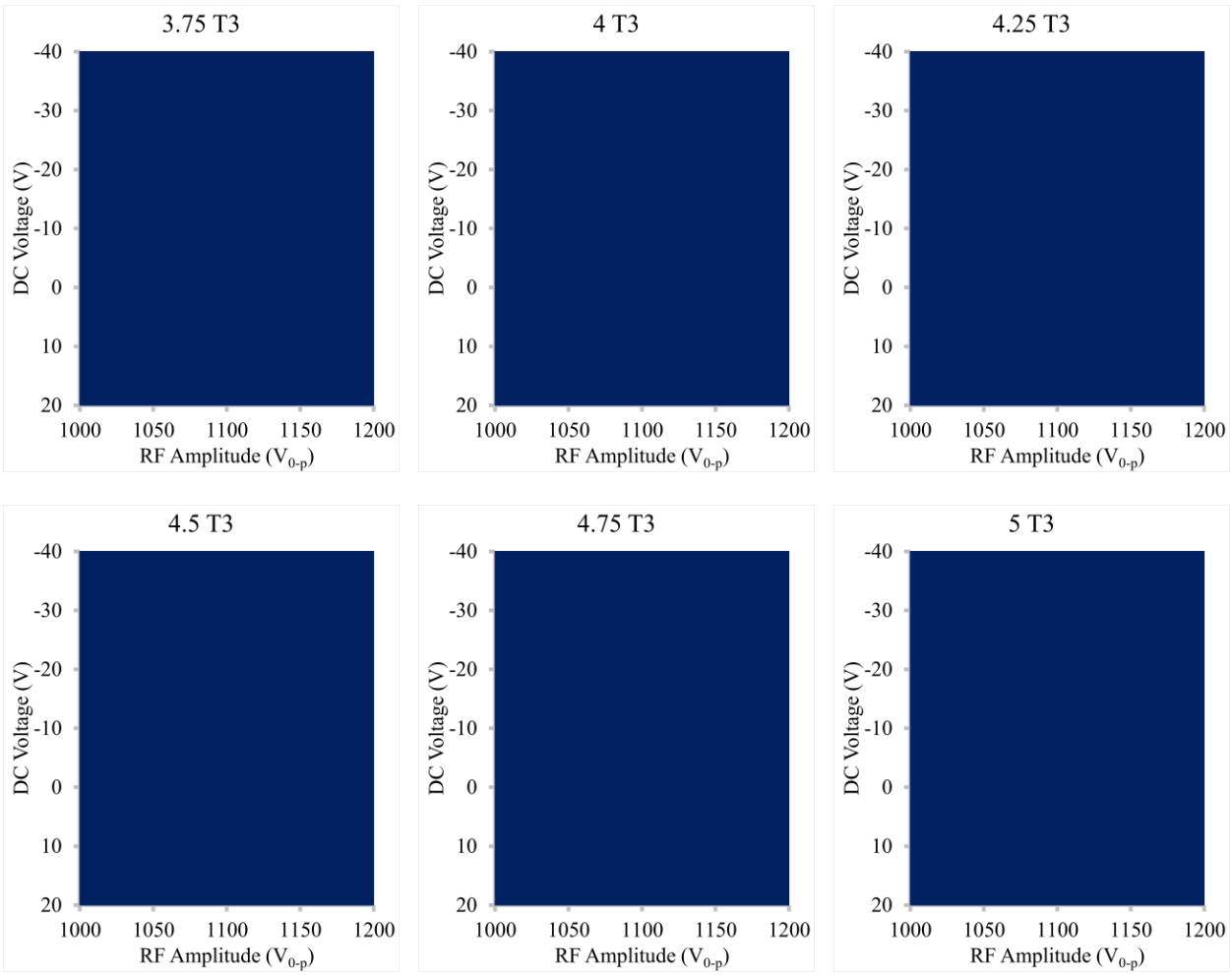

Supplemental Figure 4-4: Region of the stability diagram viewing a portion of the β_r = ½ resonance line upon adding toroidal hexapole (T3) with A_3 ranging from 0 to 5.

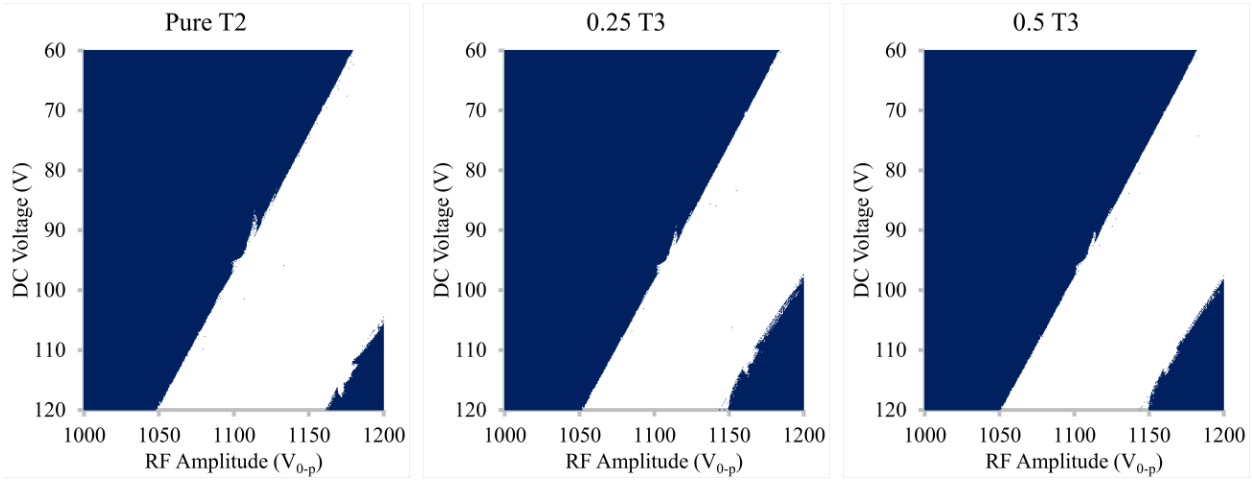

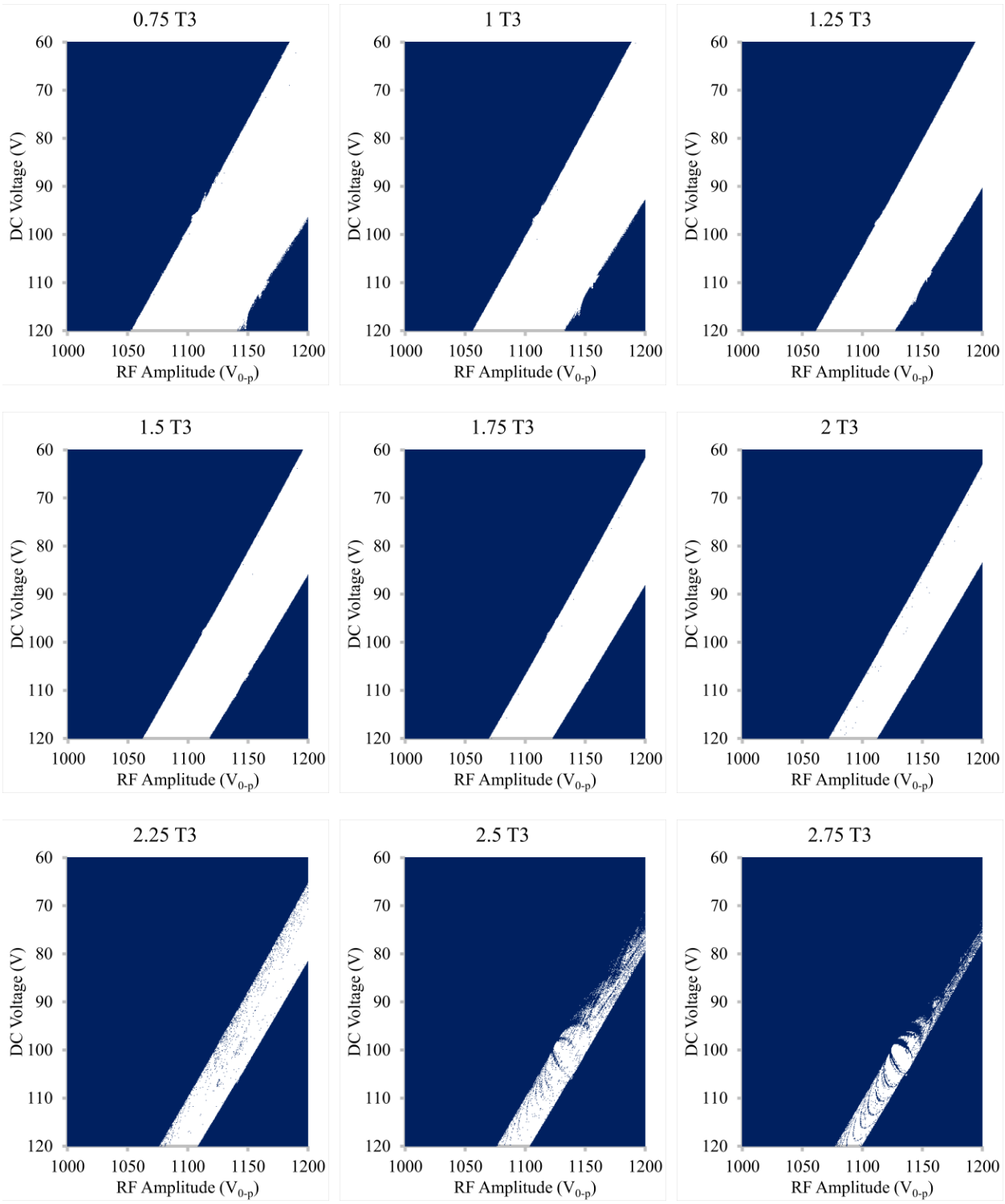

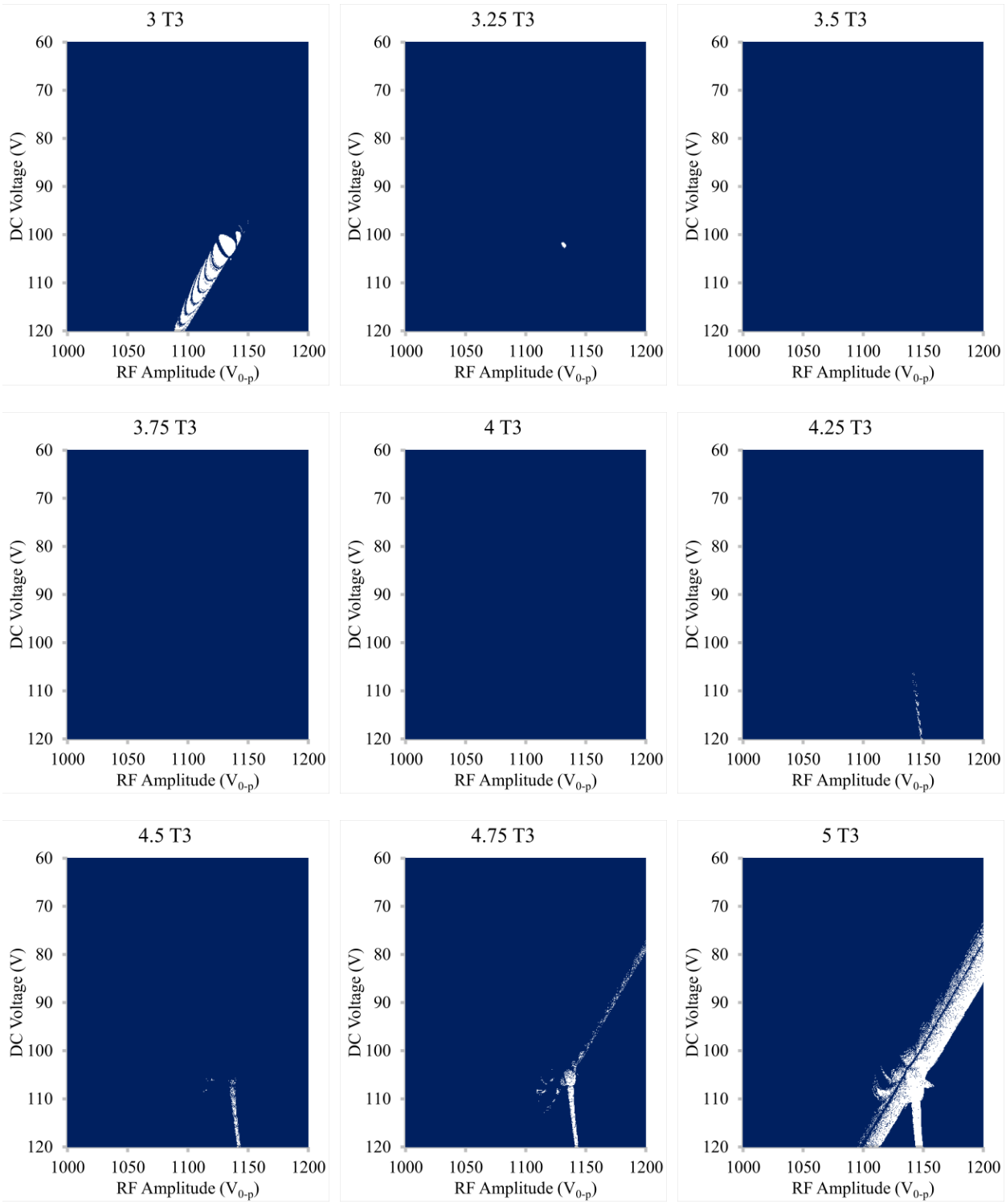

Supplemental Figure 4-5: Region of the stability diagram viewing a portion of the $\beta_r = ⅔$ resonance line upon adding toroidal hexapole (T3) with A_3 ranging from 0 to 5.

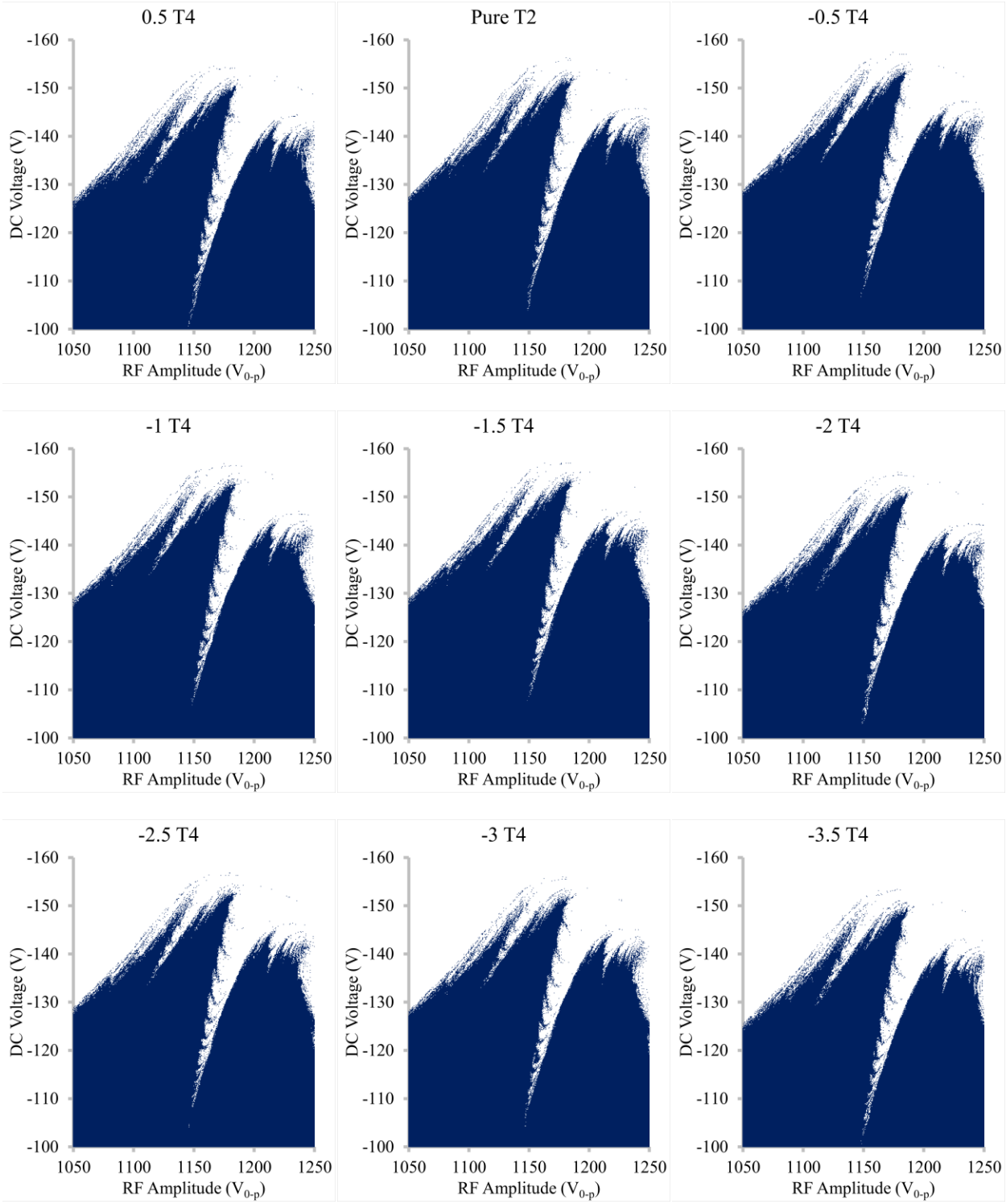

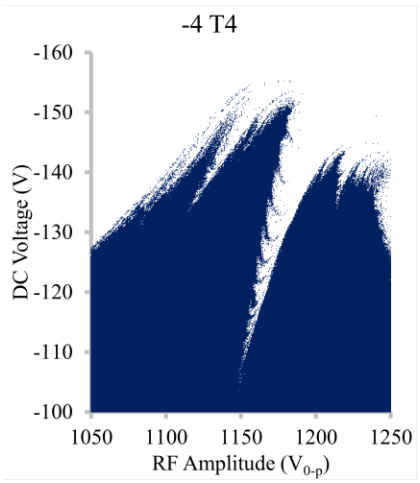

Supplemental Figure 4-6: Apex of the stability diagram upon adding toroidal octopole (T4) with A_4 ranging from 0.5 to -4.

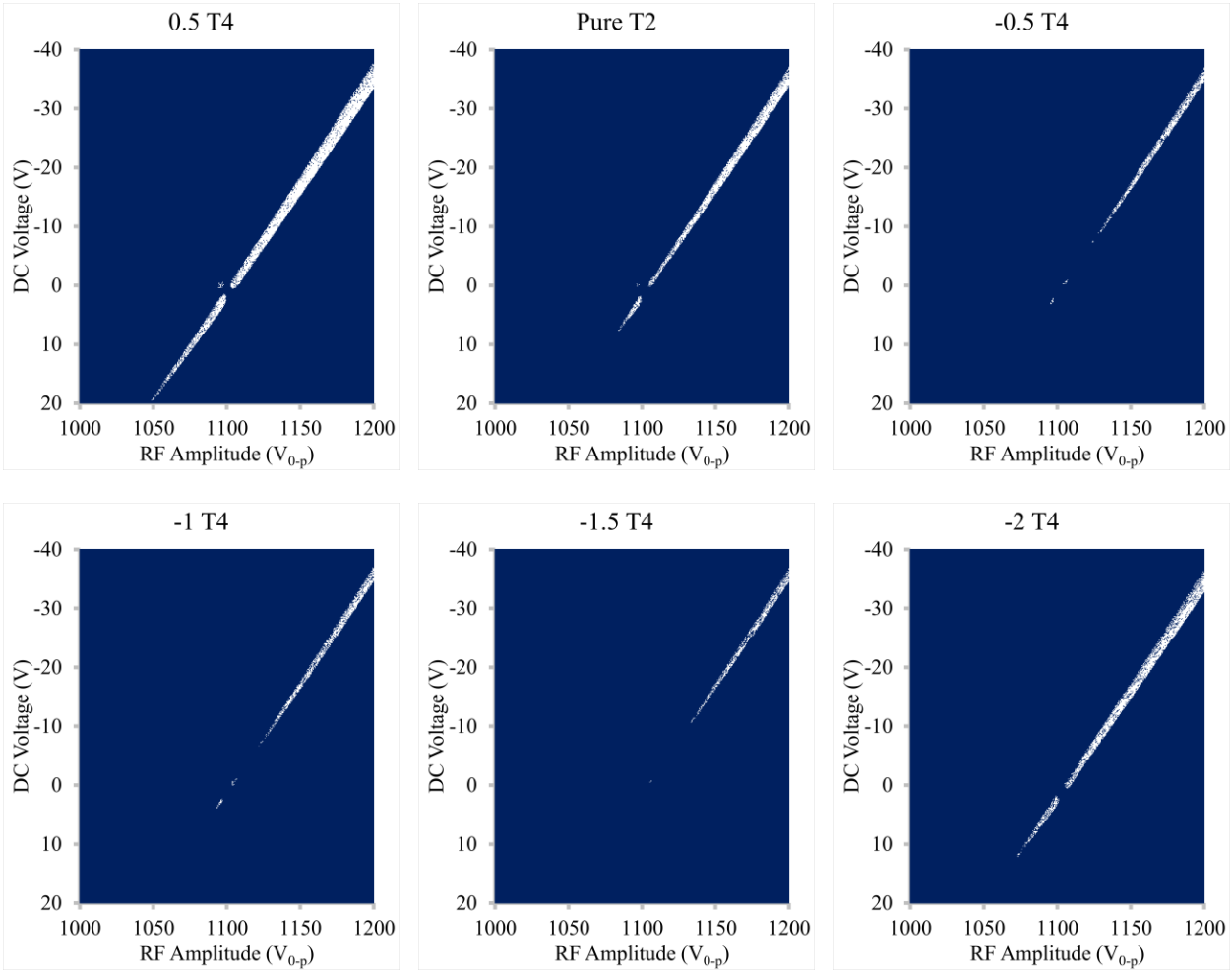

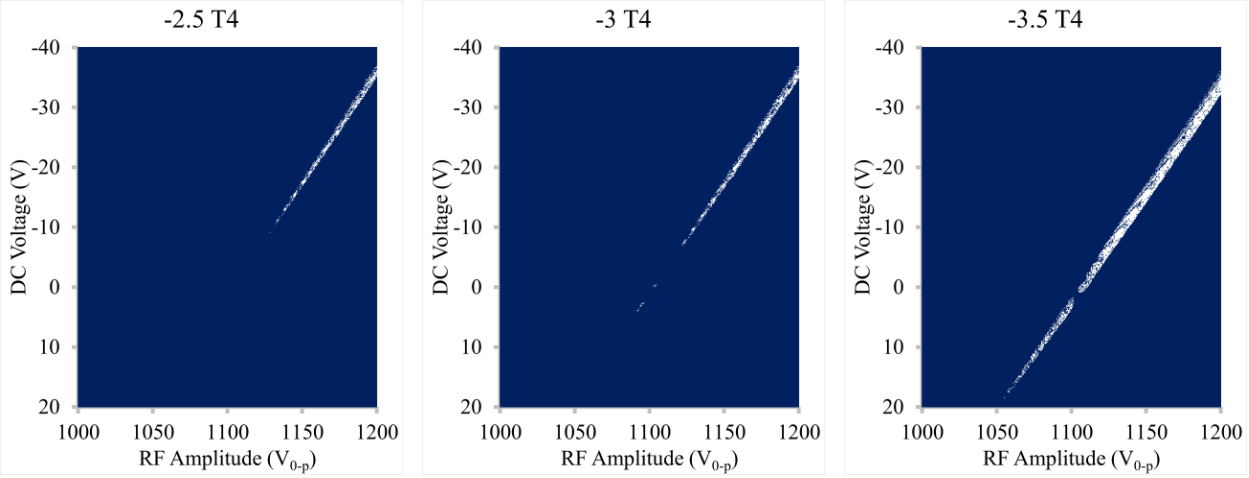

Supplemental Figure 4-7: Region of the stability diagram viewing a portion of the β_r = ½ resonance line upon adding toroidal octopole (T4) with A_4 ranging from 0.5 to -4.

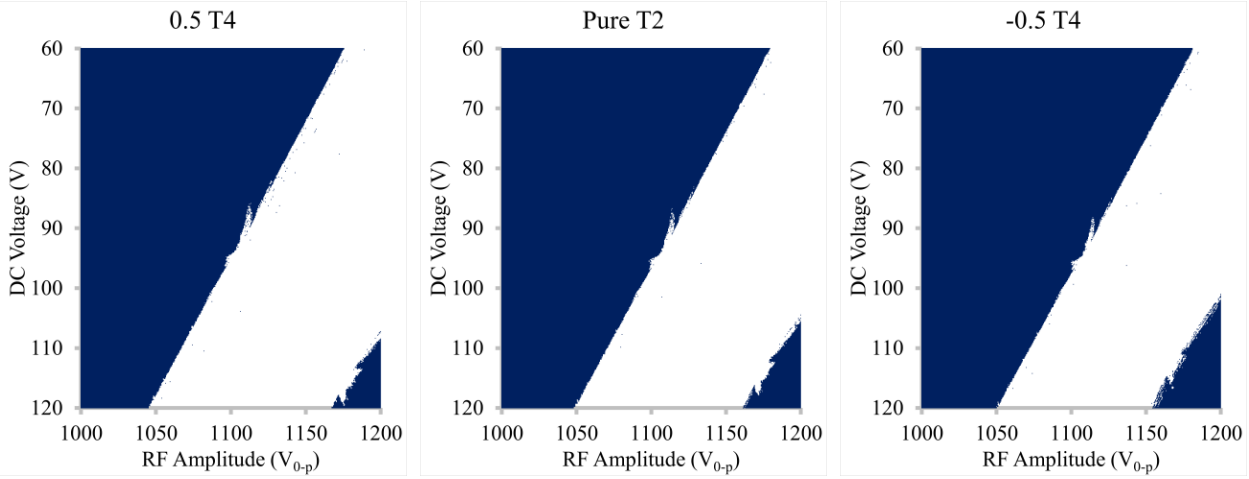

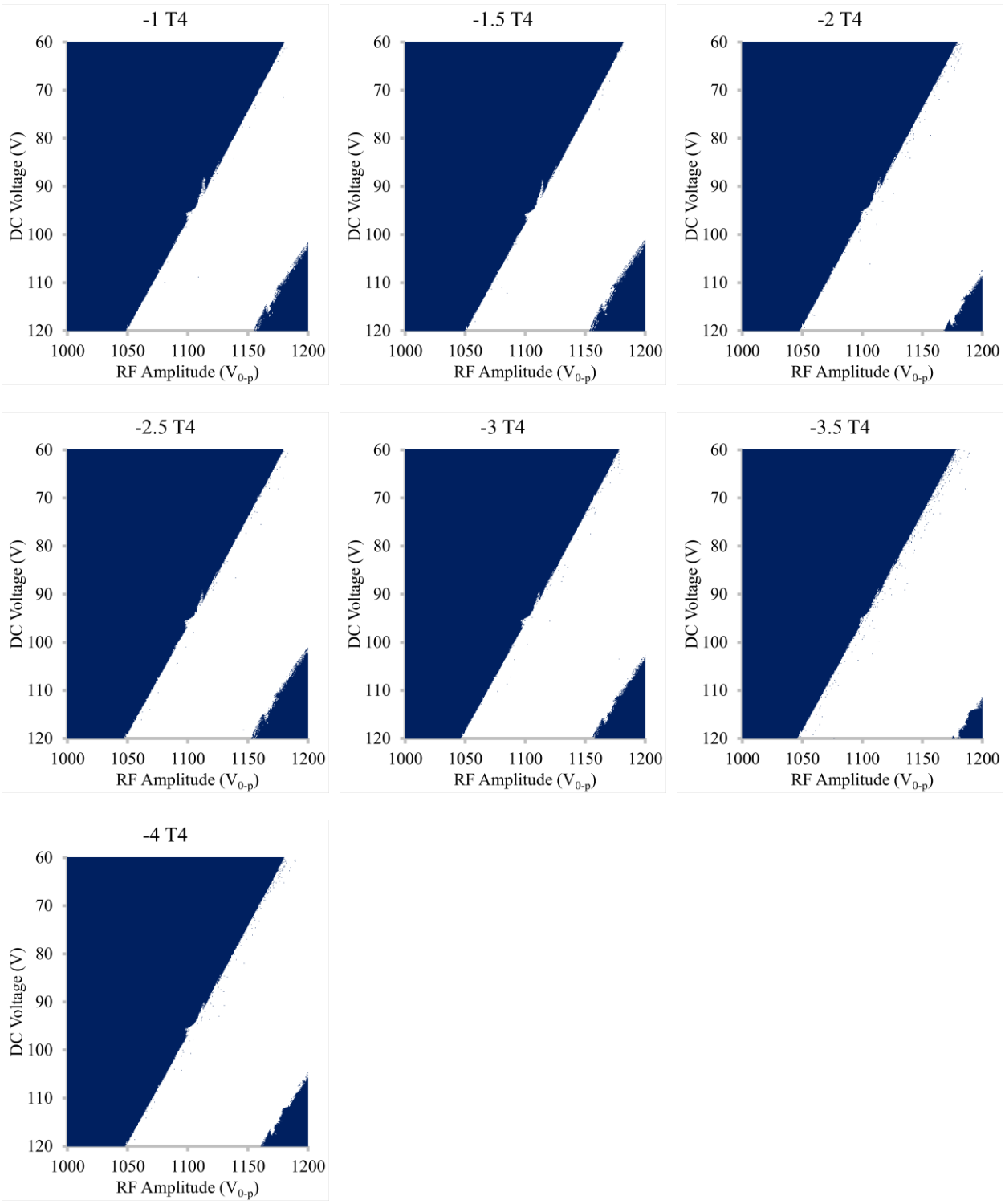

Supplemental Figure 4-8: Region of the stability diagram viewing a portion of the $\beta_r = ⅔$ resonance line upon adding toroidal octopole (T4) with A_4 ranging from 0.5 to -4.

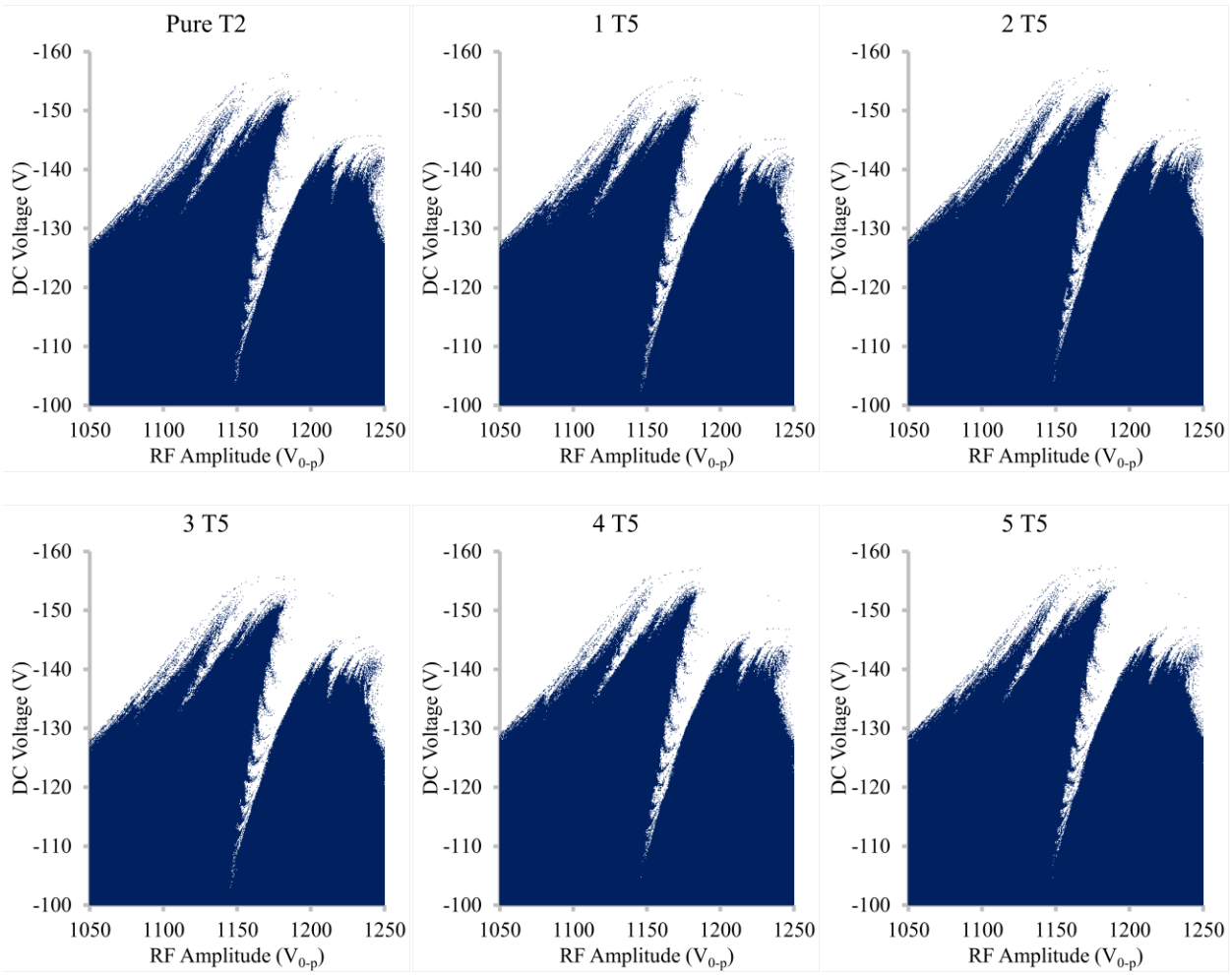

Supplemental Figure 4-9: Apex of the stability diagram upon adding toroidal decapole (T5) with A_5 ranging from 0 to 5.

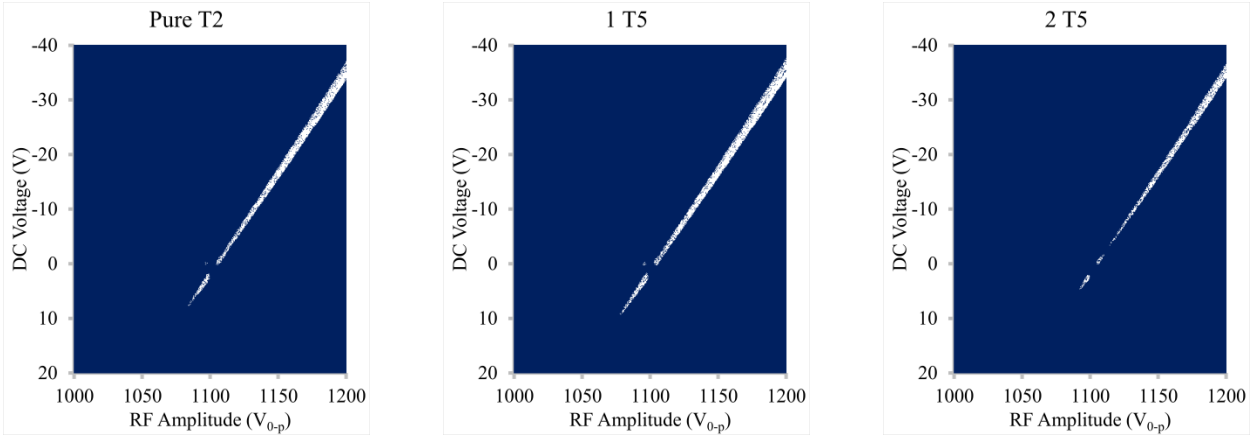

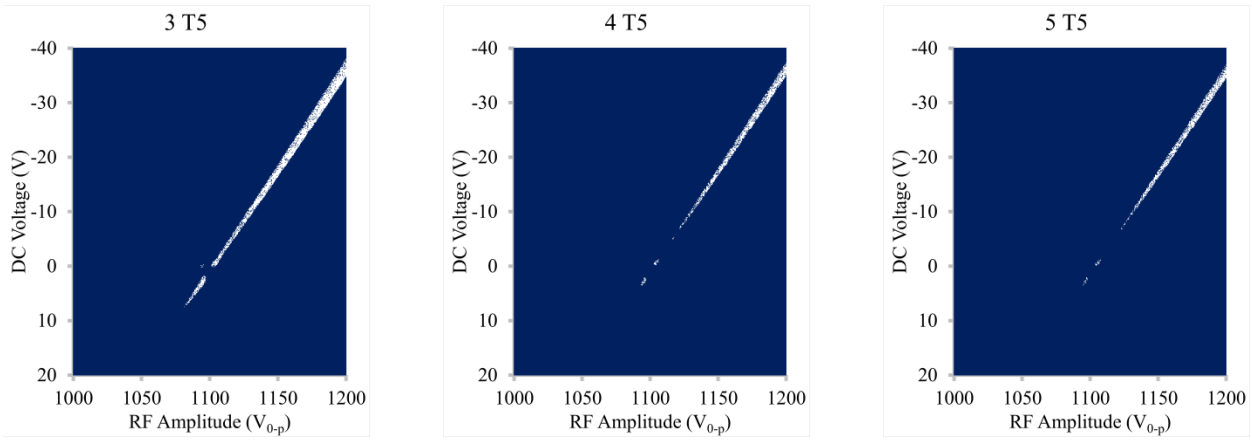

Supplemental Figure 4-10: Region of the stability diagram viewing a portion of the β_r = ½ resonance line upon adding toroidal decapole (T5) with A_5 ranging from 0 to 5.

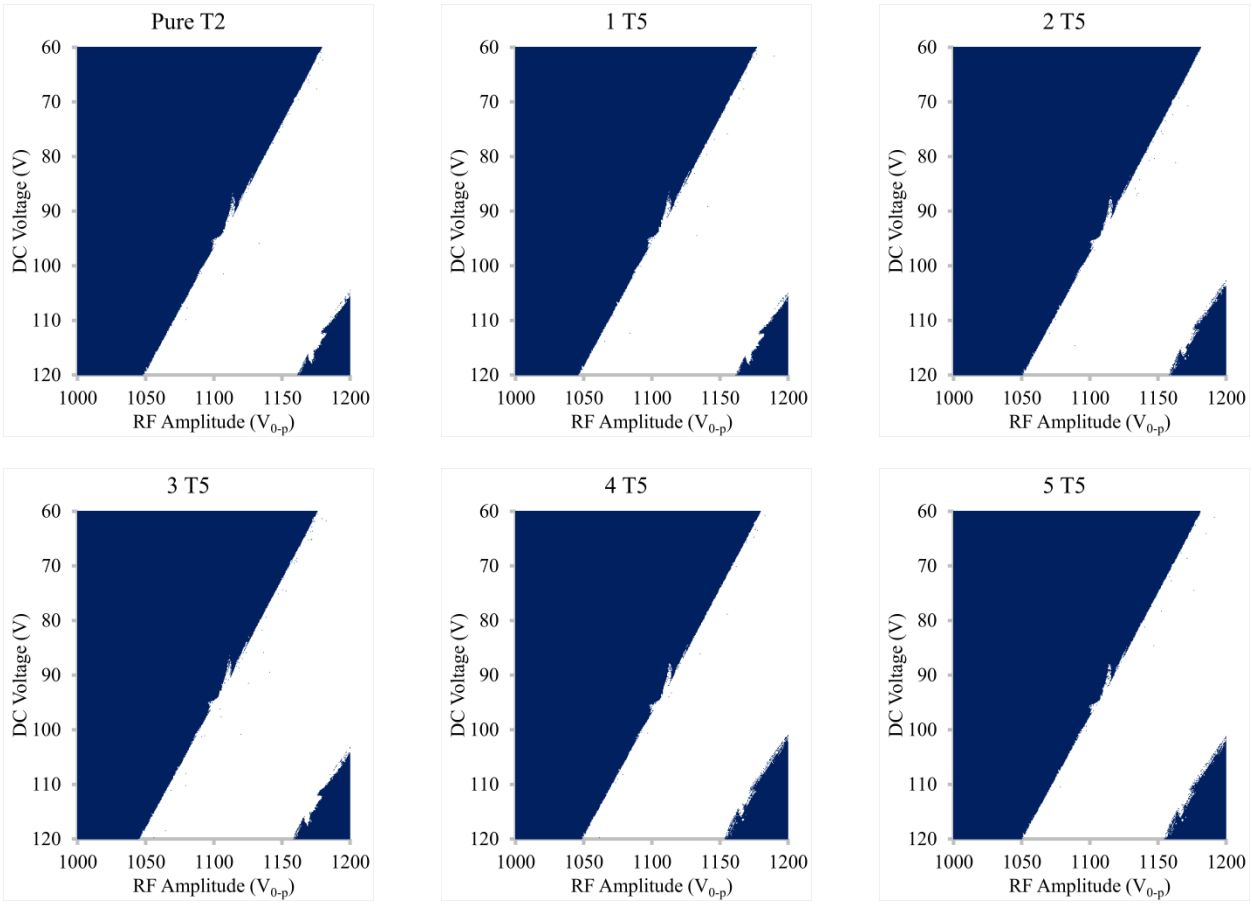

Supplemental Figure 4-11: Region of the stability diagram viewing a portion of the β_r = ⅔ resonance line upon adding toroidal decapole (T5) with A_5 ranging from 0 to 5.

5 MINIATURE CYLINDRICAL TOROIDAL ION TRAP

5.1 The Cylindrical Toroidal Ion Trap

In 2012 Taylor and Austin [100] designed, assembled, and demonstrated the performance of a toroidal ion trap with planar and cylindrical electrodes (Figure 5-1). This design came about as a way to simplify the electrode shapes for manufacturing a miniature toroidal ion trap. In developing the design, they considered how, for the asymmetric toroidal ion trap [61], the central electrode had an expanded surface area and the outer electrode had a reduced surface area. This difference in electrode shape for the central and outer electrode was implemented to overcome the field effects from the curvature of the trapping volume. They also applied a RF frequency to the endcap electrodes so as to eject the ions radially towards the central electrode rather than axially. This allowed for the detection system to be placed inside the cavity of the central electrode. With these considerations, they used SIMION to determine the optimum dimensions for this ion trap (R = 36.14 mm, r_0 = 5.91 mm, z_0 = 5.91 mm).

The resulting ion trap consisted of a copper central electrode, three stainless steel electrodes, Delrin spacers, a Delrin sleeve, a custom electron gun, a conversion dynode, and an electron multiplier. The central electrode was made from copper in order to shield the conversion dynode and electron multiplier inside the electrode from the RF outside the electrode. A portion of the slit in the central electrode was blocked so that electrons from the electron gun would not go through to the detector. The central electrode also had a wide base to be used to mount the trap to a vacuum flange as well as a raised edge on the wide base used for aligning the electrodes. Two of the stainless steel electrodes were used for an RF signal and the stainless steel electrode between them was used for an AC signal. The outer diameter of these three electrodes

was the same as the outer diameter of the raised edge of the central electrode's wide base. The AC electrode also had an ionization slit lined up with the electron gun. Delrin spacers were used in between the electrodes, and Kapton film was used to adjust the axial spacing. A Delrin sleeve was used to align all the electrodes with the raised edge on the wide base of the central electrode. Electrical connections to the RF and AC electrodes were made through the Delrin sleeve. The housing of the electron gun was made from aluminum with a filament inside, and was mounted on the outside of the Delrin sleeve. The electrodes and spacers were all pressed down with Delrin piece on top. A custom conversion dynode was mounted inside the cavity of the central electrode with an electron multiplier below.

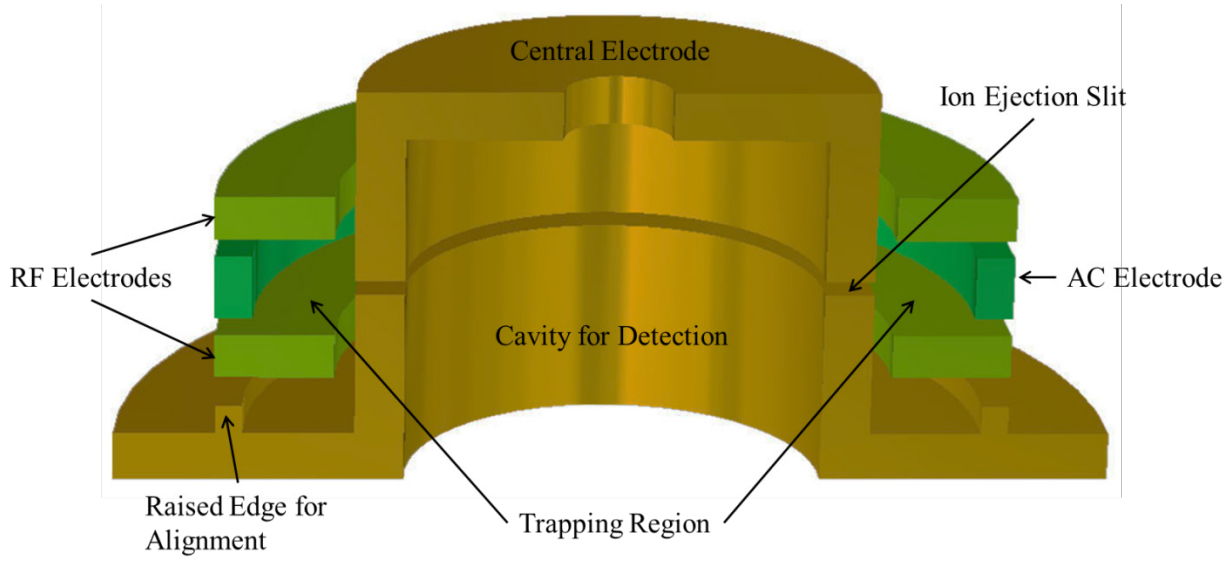

Figure 5-1: Electrode configuration of the original cylindrical toroidal ion trap. (R = 36.14 mm, r_0 = 5.91 mm, z_0 = 5.91 mm)

After the trap was assembled, the performance of the cylindrical toroidal ion trap was measured. By adjusting the spacing between the RF and AC electrodes, the resolution was optimized for both forward and reverse scans. For the *m/z* 91 and *m/z* 92 peaks of toluene, the

optimum resolution of Δm = 0.32 amu was observed when the spacing was z_0 = 5.81 mm during a reverse scan. Using toluene's *m/z* 91 peak, they found boundaries of the stability diagram, but with the limited DC offset, they could not see either the upper or lower apex. The q_z value at the boundary when a_z= 0 can be extrapolated to be about 1.075. They also performed a tandem analysis on the *m/z* 134 ion of iso-butylbenzene.

5.2 First Miniaturized Cylindrical Toroidal Ion Trap

In order to miniaturize the cylindrical toroidal ion trap, we designed an ion trap with 1/3 the trapping dimensions, r_0 and z_0, while using most of the setup of the original cylindrical toroidal ion trap (Figure 5-2). Pieces reused from the original trap included the central electrode, the Delrin sleeve, one of the Delrin spacers, the top Delrin piece, the electron gun, and the conversion dynode. New pieces for the smaller trapping volume include the RF and AC electrodes and the spacers.

5.2.1 Electrode Design and Trap Assembly

The electrodes we designed maintained the same outer diameter (3.661 in. or 92.99 mm) in order to use the same Delrin sleeve for electrode alignment. The r_0 was reduced to 1.965 mm by reducing the inner diameter of the AC electrode. The z_0 was reduced to 1.92 mm by decreasing the thickness of the AC electrode to 0.098 in. (2.49 mm) and by decreasing the space between the electrodes to 0.027 in. (0.675 mm). Instead of making new spacers, we used 0.025 in. (0.635 mm) ceramic spacers with 0.002 in. (0.051 mm) thick Kapton film. To maintain the alignment of the trapping center with the slit in the central electrode, we designed thicker RF electrodes (0.365 in. or 9.27 mm). The inner diameter of the RF electrodes was also reduced to 2.443 in. (62.05 mm) in order to minimize the space between them and the central electrode. The central

electrode still had a diameter of 2.379 in. (60.43 mm). With the changes to the trapping dimensions, the resulting major radius of the trapping space shifted to R = 1.267 in. (32.18 mm). There was also a Delrin spacer used from the original design that was used between the raised edge of the central electrode's wide base and the bottom RF electrode. The precision machining lab used tolerances as low as 0.001 in. (0.0254 mm).

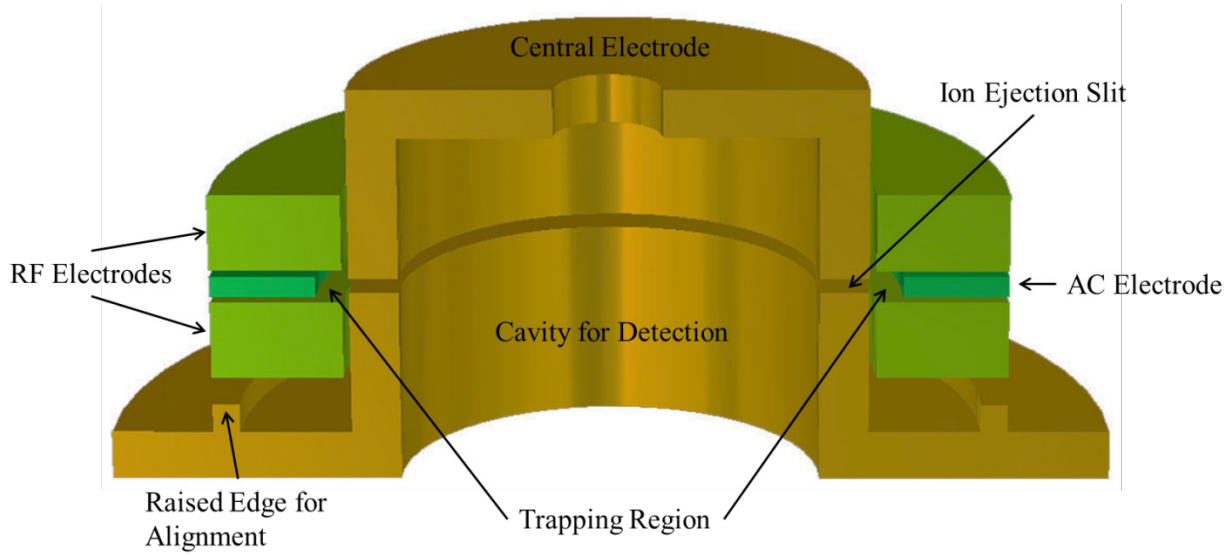

Figure 5-2: Electrode configuration of the cylindrical toroidal ion trap with r_0 and z_0 reduced by one-third and the same central electrode as the original design. (R = 32.18 mm, r_0 = 1.965 mm, z_0 = 1.92 mm)

5.2.2 Performance

To compensate for the smaller dimensions, we used a RF power supply with a higher frequency of about 3.4 MHz. The only signal seen other than noise was during the ionization phase of the ramp. We determined that the capacitance of the trap was too high for the given RF frequency. Capacitance in Farads (F) for two conductive surfaces can be calculated by

$$C = \frac{k\varepsilon_0 A}{d} \quad (5\text{-}1)$$

where k is the relative permittivity of the space between the surfaces, ε_0 is the permittivity of space (8.854×10^{-12} F/m), A is the area of the faces of the surfaces, and d is the separation of the surfaces. Using this equation and estimating k = 1, we determined the capacitance of the trap by calculating the capacitance between all of the electrode surfaces. The largest contributing factor to the capacitance was the area for the space between the RF and AC electrodes; the capacitance between the AC electrode and one of the RF electrodes was about 40.4 pF. The next largest contributing factor was the area for the space between the RF electrodes and the central electrode; the capacitance between one RF electrode and the central electrode was about 19.7 pF. We also calculated the capacitance of the bottom RF electrode to the wide base of the central electrode to be about 9.8 pF. This added up to be a minimum of about 130 pF.

5.3 Second Miniaturized Cylindrical Toroidal Ion Trap with Reduced Capacitance

With the first miniaturized design having too much capacitance, we designed another trap that would have each of the trapping dimensions reduced by one-third (R = 0.4742 in. or 12.05 mm, r_0 = 1.965 mm, z_0 = 1.92 mm) (Figure 5-3). This would require us to make new pieces for the all the electrodes and parts made of Delrin. We still used the same electron gun, conversion dynode, and electron multiplier.

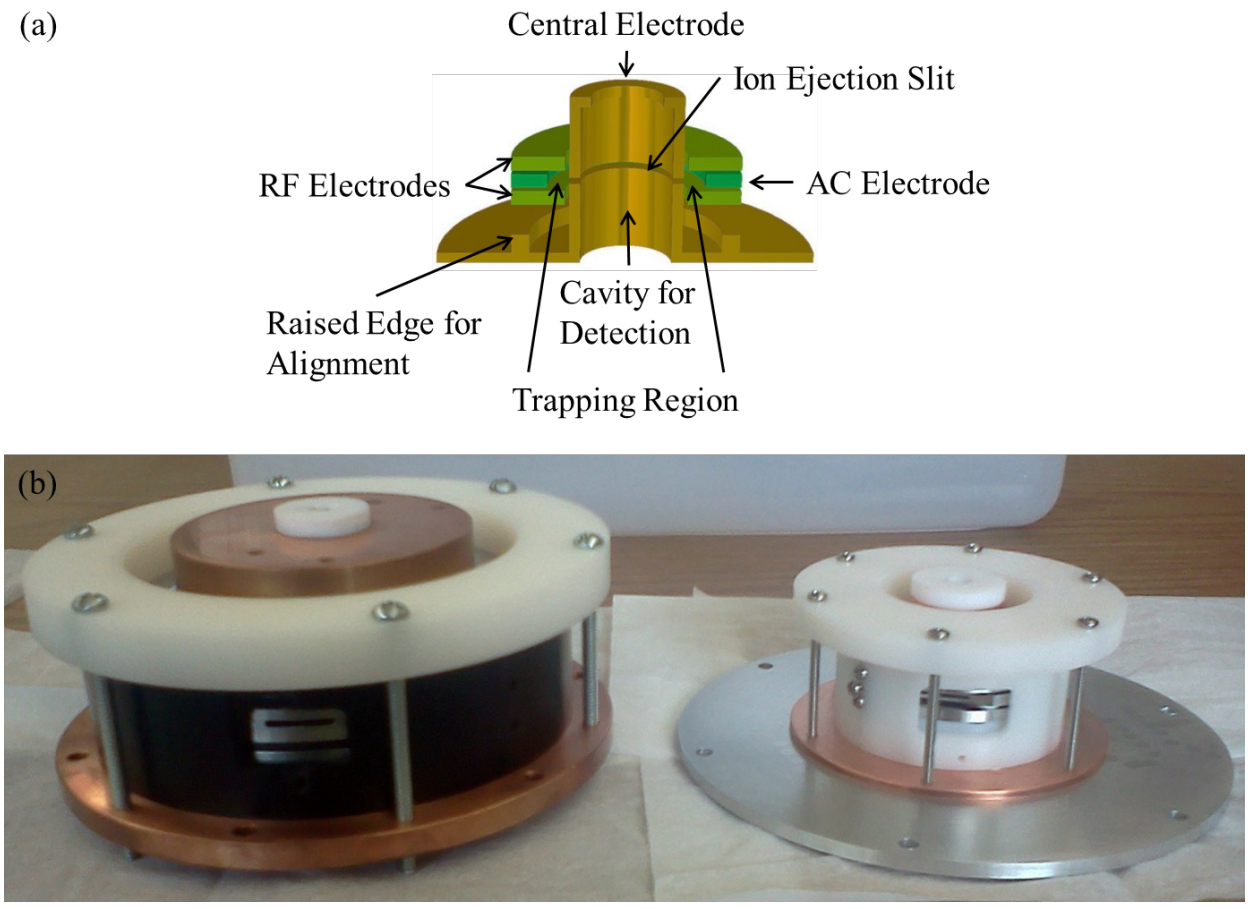

Figure 5-3: Second miniaturized design of the cylindrical toroidal ion trap. (a) Electrode configuration. (R = 12.05 mm, r_0 = 1.965 mm, z_0 = 1.92 mm) (b) Size comparison of the original cylindrical toroidal ion trap (left) and the miniaturized version (right).

5.3.1 Electrode Design and Trap Assembly

We used the same concept of the central electrode for the alignment and ion detection as the original design. The central electrode was made of copper and had a diameter of 0.7936 in. (20.16 mm). The slit was 0.022 in. (0.56 mm) wide, and one-quarter of it was blocked in order to minimize ionization signal from the electron gun. The wide base had a raised edge with an outer diameter of 1.6034 in. (40.726 mm). The RF and AC electrodes also had this same outer diameter for alignment, and they were made of stainless steel. The RF electrodes were 0.1000 in.

(2.540 mm) thick and had an inner diameter of 0.8576 in. (21.78 mm). The AC electrode was 0.0983 in. (2.50 mm) thick and had an inner diameter of 1.1034 in. (28.026 mm). The ionization slit in the AC electrode was 0.498 in. (12.6 mm) wide and 0.025 in. (0.635 mm) tall. We used the same ceramic spacers with Kapton film for the spacing between the RF and AC electrodes (0.027 in. or 0.675 mm). Pieces made from Delrin included the spacer between the bottom RF electrode and the raised edge of the central electrode's wide base, the alignment sleeve, and the top piece to press the electrodes and spacers down. The machining tolerances were as low as 0.0005 in. (0.0127 mm). An aluminum adapter plate was also designed to connect the base of the central electrode to the same mounting as the original trap.

The capacitance of the trap was calculated to be about 22.5 pF total. When we measured the capacitance of the assembled trap, the capacitance was 115 pF. This difference between the calculated and measured values could be due to the permittivity of the spacers and Kapton film as well as the offset in the measurement caused by noise (6–8 pF per measurement). Seeing that the calculated capacitance for this design is smaller than that of the previous miniaturized design, we concluded that we sufficiently minimized the capacitance.

5.3.2 Performance

We used SIMION 8.0 to determine the optimum positioning of the conversion dynode and electron multiplier in order to detect the ions that come through the slit in the central electrode. We used an RF power supply that gave a frequency of 3.42 MHz with no DC offset. We also did not apply an auxiliary AC frequency. We saw two peaks with poor resolution (Figure 5-4). When I calculated the *m/z* that should correspond to these peaks using Equations 1-10 and 1-11 and the q_z boundary from the stability diagram of the original design, the values were lower than what I

would expect to see (about *m/z* 20 and *m/z* 23). Another issue is that the mass range with the RF ramp only reached a maximum of about *m/z* 40.

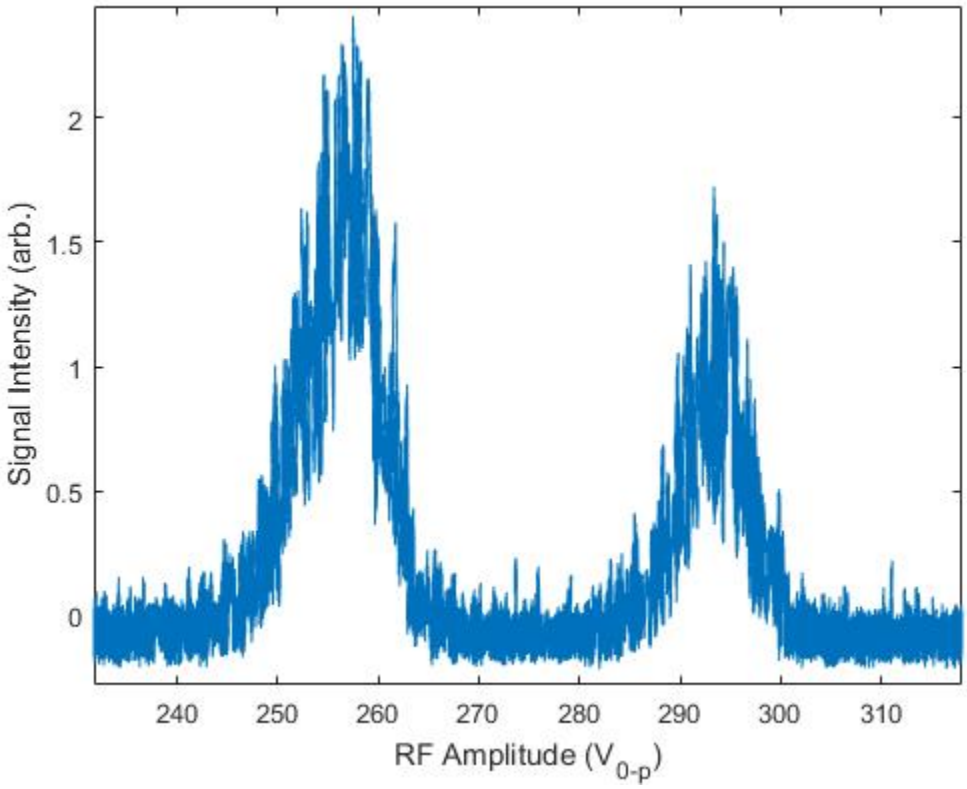

Figure 5-4: Signal of toluene analyzed by second miniaturized cylindrical toroidal ion trap.

The poor resolution could result from poor alignment. With poor alignment, ions in different parts of the trap might experience different stabilities, and there could be additional higher-order fields. There is also the issue that with the smaller trapping volume, it is more difficult to accurately control the sample and background gas pressures inside the trap while still using the same vacuum chamber.

5.4 Third Miniaturized Cylindrical Toroidal Ion Trap

The third design we developed was designed to minimize alignment issues (Figure 5-5), and we designed a smaller vacuum chamber to maintain better control of the sample and background gas pressures. We also used a new RF power supply in order to achieve higher RF amplitudes and improve the mass range.

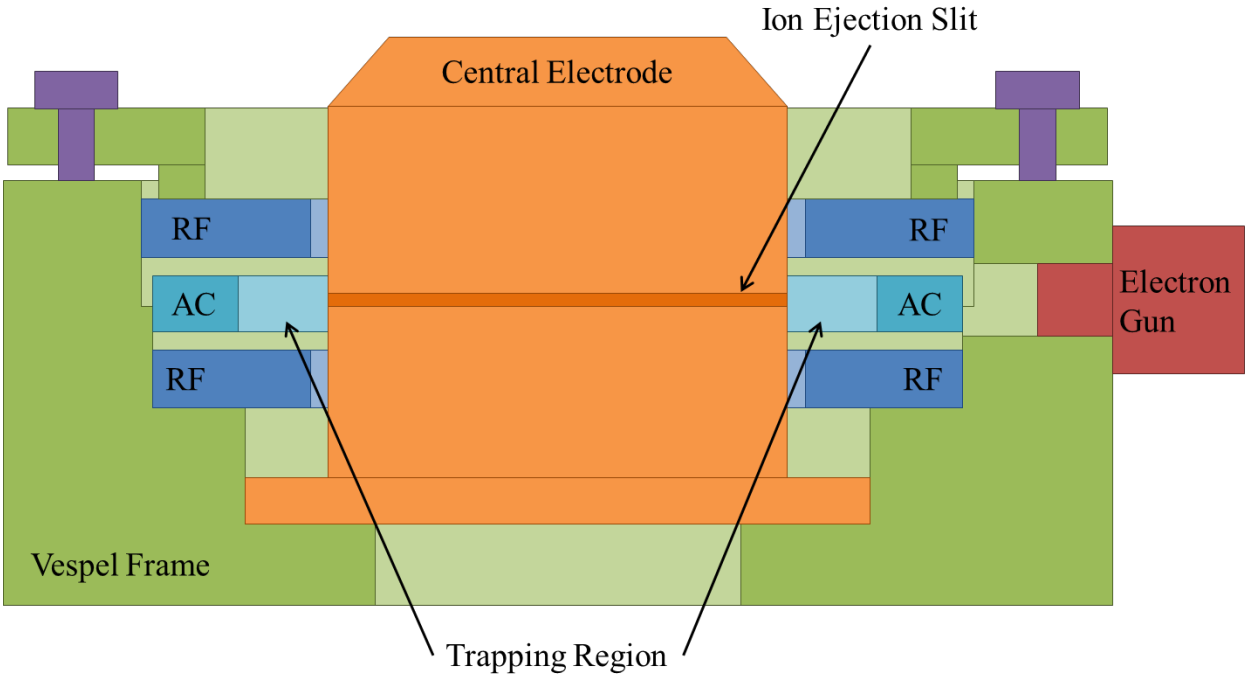

Figure 5-5: Configuration of the electrodes and Vespel frame of the third miniaturized cylindrical toroidal ion trap. (R = 11.79 mm, r_0 = 2.229 mm, z_0 = 1.934 mm)

5.4.1 Electrode Design and Trap Assembly

For alignment, we chose to mount all of the electrodes inside a frame made of Vespel. Vespel is a polyamide-based plastic produced by DuPont (Wilmington, Delaware) that has several properties useful for alignment of ion trap electrodes. Its lubricity and dimensional

stability allow for the electrodes to fit snugly within the frame, and its heat resistance allows for the trap to be heated. It also doesn't produce outgassing under vacuum. This Vespel frame was hollowed out to have four sections of different diameters matching the outer diameters of the different electrodes. The first section cut through the bottom of the frame to make room for the electron multiplier. The second section had a wider diameter of 1.0804 in. (24.7 mm) to match the smaller base of the central electrode; this would allow for the central electrode to be placed at the bottom of this section. The third section had a diameter of 1.4004 in. (35.6 mm) to match the outer diameter of the lower RF electrode and the clean cut edge of the AC electrode; the lower RF electrode would rest at the bottom of this section. The fourth section had a diameter of 1.4404 in. (36.6 mm) to match the diameter of the upper RF electrode. Machining tolerances were as low as 0.0003 in. (0.01 mm) for radial alignment.

We made all of the electrodes out of stainless steel, and we calculated more precisely the dimensions affecting the trapping region. The central electrode had an outer diameter of 0.753 in. (19.1 mm). Its slit was 0.020 in. (0.51 mm) wide with about one-quarter of it blocked where the electron gun would face. The RF electrodes were 0.100 in. (2.54 mm) thick with an inner diameter of 0.855 in. (21.7 mm). The AC electrode was 0.0983 in. (2.50 mm) thick with an inner diameter of 1.104 in. (28.04 mm). The ionization slit in the AC electrode was 0.250 in. (6.35 mm) wide and 0.040 in. (1.0 mm) tall. The upper portion of the outer diameter was cut less precisely in order to easily maintain the low tolerances in all other dimensions of the AC electrode.

A new custom electron gun was mounted on the side of the Vespel frame. The housing was made from stainless steel. In order to obtain a higher transmission of electrons from the electron gun's filament to the sample inside the trap, we designed and ordered a custom filament from Scientific Instrument Services, Inc. (Ringoes, NJ). In order to focus the electrons through the slit

in the electron gun's gate, we changed the shape of the Pierce electrode behind the filament which accelerates the ions in a direction. Simulations with SIMION 8.0 (Figure 5-6) showed improved focusing when the radius of the Pierce electrode was 0.020 in. (0.51 mm) and the total depth of the Pierce electrode was 0.035 in (0.89 mm). The filament would be 0.015 in (0.38 mm) inside the Pierce electrode.

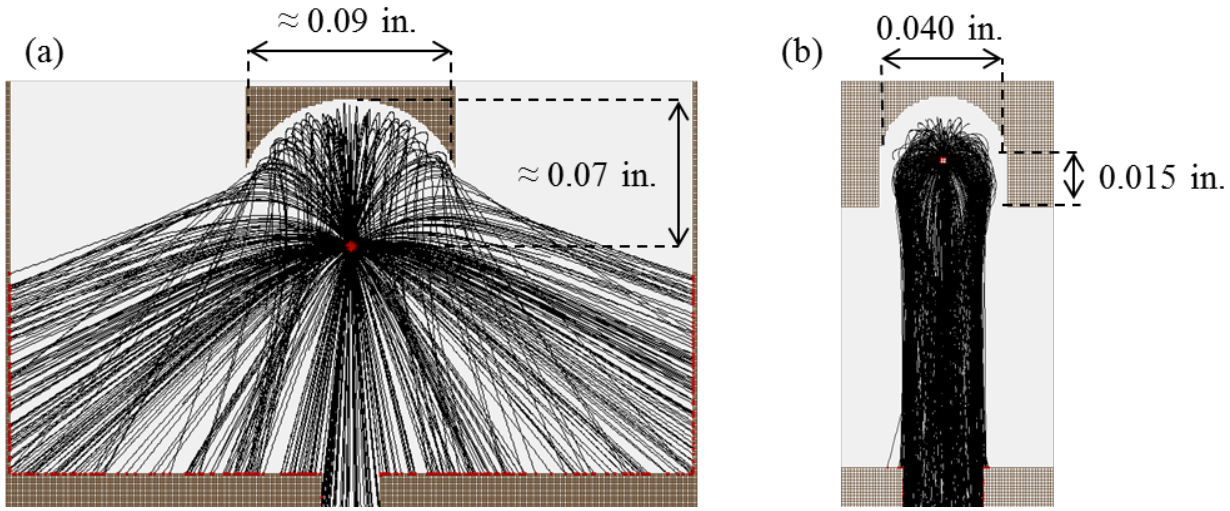

Figure 5-6: SIMION 8.0 images of a (a) commercial and (b) custom filaments to be used for the custom electron gun. (a) The smallest commercial filament by Scientific Instrument Services, Inc. (Ringoes, NJ) had a Pierce electrode that was about 0.09 in. (2.2 mm) wide and 0.07 in. (1.8 mm) from the filament. (b) The custom filament design had a Pierce electrode that was 0.040 in. (1.02 mm) wide. The bottom of the Piece electrode had a radius of curvature of 0.020 in. (0.51 mm). The filament was 0.020 in. (0.51 mm) from the Pierce electrode's bottom and 0.015 in. (0.38 mm) from the outside edge of the Pierce electrode.

For detection, we redesigned a smaller conversion dynode and an electron multiplier to allow for a 0.25 in. (6.4 mm) spacing from the inside surface of the central electrode in order to prevent possible arcing. For the conversion dynode, we used the same angles and depth as the original. We requested a customized electron multiplier from DeTech Detector Technology, Inc.

(Palmer, MA) to be tall enough to be close to the central electrode's slit while still keeping all electron multiplier parts away from the inner sides of the central electrode.

5.4.2 Setup

The new vacuum chamber was designed to be 3.60 in × 4.00 in. × 2.00 in. (91.4 mm × 101.6 mm × 50.8 mm) (Figure 5-7). A 0.375 in. (9.525 mm) glass window on top with an O-ring to seal the chamber was used for viewing and access into the chamber. The trap was mounted sideways in the trap with a bracket. SHV and multi-pin feedthroughs were used to apply voltages to the trap, electron gun, and detector, and a BNC connector was used for the signal output (MDC Vacuum Products LLC, Hayward CA). Conflat™ flanges were used to connect the chamber to the HiCube turbo-molecular vacuum pump and the D-35614 full range pressure gauge (Pfeiffer Vacuum, Asslar, Germany). A precision leak valve from Nupro/Swagelok (Solon, OH) controlled the sample pressure, and a leak valve from Granville Phillips (Boulder CO) controlled the helium pressure.

For a new RF power supply, we used the PSRF-151: High-Q Head-G Power Supply from Ardara (North Huntingdon, PA). It was designed to give about 3.42 MHz for a 140 pF test load. Because the trap's capacitance was much smaller than the test load, we added capacitors to the power supply. We applied 120 pF with capacitors, and the RF power supplies gave 3.46 MHz when applied to the trap. The maximum amplitude of the signal was about 1000 $V_{0\text{-}p}$.

We used an arbitrary waveform generator (33250A, Agilent Technologies, Santa Clara, CA) to control the amplitude of the RF ramp. For the AC signal, we used a sine wave from a function generator (DS345, Stanford Research Systems, Sunnyvale, CA). We used a previously made custom power source for the electron gun. The conversion dynode and electron multiplier

were powered by high voltage power supplies (Stanford Research Systems, Sunnyvale, CA). The signal was amplified by a current amplifier (428, Keithley, Cleaveland, OH), and displayed on an oscilloscope (Wavesurfer 42MXs-B, LeCroy, Chestnut Ridge, NY). The timing of the RF amplitude, AC signal, and electron gun gate was controlled by a pulse/delay generator (575, Berkeley Nucleonics Corp., San Rafael CA).

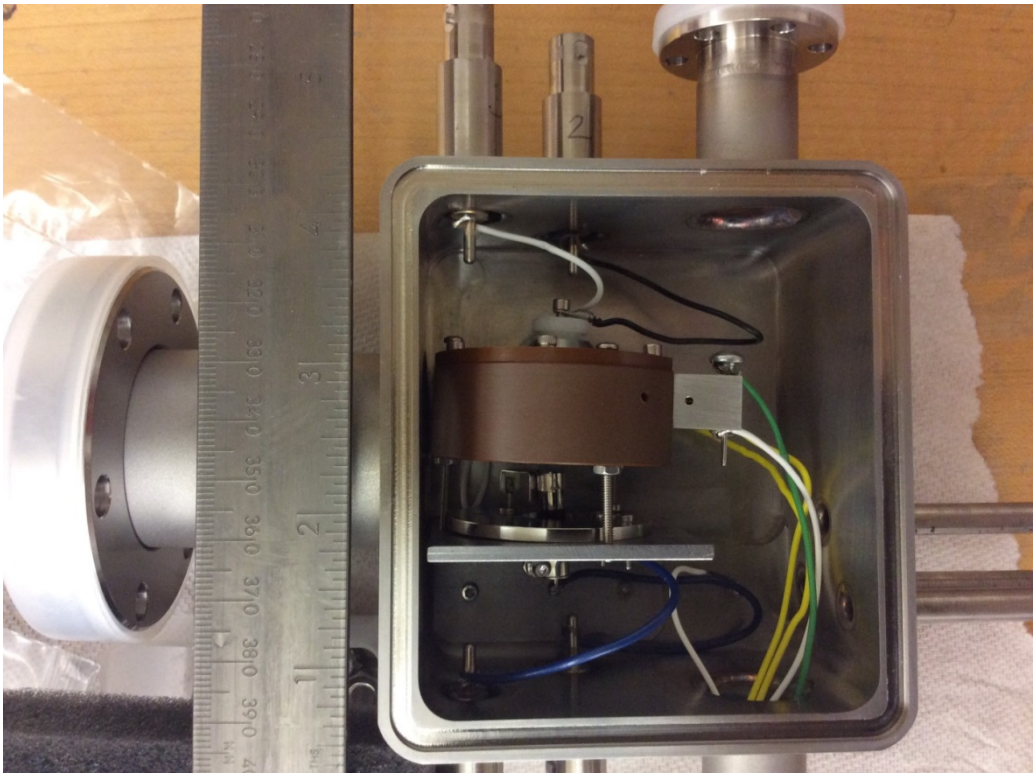

Figure 5-7: Assembly of the third miniaturized version of the cylindrical toroidal ion trap inside the vacuum chamber.

5.4.3 Performance

We are currently in the process of operating this miniaturized version of the cylindrical toroidal ion trap. We have analyzed toluene, deuterated toluene, dichloromethane, heptane, trichloroethylene, benzene, and isobutylbenzene, but we have not seen any identifiable peaks.

We have taken the trap apart and reassembled it, but we still have not been able to make the ion trap function as a mass spectrometer. It may be that the trapping dimension r_0 of the ion trap is not the one-third the size of the original dimension.

6 FUTURE WORK

6.1 Simulations of Ion Motion in Traps of Toroidal Geometry

The most recent research I have done has looked at portions of the stability diagram for ion motion in toroidal ion traps made of differing amounts of electric fields based on toroidal harmonics. The next step in this endeavor will be to look at the toroidal quadrupole ion traps with toroidal hexapole coefficients that showed highly linear fields or had reduced resonance lines. The toroidal hexapole coefficient of 1.25 had the most linear axial field. The toroidal hexapole coefficient of 2.75 showed a minimized $\beta_r + 2\beta_z = 2$ resonance line and a maximized number of stable points within the boundaries at the apex. The toroidal hexapole coefficients of 3.25 to 4 showed minimized resonance lines at $\beta_r = ⅔$ and $\beta_r + \beta_z = 1$. These toroidal quadrupole ion traps with toroidal hexapole coefficients could be further explored by both viewing the full stability diagram as well as performing mass analysis. These results could be used either to determine the factors that can be used to optimize existing toroidal ion trap mass spectrometers or to build a trap based on the toroidal quadrupole and hexapole.

6.2 Miniaturized Ion Traps based on the Cylindrical Toroidal Ion Trap

To be used in various fields, the current miniaturized cylindrical toroidal ion trap will need to demonstrate acceptable performance as a portable mass spectrometer. Adjustments may be needed in order to improve its current performance. Once its performance as a mass analyzer has been optimized, the design can be further miniaturized, and variations to the design can allow for higher trapping efficiency when using external ionization sources.

6.2.1 Current Miniaturized Cylindrical Toroidal Ion Trap

The current miniature version of the cylindrical toroidal ion trap has not yet shown optimized resolution for mass analysis. One factor affecting its performance is that the r_0 for this design turned out larger than originally intended (2.229 mm instead of 1.965 mm). If with more experimentation the resolution has not been improved, it may be necessary to remake one or more of the electrodes to correct for this. Either the AC electrode's inner diameter can be reduced to 1.063 in. (27.00 mm) or the central electrode's outer diameter can be increased to 0.794 in. (20.16 mm). If the central electrode's outer diameter is increased, the space between the central electrode and the RF electrodes would be 0.031 in. (0.79 mm); it may also be necessary to increase the inner diameter of the RF electrodes in order to increase this space and prevent arcing.

6.2.2 Further Miniaturization of the Cylindrical Toroidal Ion Trap

Once the performance of the miniature cylindrical toroidal ion trap has been optimized, further miniaturization can be performed for a more portable mass spectrometer. One method of manufacturing the electrodes would be to make the RF and AC electrodes out of sheet metal. Sheet metal has uniform thickness and the shape of the electrodes can be easily repeated when punch-cutting the sheet metal. This may cause one side of the cut to have a rounded edge and the other side to have a sharper edge. This can be corrected for by lightly sanding the side with the sharper edges. Thicknesses that can be used for a miniaturized ion trap can range from gauge 7 (0.1875 in. or 4.76 mm) down to gauge 30 (0.011 in. or 0.279 mm).

With further miniaturization, ion capacity will be decreased. In order to maintain signal intensity, we can assemble an array of miniaturized cylindrical toroidal ion traps. One possible design stacks the individual traps one on top of another (Figure 6-1). The RF electrodes of one

trap in the array would be shared with the traps above and below. The central electrode would have several slits, one slit for each trap in the array.

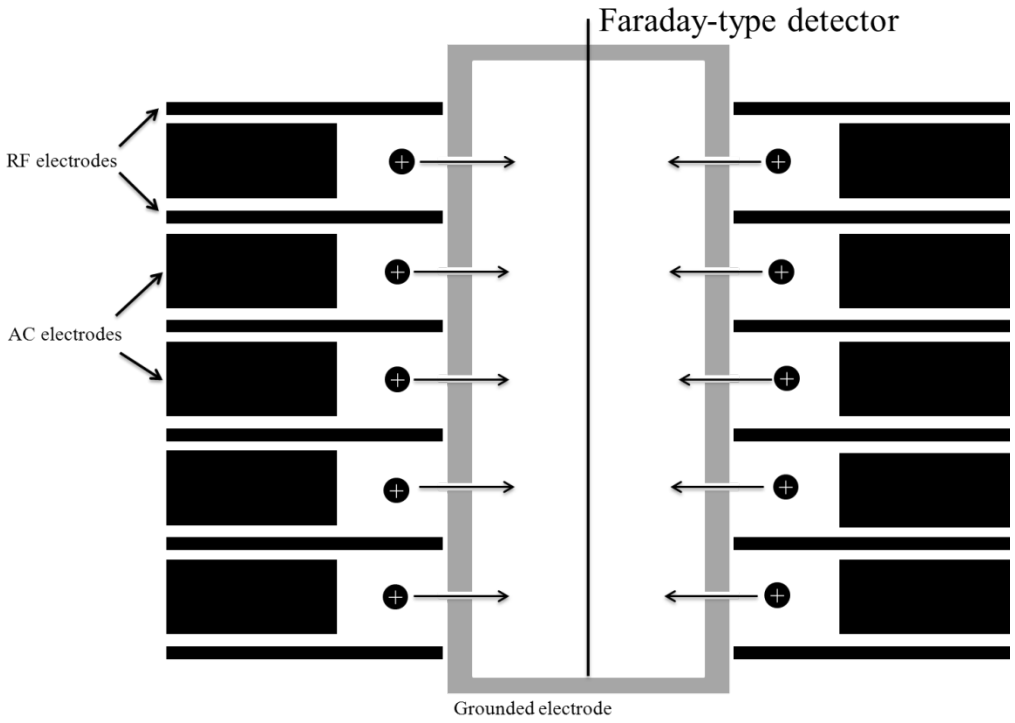

Figure 6-1: Schematic of an array of cylindrical toroidal ion traps with a Faraday wire for a charge detector. (Adapted from D. E. Austin and N. R. Taylor, "Toroidal Ion Trap Mass Analyzer with Cylindrical Electrodes". US Patent 8,642,955 B2, 4 Feb. 2014. [148])

If the central electrode is smaller, it may be necessary to use a different detection system such as a charge detector. Using a wire as a charge-collector, the charge collected on the wire can be used to control the current passing through a junction gate field-effect transistor (JFET). The current can be amplified and converted to a voltage that can be read on an oscilloscope; this voltage signal would need to be differentiated to convert the rise-time to signal peaks.

6.2.3 Design Variations for External Ionization Sources

Currently, the cylindrical toroidal ion trap is designed for electron ionization of gaseous sample molecules already inside the trapping volume. To eliminate some of the sample preparation and allow for samples not volatile enough to be ionized in the gas phase, other ionization sources can produce ions outside the vacuum system, such as electrospray ionization (ESI), matrix-assisted laser desorption-ionization (MALDI), desorption electrospray ionization (DESI), direct analysis in real time (DART), and other various methods [149].

In order to use these methods of ionization with the cylindrical toroidal ion trap, we need a way to efficiently inject the ions into the trap. Traps like the QIT can have external ions injected through the exit slits so that the ions pass through the electric field. Traps like the LIT can have external ions injected axially so that the ions pass through perpendicular to the trapping fields. In both cases, buffer gas pressure is usually increased to reduce the kinetic energy and velocity of the ions to prevent them from passing through.

For the cylindrical toroidal ion trap, a change to the design would be needed in order to provide a way for the ions to be injected. One way to do this would be to add an ion guide like the RIT tangentially to the trapping volume. Because the shape of this design is similar to the Greek letter ρ (rho), this design can be called the ρ-trap (Figure 6-2). For electron ionization, an electron gun can be mounted to the ion guide portion of the ρ-trap. External ions can be injected through a slit in the end electrode of the ion guide. Once the ions are in the ion guide, a voltage pulse from the end electrode can push the ions towards the toroidal trapping region of the ρ-trap. One issue is the effect of the attachment of the ion guide to the trapping fields of the toroidal ion trap. To prevent ions being ejected at the wrong time of the RF ramp, the slit in the central electrode can be blocked at the intersection of the ion guide and toroidal trap. This design for an

ion trap of toroidal geometry can be implemented at any point in the miniaturization of the cylindrical toroidal ion trap. Once a miniaturized cylindrical toroidal ion trap has demonstrated sufficient performance, a ρ-trap with the same trapping dimensions can be designed to test the performance when an ion guide is attached to the toroidal trapping volume.

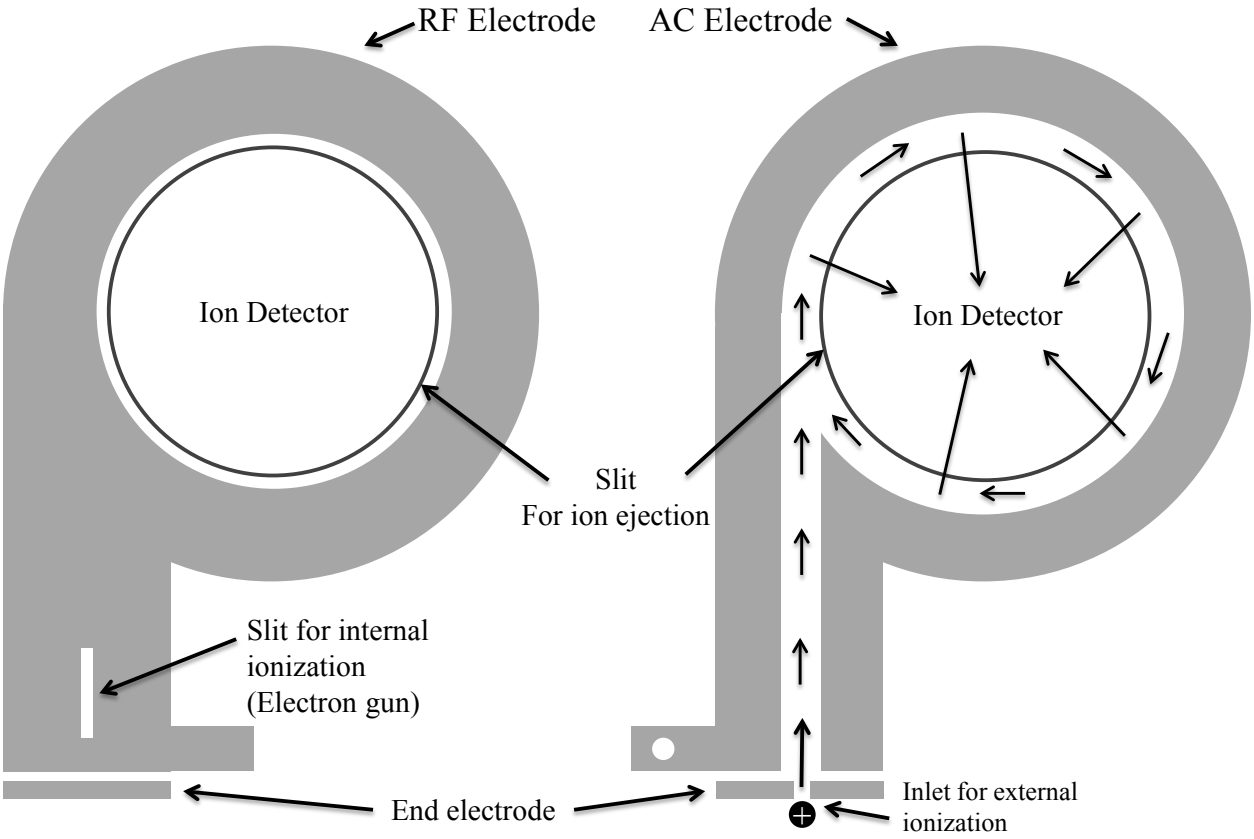

Figure 6-2: The ρ-Trap (RHO-Trap). To allow for both kinds of ionization, the RF electrode has a slit for internal ionization while the end electrode has an inlet for external ionization. (Adapted from D. E. Austin and N. R. Taylor, "Toroidal Ion Trap Mass Analyzer with Cylindrical Electrodes". US Patent 8,642,955 B2, 4 Feb. 2014. [148])

REFERENCES

[1] A. J. Dempster, "A New Method of Positive Ray Analysis," *Phys. Rev.,* vol. 11, no. 4, p. 316–325, 1918.

[2] F. W. Aston, "Constitution of the Elements," *Nature,* vol. 104, no. 2616, p. 393, 1919.

[3] S. Maher, F. P. M. Jjunju and S. Taylor, "Colloquium: 100 Years of Mass Spectrometry: Perspectives and Future Trends," *Rev. Mod. Phys.,* vol. 87, no. 1, p. 113–135, 2015.

[4] R. A. Ketola, T. Kotiaho, M. E. Cisper and T. M. Allen, "Environmental Applications of Membrane Introduction Mass Spectrometry," *J. Mass Spectrom.,* vol. 37, no. 5, p. 457–476, 2002.

[5] S. D. Richardson, "Environmental Mass Spectrometry," *Anal. Chem.,* vol. 72, no. 18, p. 4477–4496, 2000.

[6] J. J. Mosher, G. C. Klein, A. G. Marshall and R. H. Findlay, "Influence of Bedrock Geology on Dissolved Organic Matter Quality in Stream Water," *Org. Geochem.,* vol. 41, no. 11, p. 1177–1188, 2010.

[7] C. Van Poucke, F. Dumoulin, S. Yakkundi, C. Situ, C. T. Elliott, E. M. Grutters, R. Verheijen, R. Schilt, S. Eriksson and C. Van Peteghem, "Banned Antibacterial Growth Promoters in Animal Feed: Collaborative Trial on the Liquid Chromatography-Tandem Mass Spectrometry Method Developed in the Feedstuffs-Radius Project," *Anal. Chim. Acta,* vol. 557, no. 1–2, p. 204–210, 2006.

[8] P. A. Smith, C. R. Jackson Lepage, D. Koch, H. D. M. Wyatt, G. L. Hook, G. Betsinger, R. P. Erickson and B. A. Eckenrode, "Detection of Gas-Phase Chemical Warfare AgentsUsing Field-Portable Gas Chromatography-Mass Spectrometry Systems: Instrument and Sampling Strategy Considerations," *Trends Anal. Chem.,* vol. 23, no. 4, p. 296–306, 2004.

[9] S. G. Ler, F. K. Lee and P. Gopalakrishnakone, "Trends in Detection of Warfare Agents Detection Methods for Ricin, Staphylococcal Enterotoxin B and T-2 Toxin," *J. Chromatogr. A,* vol. 1133, no. 1–2, p. 1–12, 2006.

[10] C. C. Mulligan, D. R. Justes, R. J. Noll, N. L. Sanders, B. C. Laughlin and R. G. Cooks, "Direct Monitoring of Toxic Compounds in Air Using a Portable Mass Spectrometer," *Analyst,* vol. 131, no. 4, p. 556–567, 2006.

[11] J. Yinon, "Forensic Applications of Mass Spectrometry," *Mass Spectrom. Rev.,* vol. 10, no. 3, p. 179–224, 1991.

[12] S. Petrie and D. K. Bohme, "Ions in Space," *Mass Spectrom. Rev.,* vol. 26, no. 2, p. 258–280, 2007.

[13] W. B. Brinckerhoff, F. H. W. van Amerom, R. M. Danell, V. Pinnick, R. Arevalo, M. Atanassova, L. Hovmand, P. R. Mahaffy, R. J. Cotter and M. Team, "A Dual Source Ion

Trap Mass Spectrometer for the Mars Organic Molecule Analyzer on ExoMars 2018," *EPC Abstracts,* vol. 6, no. DPS2011, p. 1337, 2011.

[14] V. Lopez-Avila and H. H. Hill, "Field Analytical Chemistry," *Anal. Chem.,* vol. 69, no. 12, p. 289–305, 1997.

[15] A. Trimborn, K. -P. Hinz and B. Spengler, "Online Analysis of Atmospheric Particles with a Transportable Laser Mass Spectrometer," *Aerosol Sci. Technol.,* vol. 33, no. 1–2, p. 191–201, 2000.

[16] P. A. Smith, M. T. A. Roe, C. Sadowski and E. D. Lee, "Unknown Exposures: Gaps in Basic Characterization Addressed with Person-Portable Gas Chromatography-Mass Spectrometry Instrumentation," *J. Occup. Environ. Hyg.,* vol. 8, no. 3, p. 129–138, 2011.

[17] P. I. Hendricks, J. K. Dalgleish, J. T. Shelley, M. A. Kirleis, M. T. McNicholas, L. Li, T.-C. Chen, C.-H. Chen, J. S. Duncan, F. Boudreau, R. J. Noll, J. P. Denton, T. A. Roach and Z. Ouyang, "Autonomous in Situ Analysis and Real-Time Chemical Detection Using a Backpack Miniature Mass Spectrometer: Concept, Instrumentation Development, and Performance," *Anal. Chem.,* vol. 86, no. 6, p. 2900–2908, 2014.

[18] L. J. Kricka, "Miniaturization of Analytical Systems," *Clin. Chem.,* vol. 44, no. 9, p. 2008–2014, 1998.

[19] E. R. Badman and R. G. Cooks, "Miniature Mass Analyzers," *J. Mass Spectrom.,* vol. 35, no. 6, p. 659–671, 2000.

[20] W. Paul and H. Steinwedel, "Ein Neues Massenspektrometer ohne Magnetfeld," *Z. Naturforsch. A,* vol. 8, p. 448–450, 1953.

[21] A. Keil, N. Talaty, C. Janfelt, R. J. Noll, L. Gao, Z. Ouyang and R. G. Cooks, "Ambient Mass Spectrometry with a Handheld Mass Spectrometer at High Pressure," *Anal. Chem.,* vol. 79, no. 20, p. 7734–7739, 2007.

[22] A. Keil, H. Hernandez-Soto, R. J. Noll, M. Fico, L. Gao, Z. Ouyang and R. G. Cooks, "Monitoring of Toxic Compounds in Air Using a Handheld Rectilinear Ion Trap Mass Spectrometer," *Anal. Chem.,* vol. 80, no. 3, p. 734–741, 2008.

[23] Y. Peng and D. E. Austin, "New Approaches to Miniaturizing Ion Trap Mass Analyzers," *Trends Anal. Chem.,* vol. 30, no. 10, p. 1560–1567, 2011.

[24] E. Fischer, "Die Dreidimensionale Stabilisierung von Ladungsträgern in einem Vierpolfeld," *Zeitschrift für Physik,* vol. 156, no. 1, p. 1–26, 1959.

[25] R. E. March and J. F. J. Todd, Quadrupole Ion Trap Mass Spectrometry, Second Edition, Hoboken, NJ: Wiley-Interscience, 2005.

[26] W. Paul, *Electromagnetic Traps for Charged and Neutral Particles,* Stockholm: The Nobel Foundation, 1989.

[27] H. G. Dehmelt, *Experiments with an Isolated Subatomic Particle at Rest,* Stockholm: The Nobel Foundation, 1989.

[28] D. J. Wineland, *Superposition, Entanglement, and Raising Schröedinger´s Cat,* Stockholm: The Nobel Foundation, 2012.

[29] C. Monroe, D. M. Meekhof, B. E. King, W. M. Itano and D. J. Wineland, "Demonstration of a Fundamental Quantum Logic Gate," *Phys. Rev. Lett.,* vol. 75, no. 25, p. 4714–4717, 1995.

[30] C. Ospelkaus, U. Warring, Y. Colombe, K. R. Brown, J. M. Amini, D. Leibfried and D. J. Wineland, "Microwave Quantum Logic Gates for Trapped Ions," *Nature,* vol. 476, no. 7359, p. 181–184, 2011.

[31] J. J. Bollinger, J. D. Prestage, W. M. Itano and D. J. Wineland, "Laser-Cooled-Atomic Frequency Standard," *Phys. Rev. Lett.,* vol. 54, no. 10, p. 1000–1003, 1985.

[32] J. D. Prestage, G. J. Dick and L. Maleki, "New Ion Trap for Frequency Standard Applications," *J. Appl. Phys.,* vol. 66, no. 3, p. 1013–1017, 1989.

[33] J. J. Bollinger, D. J. Heinzen, W. M. Itano, S. L. Gilbert and D. J. Wineland, "A 303-MHz Frequency Standard Based on Trapped Be+ Ions," *IEEE Trans. Instrum. Meas.,* vol. 40, no. 2, p. 126–128, 1991.

[34] H. G. Dehmelt, "Radiofrequency Spectroscopy of Stored Ions I: Storage," *Adv. At. Mol. Phys.,* vol. 3, p. 53–72, 1967.

[35] H. G. Dehmelt, "Radiofrequency Spectroscopy of Stored Ions II: Spectroscopy," *Adv. At. Mol. Phys.,* vol. 5, p. 109–154, 1969.

[36] N. Polfer, B. G. Sartakov and J. Oomens, "The Infrared Spectrum of the Adamantyl Cation," *Chem. Phys. Lett.,* vol. 400, no. 1–3, p. 201–205, 2004.

[37] Q. Bian, M. W. Forbes, F. O. Talbot and R. A. Jockusch, "Gas-Phase Fluorescence Excitation and Emission Spectroscopy of Mass-Selected Trapped Molecular Ions," *Phys. Chem. Chem. Phys.,* vol. 12, no. 11, p. 2590–2598, 2010.

[38] J. F. J. Todd, "Chapter 1: Introduction to Practical Aspects of Ion Trap Mass Spectrometry," in R.E. March, J.F.J. Todd (Eds.), *Practical Aspects of Ion Trap Mass Spectrometry, vol. 1*, New York, USA, CRC Press, 1995, p. 3–24.

[39] R. E. March and F. A. Londry, "Chapter 2: Theory of Quadrupole Mass Spectrometry," in R.E. March, J.F.J. Todd (Eds.), *Practical Aspects of Ion Trap Mass Spectrometry, vol. 1*, New York, USA, CRC Press, 1995, p. 25–48.

[40] R. D. Knight, "The General Form of the Quadrupole Ion Trap Potential," *Int. J. Mass Spectrom. Ion Phys.,* vol. 51, no. 1, p. 127–131, 1983.

[41] R. E. March, "Quadrupole Ion Traps," *Mass Spectrom. Rev.,* vol. 28, no. 6, p. 961–989, 2009.

[42] G. C. Stafford Jr., P. E. Kelley, J. E. P. Syka, W. E. Reynolds and J. F. J. Todd, "Recent Improvements in and Analytical Applications of Advanced Ion Trap Technology," *Int. J. Mass Spectrom. Ion Processes,* vol. 60, no. 1, p. 85–98, 1984.

[43] G. C. Stafford, P. E. Kelley and D. R. Stephens, "Method of Mass Analyzing a Sample by Use of a Quadrupole Ion Trap". U.S. Patent 4,540,884, 10 September 1985.

[44] J. F. J. Todd, A. D. Penman and R. D. Smith, "Some Alternative Scanning Methods for the Ion Trap Mass Spectrometer," *Int. J. Mass Spectrom. Ion Processes,* vol. 106, p. 117–135, 1991.

[45] J. Franzen, R. Gabling, M. Schubert and Y. Wang, "Chapter 3: Nonlinear Ion Traps," in R.E. March, J.F.J. Todd (Eds.), *Practical Aspects of Ion Trap Mass Spectrometry, vol. 1*, New York, USA, CRC Press, 1995, p. 49–167.

[46] J. P. Guzowski Jr. and G. M. Hieftje, "Charateristics of a RF-only Hexapole Ion-Guide Interface For Plasma-Source Time-of-Flight Mass Spectrometry," *J. Anal. At. Spectrom.,* vol. 16, no. 8, p. 781–792, 2001.

[47] P. Tosi, G. Fontana, S. Longano and D. Bassi, "Transport of an Ion Beam Through an Octopole Guide Operating in the R.F.-only Mode," *Int. J. Mass Spectrom. Ion Processes,* vol. 93, no. 1, p. 95–105, 1989.

[48] C. Hägg and I. Szabo, "New Ion-Optical Devices Utilizing Oscillatory Electric Fields. II. Stability of Ion Motion in a Two-Dimensional Hexapole Field," *Int. J. Mass Spectrom. Ion Processes,* vol. 73, no. 3, p. 237–275, 1986.

[49] C. Hägg and I. Szabo, "New Ion-Optical Devices Utilizing Oscillatory Electric Fields. III. Stability of Ion Motion in a Two-Dimensional Octopole Field," *Int. J. Mass Spectrom. Ion Processes,* vol. 73, no. 3, p. 277–294, 1986.

[50] J. Franzen, "Simulation Study of an Ion Cage with Superimposed Multipole Fields," *Int. J. Mass Spectrom. Ion Processes,* vol. 106, p. 63–78, 1991.

[51] P. Hendricks, J. Duncan, R. J. Noll, Z. Ouyang and R. G. Cooks, "Performance of a Low Voltage Ion Trap," *Int. J. Mass Spectrom.,* vol. 305, no. 1, p. 69–73, 2011.

[52] S. Pau, C. S. Pai, Y. L. Low, J. Moxom, P. T. A. Reilly, W. B. Whitten and J. M. Ramsey, "Microfabricated Quadrupole Ion Trap for Mass Spectrometer Applications," *Phys. Rev. Lett.,* vol. 96, no. 12, p. 120801, 2006.

[53] W. Neuhauser, M. Hohenstatt, P. Toschek and H. Dehmelt, "Optical-Sideband Cooling of Visible Atom Cloud Confined in Parabolic Well," *Phys. Rev. Lett.,* vol. 41, no. 4, p. 233–236, 1978.

[54] R. E. Kaiser, R. G. Cooks, J. Moss and P. H. Hemberger, "Mass Range Extension in a Quadrupole Ion-Trap Mass Spectrometer," *Rapid Commun. Mass Spectrom.,* vol. 3, no. 2, p. 50–53, 1989.

[55] Y. Tian, J. Higgs, A. Li, B. Barney and D. E. Austin, "How Far Can Ion Trap Miniaturization Go? Parameter Scaling and Space-Charge Limits for Very Small Cylindrical Ion Traps," *J. Mass Spectrom.,* vol. 49, no. 3, p. 233–240, 2014.

[56] J. C. Schwartz, M. W. Senko and J. E. P. Syka, "A Two-Dimensional Quadrupole Ion Trap Mass Spectrometer," *J. Am. Soc. Mass Spectrom.,* vol. 13, no. 6, p. 659–669, 2002.

[57] E. C. Beaty, "Simple Electrodes for Quadrupole Ion Traps," *J. Appl. Phys.,* vol. 61, no. 6, p. 2118–2122, 1987.

[58] D. B. Langmuir, R. V. Langmuir, H. Shelton and R. F. Wuerker, "Containment Device". U. S. Patent 3,065,640, 27 Nov. 1962.

[59] Z. Ouyang and R. G. Cooks, "Rectilinear Ion Trap and Mass Analyzer System and Method". US Patent 6,838,666, 4 January 2005.

[60] M. E. Bier and J. E. P. Syka, "Ion Trap Mass Spectrometer System and Method". US Patent 5,420,425, 30 May 1995.

[61] S. A. Lammert, W. R. Plass, C. V. Thompson and M. B. Wise, "Design, Optimization and Initial Performance of a Toroidal RF Ion Trap Mass Spectrometer," *Int. J. Mass Spectrom.,* vol. 212, p. 25–40, 2001.

[62] W. Paul and H. Steinwedel, "Apparatus for Separating Charged Particles of Different Specific Charges". United States Patent 2,939,952, 7 June 1960.

[63] P. H. Dawson and N. R. Whetten, "Three-dimensional Mass Spectrometer and Gauge". U.S. Patent 3,527,939, 8 September 1970.

[64] J. E. P. Syka, "Chapter 4: Commercialization of the Quadrupole Ion Trap," in R.E. March, J.F.J. Todd (Eds.), *Practical Aspects of Ion Trap Mass Spectrometry, vol. 1*, New York, USA, CRC Press, 1995, p. 169–205.

[65] J. Louris, J. Schwartz, G. Stafford, J. Syka and D. Taylor, "The Paul Ion Trap Mass Selective Instability Scan: Trap Geometry and Resolution," in *The 40th ASMS Conference on Mass Spectrometry and Allied Topics*, Washington, DC, 1992.

[66] M.-N. Benilan and C. Audoin, "Confinement D'Ions Par Un Champ Electrique De Radiofrequence Dans Une Cage Cylindrique," *Int. J. Mass Spectrom. Ion Phys.,* vol. 11, no. 5, p. 421–432, 1973.

[67] R. F. Bonner, J. E. Fulford, R. E. March and G. F. Hamilton, "The Cylindrical Ion Trap. Part I. General Introduction," *Int. J. Mass Spectrom. Ion Phys.,* vol. 24, no. 3, p. 255–269, 1977.

[68] W.-W. Lee, C.-H. Oh, P.-S. Kim, M. Yang and K. Song, "Characteristics of Cylindrical Ion Trap," *Int. J. Mass Spectrom.,* vol. 230, no. 1, p. 25–31, 2003.

[69] J. M. Wells, E. R. Badman and G. R. Cooks, "A Quadrupole Ion Trap with Cylindrical Geometry Operated in the Mass-Selective Instability Mode," *Anal. Chem.,* vol. 70, no. 3, p. 438–444, 1998.

[70] E. R. Badman, R. C. Johnson, W. R. Plass and R. G. Cooks, "A Miniature Cylindrical Quadrupole Ion Trap: Simulation and Experiment," *Anal. Chem.,* vol. 70, no. 23, p. 4896–4901, 1998.

[71] O. Kornienko, P. T. A. Reilly, W. B. Whitten and J. M. Ramsey, "Micro Ion Trap Mass Spectrometry," *Rapid Commun. Mass Spectrom.,* vol. 13, no. 1, p. 50–53, 1999.

[72] A. V. Jesseph, J. D. Fox and G. F. Verbeck IV, "Ion Isolation and Collision-Induced Dissociation in a 0.5 mm r_0 Cylindrical Ion Trap," *Int. J. Mass Spectrom.,* vol. 295, no. 3, p. 149–152, 2010.

[73] G. Wu, R. G. Cooks and Z. Ouyang, "Geometry Optimization for the Cylindrical Ion Trap: Field Calculations, Simulations and Experiments," *Int. J. Mass Spectrom.,* vol. 241, no. 2–3, p. 119–132, 2005.

[74] E. R. Badman and R. G. Cooks, "A Parallel Miniature Cylindrical Ion Trap Array," *Anal. Chem.,* vol. 72, no. 14, p. 3291–3297, 2000.

[75] H. Peddanenikalva, K. Potluri, S. Bhansal, R. T. Short and D. Fries, "64.4: A Microfabrication Strategy for Cylindrical Ion Trap Mass Spectrometer Arrays," in *Proceedings of IEEE Sensors*, Orlando, FL, 2002.

[76] M. G. Blain, L. S. Riter, D. Cruz, D. E. Austin, G. Wu, W. R. Plass and R. G. Cooks, "Towards the Hand-Held Mass Spectrometer: Design Considerations, Simulation, and Fabrication of Micrometer-Scaled Cylindrical Ion Traps," *Int. J. Mass Spectrom,* vol. 236, no. 1–3, p. 91–104, 2004.

[77] D. Cruz, J. P. Chang, M. Fico, A. J. Guymon, D. E. Austin and M. G. Blain, "Design, Microfabrication, and Analysis of Micrometer-Sized Cylindrical Ion Trap Arrays," *Rev. Sci. Instrum.,* vol. 78, no. 1, p. 015107, 2007.

[78] F. H. W. Van Amerom, A. Chaudhary, M. Cardenas, J. Bumgarner and R. T. Short, "Microfabrication of Cylindrical Ion Trap Mass Spectrometer Arrays for Handheld Chemical Analyzers," *Chem. Eng. Commun.,* vol. 195, no. 2, p. 98–114, 2008.

[79] D. J. Douglas, A. J. Frank and D. Mao, "Linear Ion Traps in Mass Spectrometry," *Mass Spectrom. Rev.,* vol. 24, no. 1, p. 1–29, 2004.

[80] R. E. March and J. F. J. Todd, "Chapter 1: An Appreciation and Historical Survey of Mass Spectrometry," in R.E. March, J.F.J. Todd (Eds.), *Practical Aspects of Trapped Ion Mass Spectrometry, vol. 4*, New York, USA, CRC Press, 2010, p. 3–168.

[81] J. M. Campbell, B. A. Collings and D. J. Douglas, "A New Linear Ion Trap Time-of-Fight System with Tandem Mass Spectrometry Capabilities," *Rapid Comm. Mass Spectrom.,* vol. 12, no. 20, p. 1463–1474, 1998.

[82] J. W. Hager, "A New Linear Ion Trap Mass Spectrometer," *Rapid Commun. Mass Spectrom.,* vol. 16, no. 6, p. 512–526, 2002.

[83] D. A. Church, "Storage-Ring Ion Trap Derived from the Linear Quadrupole Radio-Frequency Mass Filter," *J. Appl. Phsy.,* vol. 40, no. 8, p. 3127–3134, 1969.

[84] B. I. Deutch, F. M. Jacobsen, L. H. Andersen, P. Hvelplund, H. Knudsen, M. H. Holzscheiter, M. Charlton and G. Laricchia, "Antihydrogen Production by Positronium-Antiproton Collisions in an Ion Trap," *Phys. Scr.,* vol. 1988, no. T22, p. 248–255, 1988.

[85] I. Waki, S. Kassner, G. Birkl and H. Walther, "Observation of Ordered Stuctures of Laser-Cooled Ions in a Quadrupole Storage Ring," *Phys. Rev. Lett.,* vol. 68, no. 13, p. 2007–2010, 1992.

[86] C. Beaugrand, G. Devant, D. Jaouen, H. Mestdagh and C. Rolando, "Ion Confinement in the RF-Only Collision Cell of a Tandem Quadrupole Instrument," *Spectros. Int. J.,* vol. 5, p. 265–272, 1987.

[87] C. Beaugrand, D. Jaouen, H. Mestdagh and C. Rolando, "Ion Confinement in the Collision Cell of a Multiquadrupole Mass Spectrometer: Access to Chemical Equilibrium and Determination of Kinetic and Thermodynamic Parameters of an Ion-Molecule Reaction," *Anal. Chem.,* vol. 61, no. 13, p. 1447–1453, 1989.

[88] G. G. Dolnikowski, M. J. Kristo, C. G. Enke and J. T. Watson, "Ion-Trapping Technique for Ion/Molecule Reaction Studies in the Center Quadrupole of a Triple Quadrupole Mass Spectrometer," *Int. J. Mass Spectrom. Ion. Proc.,* vol. 82, no. 1–2, p. 1–15, 1988.

[89] M. Welling, H. A. Schuessler, R. I. Thompson and H. Walther, "Ion/Molecule Reactions, Mass Spectrometry and Optical Spectroscopy in a Linear Ion Trap," *Int. J. Mass Spectrom. Ion Processes,* vol. 172, no. 1–2, p. 95–114, 1998.

[90] J. W. Hager, "Axial Ejection in a Multipole Mass Spectrometer". U.S. Patent 6,177,668, 23 January 2001.

[91] S. A. Smith, C. C. Mulligan, Q. Song, R. J. Noll, R. G. Cooks and Z. Ouyang, "Chapter 2: Ion Trap for Miniature, Multiplexed, and Soft-Landing Technologies," in R.E. March, J.F.J. Todd (Eds.), *Practical Aspects of Trapped Ion Mass Spectrometry, vol. 4*, New York, USA, CRC Press, 2010, p. 169–247.

[92] Z. Ouyang, G. Wu, Y. Song, H. Li, W. R. Plass and R. G. Cooks, "Rectilinear Ion Trap: Concepts, Calculations, and Analytical Performance of a New Mass Analyzer," *Anal. Chem.,* vol. 76, no. 16, p. 4595–4605, 2004.

[93] Q. Song, S. Kothari, M. A. Senko, J. C. Schwartz, J. W. Amy, G. C. Stafford, R. G. Cooks and Z. Ouyang, "Rectilinear Ion Trap Mass Spectrometer with Atmospheric

Pressure Interface and Electrospray Ionization Source," *Anal. Chem.,* vol. 78, no. 3, p. 718–725, 2006.

[94] Y. Song, G. Wu, Q. Song, R. G. Cooks, Z. Ouyang and W. R. Plass, "Novel Linear Ion Trap Mass Analyzer Composed of Four Planar Electrodes," *J. Am. Soc. Mass Spectrom.,* vol. 17, no. 4, p. 631–639, 2006.

[95] A. M. Tabert, M. P. Goodwin, J. S. Duncan, C. D. Fico and R. G. Cooks, "Multiplexed Rectilinear Ion Trap Mass Spectrometer for High-Throughput Analysis," *Anal. Chem.,* vol. 78, no. 14, p. 4830–4838, 2006.

[96] W.-P. Peng, M. P. Goodwin, Z. Nie, M. Volný, Z. Ouyang and R. G. Cooks, "Ion Soft Landing Using a Rectilinear Ion Trap Mass Spectrometer," *Anal. Chem.,* vol. 80, no. 17, p. 6640–6649, 2008.

[97] D. E. Austin and S. A. Lammert, "Chapter 6: Ion Traps with Circular Geometries," in R.E. March, J.F.J. Todd (Eds.), *Practical Aspects of Trapped Ion Mass Spectrometry, vol. 4*, New York, USA, CRC Press, 2010, p. 373–398.

[98] S. A. Lammert, A. A. Rockwood, M. Wang, M. L. Lee, E. D. Lee, S. E. Tolley, J. R. Oliphant, J. L. Jones and R. W. Waite, "Miniature Toroidal Radio Frequency Ion Trap Mass Analyzer," *J. Am. Soc. Mass Spectrom.,* vol. 17, no. 7, p. 916–922, 2006.

[99] J. A. Contreras, J. A. Murray, S. E. Tolley, J. L. Oliphant, H. D. Tolley, S. A. Lammert, E. D. Lee, D. W. Later and M. L. Lee, "Hand-Portable Gas Chromatograph-Toroidal Ion Trap Mass Spectrometer (GC-TMS) for Detection of Hazardous Compounds," *J. Am. Soc. Mass Spectrom.,* no. 19, p. 1425–1434, 2008.

[100] N. R. Taylor and D. E. Austin, "A Simplified Toroidal Ion Trap Mass Analyzer," *Int. J. Mass Spectrom.,* vol. 321–322, p. 25–32, 2012.

[101] M. W. Forbes, M. Sharifi, T. Croley, L. Z. and R. E. March, "Simulation of Ion Trajectories in a Quadrupole Ion Trap: a Comparison of Three Simulation Programs," *J. Mass Spectrom.,* vol. 34, no. 12, p. 1219–1239, 1999.

[102] H.-P. Reiser, R. K. Julian Jr. and R. G. Cooks, "A Versitile Method of Simulation of the Operation of Ion Trap Mass Spectrometers," *Int. J. Mass Spectrom. Ion Processes,* vol. 121, no. 1–2, p. 49–63, 1992.

[103] R. K. Julian, M. Nappi, C. Weil and R. G. Cooks, "Multiparticle Simulation of Ion Motion in the Ion Trap Mass Spectrometer: Resonant and Direct Current Pulse Excitation," *J. Am. Soc. Mass Spectrom.,* vol. 6, no. 1, p. 57–70, 1995.

[104] C. Weil, M. Nappi, C. D. Cleven, H. Wollnik and R. G. Cooks, "Multiparticle Simulation of Ion Injection into the Quadrupole Ion Trap Under the Influence of Helium Buffer Gas Using Short Injection Times and DC Pulse Potentials," *Rapid Commun. Mass Spectrom.,* vol. 10, no. 7, p. 742–750, 1996.

[105] M. Nappi, C. Weil, C. D. Cleven, L. A. Horn, H. Wollnik and R. G. Cooks, "Visual Representations of Simulated Three-Dimensional Ion Trajectories in an Ion Trap Mass Spectrometer," *Int. J. Mass Spectrom. Ion Processes,* vol. 161, no. 1–3, p. 77–85, 1997.

[106] H. A. Bui and R. G. Cooks, "Windows Version of the Ion Trap Simulation Program ITSIM: A Powerful Heuristic and Predictive Tool in Ion Trap Mass Spectrometry," *J. Mass Spectrom.,* vol. 33, no. 4, p. 297–304, 1998.

[107] R. E. March, F. A. Londry, R. L. Alfred, J. F. J. Todd, A. D. Penman, F. Vedel and M. Vedel, "Resonant Excitation of Ions Stored in a Quadrupole Ion Trap. Part III. Introduction the the Field InterpolationSimulationMethod," *Int. J. Mass Spectrom. Ion Processes,* vol. 110, no. 3, p. 159–178, 1991.

[108] F. A. Londry, R. L. Alfred and R. E. March, "Computer Simulation of Single-Ion Trajectories in Paul-Type Ion Traps," *J. Am. Soc. Mass Spectrom.,* vol. 4, no. 9, p. 687–705, 1993.

[109] R. E. March, M. R. Weir, M. Tkaczyk, F. A. Londry, R. L. Alfred, A. M. Franklin and J. F. J. Todd, "Kinetic Energy Effects in an Ion Ensemble Subjected to Mass-Selective Isoation and Resonance Excitation: A Simulation Study," *Org. Mass Spectrom.,* vol. 28, no. 5, p. 499–509, 1993.

[110] R. L. Alfred, F. A. Londry and R. E. March, "Resonance Excitation of Ions Stored in a Quadrupole Ion Trap. Part IV. Theory of Quadrupolar Excitation," *Int. J. Mass Spectrom. Ion Processes,* vol. 125, no. 2–3, p. 171–185, 1993.

[111] M. Splendore, F. A. Londry, R. E. March, R. J. S. Morrison, P. Perrier and J. André, "A Simulation Study of Ion Kinetic Energies During Resonant Excitation in a Stretched Ion Trap," *Int. J. Mass Spectrom. Ion Processes,* vol. 156, no. 1–2, p. 11–29, 1996.

[112] R. E. March, M. Tkacyzk, F. A. Londry and R. L. Alfred, "Mass-Selective Isolation of Ions Stored in a Quadrupole Ion Trap. Part 2. A Simulation Study of Consecutive Isolation," *Int. J. Mass Spectrom. Ion Processes,* vol. 125, no. 1, p. 9–32, 1993.

[113] M. Splendore, M. Lausevic, Z. Lausevic and R. E. March, "Resonant Excitation and/or Ejection of Ions Subjected to DC and RF Fields in a Commercial Quadrupole Ion Trap," *Rapid Commun. Mass Spectrom.,* vol. 11, no. 2, p. 228–233, 1997.

[114] R. E. March, F. A. Londry, R. L. Alfred, A. M. Franklin and J. F. J. Todd, "Mass-Selective Isolation of Ions Stored in a Quadrupole Ion Trap. A Simulation Study," *Int. J. Mass Spectrom. Ion Processes,* vol. 112, no. 2–3, p. 247–271, 1992.

[115] D. A. Dahl, "SIMION for the Personal Computer in Reflection," *Int. J. Mass Spectrom.,* vol. 200, no. 1–3, p. 3–25, 2000.

[116] L. He and D. M. Lubman, "Simulation of External Ion Injection, Cooling and Extraction Processes with SIMION 6.0 for the Ion Trap/Reflectron Time-of-Flight Mass Spectrometer," *Rapid Commun. Mass Spectrom.,* vol. 11, no. 13, p. 1467–1477, 1997.

[117] K. Blaum, C. Geppert, P. Müller, W. Nörtershäuser, E. W. Otten, A. Schmitt, N. Trautmann, K. Wendt and B. A. Bushaw, "Properties and Performance of a Quadrupole Mass Filter used for Resonance Ionization Mass Spectrometry," *Int. J. Mass Spectrom.,* vol. 181, no. 1–3, p. 67–87, 1998.

[118] V. M. Doroshenko and R. J. Cotter, "Injection of Externally Generated Ions into an Increasing Trapping Field of a Quadrupole Ion Trap Mass Spectrometer," *J. Mass Spectrom.,* vol. 32, no. 6, p. 602–615, 1997.

[119] E. E. Gard, M. K. Green, H. Warren, E. J. O. Camara, F. He, S. G. Penn and C. B. Lebrilla, "A Dual Vacuum Chamber Fourier Transform Mass Spectrometer with Rapidly Interchangeable FAB, MALDI, and ESI sources: electrospray results," *Int. J. Mass Spectrom. Ion Processes,* vol. 157/158, p. 115–127, 1996.

[120] S. A. Schaffer, K. Tang, G. A. Anderson, D. C. Prior, H. R. Udseth and R. D. Smith, "A Novel Ion Funnel for Focusing Ions at Elevated Pressure Using Electrospray Ionization Mass Spectrometry," *Rapid Commun. Mass Spectrom.,* vol. 11, no. 16, p. 1813–1817, 1997.

[121] *SIMION 8.0,* Ringoes, NJ: Scientific Instrument Services, Inc.

[122] J. M. Higgs and D. E. Austin, "Simulations of Ion Motion in Toroidal Ion Traps," *Int. J. Mass Spectrom.,* vol. 363, p. 40–51, 2014.

[123] J. E. Fulford, D.-N. Hoa, R. J. Hughes, R. E. March, R. F. Bonner and G. J. Wong, "Radio-Frequency Mass Selective Excitation and Resonant Ejection of Ions in a Three-Dimensional Quadrupole Ion Trap," *J. Vac. Sci. Technol.,* vol. 17, no. 4, p. 829–835, 1980.

[124] M. Wang, H. E. Quist, B. J. Hansen, Y. Peng, Z. Zhang, A. R. Hawkins, A. L. Rockwood, D. E. Austin and M. L. Lee, "Performance of a Halo Ion Trap Mass Analyzer with Exit Slits for Axial Ejection," *J. Am. Soc. Mass Spectrom.,* vol. 22, no. 2, p. 369–378, 2011.

[125] A. Chaudhary, F. van Amerom, R. Short and S. Bhansali, "Fabrication and Testing of a Miniature Cylindrical Ion Trap Mass Spectrometer Constructed from Low Temperature Co-Fired Ceramics," *Int. J. Mass Spectrom.,* vol. 251, p. 32–39, 2006.

[126] M. Sudakov, "Effective Potential and the Ion Axial Beat Motion near the Boundary of the First Stable Region in a Nonlinear Ion Trap," *Int. J. Mass Spectrom.,* vol. 206, no. 1–2, p. 27–43, 2001.

[127] D. E. Austin, B. J. Hansen, Y. Peng and Z. Zhang, "Multipole Expansion in Quadrupolar Devices Comprised of Planar Electrode Arrays," *Int. J. Mass Spectrom.,* vol. 295, p. 153–158, 2010.

[128] Z. Zhang, H. Quist, Y. Peng, B. J. Hansen, J. Wang, A. R. Hawkins and D. E. Austin, "Effects of Higher-Order Multipoles on the Performance of a Two-Plate Quadrupole Ion Trap Mass Analyzer," *Int. J. Mass Spectrom.,* vol. 299, p. 151–157, 2011.

[129] L. Ding, M. Sudakov and S. Kumashiro, "A Simulation Study of the Digital Ion Trap Mass Spectrometer," *Int. J. Mass Spectrom.,* vol. 221, p. 117–138, 2002.

[130] A. V. Tolmachev, H. R. Udseth and R. D. Smith, "Modeling the Ion Density Distribution in Collisional Cooling RF Multipole Ion Guides," *Int. J. Mass Spectrom.,* vol. 222, p. 155–174, 2003.

[131] A. Makarov, E. Denisov, A. Kholomeev, W. Balschun, O. Lange, K. Strupat and S. Horning, "Performance Evaluation of a Hybrid Linear Ion Trap/Orbitrap Mass Spectrometer," *Anal. Chem.,* vol. 78, no. 7, p. 2113–2120, 2006.

[132] J. M. Higgs, B. V. Petersen, S. A. Lammert, K. F. Warnick and D. E. Austin, "Radiofrequency trapping of ions in a pure toroidal potential distribution," *Int. J. Mass Spectrom.,* vol. 395, p. 20–26, 2016.

[133] N. Yu, W. Nagourney and H. Dehmelt, "Demonstration of New Paul-Straubel Trap for Trapping Single Ions," *J. Appl. Phys.,* vol. 69, no. 6, p. 3779–3781, 1991.

[134] D. Gerlich, "lon-Neutral Collisions in a 22-Pole Trap at Very Low Energies," *Phys. Scr.,* vol. T59, p. 256–263, 1995.

[135] X. Zhou, C. Xiong, G. Xu, H. Liu, Y. Tang, Z. Zhu, R. Chen, H. Qiao, Y.-H. Tseng, W.-P. Peng, Z. Nie and Y. Chen, "Potential Distribution and Transmission Characteristics in a

Curved Quadrupole Ion Guide," *J. Am. Soc. Mass Spectrom.,* vol. 22, no. 2, p. 386–398, 2011.

[136] P. M. Morse and H. Feshbach, in *Methods of Theoretical Physics, Part I*, New York, McGraw-Hill, 1953, p. 666.

[137] P. M. Morse and H. Feshbach, in *Methods of Theoretical Physics, Part I*, New York, McGraw-Hill, 1953, p. 593–597.

[138] S. Lammert, E. Lee, R. Waite, J. Oliphant, D. Austin, J. Higgs, K. F. Warnick and D. Tolley, "Toroidal Multipole Expansion for the Design of Circular Ion Traps," in *62nd ASMS Conference on Mass Spectrometry and Allied Topics*, Baltimore, MD, 2014.

[139] V. Rajagopal, C. Stokes and A. Ferzoco, "A Linear Ion Trap with an Expanded Inscribed Diameter to Improve Optical Access for Fluorescence Spectroscopy," *J. Am. Soc. Mass Spectrom.,* 2017. https://doi.org/10.1007/s13361-017-1763-3.

[140] J. Nauta, A. Borodin, H. B. Ledwa, J. Stark, M. Schwarz, L. Schmöger, P. Micke, J. R. Crespo López-Urrutia and T. Pfeifer, "Towards Precision Measurements on Highly Charged Ions Using a High Harmonic Generation Frequency Comb," *Nucl. Instrum. Methods Phys. Res. B,* vol. 408, p. 285–288, 2017.

[141] W. M. Itano, J. C. Bergquist and D. J. Wineland, "Early Observations of Macroscopic Quantum Jumps in Single Atoms," *Int. J. Mass Spectrom.,* vol. 377, p. 403–409, 2015.

[142] T. R. Tan, J. P. Gaebler, Y. Lin, Y. Wan, R. Bowler, D. Leibfried and D. J. Wineland, "Multi-Element Logic Gates for Trapped-Ion Qubits," *Nature,* vol. 528, no. 7582, p. 380–383, 2015.

[143] Z. Peng, J. Bu and S. A. McLuckey, "The Generation of Dehydroalanine Residues in Protonated Polypeptides: Ion/Ion Reactions for Introducing Selective Cleavages," *J. Am. Soc. Mass Spectrom.,* vol. 28, no. 9, p. 1765–1774, 2017.

[144] A. N. Kotana and A. K. Mohanty, "Determination of Multipole Coefficients in Toroidal Ion Trap Mass Analysers," *Int. J. Mass Spectrom.,* vol. 408, p. 62–76, 2016.

[145] A. N. Kotana and A. K. Mohanty, "Computation of Mathieu Stability Plot for an Arbitrary Toroidal Ion Trap Mass Analyser," *Int. J. Mass Spectrom.,* vol. 414, p. 13–22, 2017.

[146] X. Zhou, C. Xiong, S. Zhang, N. Zhang and Z. Nie, "Study of Nonlinear Resonance Effect in Paul Trap," *J. Am. Soc. Mass Spectrom.,* vol. 24, no. 5, p. 794–800, 2013.

[147] D. J. Douglas, "Linear Quadrupoles in Mass Spectrometry," *Mass Spectrom. Rev.,* vol. 28, no. 6, p. 937–960, 2009.

[148] D. E. Austin and N. R. Taylor, "Toroidal Ion Trap Mass Analyzer with Cylindrical Electrodes". US Patent 8,642,955 B2, 4 Feb. 2014.

[149] M. E. Monge, G. A. Harris, P. Dwivedi and F. M. Fernández, "Mass Spectrometry: Recent Advances in Direct Open Air Surface Sampling/Ionization," *Chem. Rev.,* vol. 113, no. 4, p. 2269–2308, 2013.

APPENDIX

Because of the many simulations that I have done for this research, I've included the computer programing involved in running the simulations and the Matlab scripts I used to process the data.

A.1 SIMION 8.0 .lua User Programs

When running ion traps in SIMION 8.0, I used user programs to control the voltages and data recording. The user programs were written in .lua. Comments in .lua programming are notated with "--" in front. The main user program shares the same with the simulation program. It refers to a selected mode (i.e. group.lua) that imports the program (i.e. util.lua) that controls the voltages and other settings. Other modes I used had additions to the util.lua file for recording data and running several ions sequentially.

A.1.1 Main User Program

```
-- trap.lua - Loads one of the ion trap demos.
-- D.Manura-2006-08.
-- (c) 2006 Scientific Instrument Services, Inc. (Licenced under SIMION 8.0)
--================================================================
simion.workbench_program()
-- <mode> is a global variable that selects which simulation to load
-- ("inject", "group", or "tickle").  You may change the default
-- mode here or override the default by entering <mode="tickle">
-- (without brackets) in the SIMION command-bar.
-- You must reload the workbench IOB after making this change.
local cmode = mode or "group"  -- default
-- Check mode selection.
assert(cmode == "inject" or cmode == "group" or cmode == "tickle",
       "invalid simulation mode <" .. tostring(cmode) ..
        [[>. mode should be "inject", "group", or "tickle".]])
      -- cmodes can be added to this which refer to other .lua files
-- Load program defining mode.
local filename = cmode .. ".lua"
simion.import(filename)
```

```
print(cmode .. " mode loaded.")
```

A.1.2 group.lua

```
-- group.lua - ion trap demo program for demonstrating ion grouping inside
trap.
-- D.Manura-2006-08 - based on PRG code from SIMION 7.0 - David A. Dahl 1995
-- (c) 2006 Scientific Instrument Services, Inc. (Licensed under SIMION 8.0)
--============================================================
simion.import("util.lua") -- load default ion trap behavior
-- Incorporate default ion trap behavior.
trap_install_segments()
-- Incorporate Stoke's law viscous effects on ion motion.
segment.accel_adjust = stokes_damping
```

A.1.3 util.lua

```
-- util.lua - Functionality shared by the ion trap demo programs
-- Also with hard sphere collisions (see collisions_hs1.lua)
-- After defining the variables, the segments of the program are:
      -- trap_initialize: Starting conditions
      -- trap_fast_adjust: Voltage control with respect to time
      -- trap_tstep_adjust: Controls the time-step size
      -- trap_other_actions: Controls collisions, prepares for next time-step
      -- trap_terminate: Activates when the ion's flight has ended
--====================================================================
---- adjustable during flight
-- ion trap voltage control
adjustable _RF_amplitude      = 500      -- RF amplitude
adjustable _DC_voltage        = 0.0      -- DC voltage
-- collisions
adjustable _mean_free_path_mm = -1       -- Mean free path (MFP) (mm) between
collisions
      -- if value of -1, mean free path is calculated by pressure and other
variables below
adjustable _gas_mass_amu = 4.0           -- Mass of background gas particle
(amu)
adjustable _temperature_k = 273.0        -- Background gas temperature (K)
adjustable _pressure_pa = 0              -- Background gas pressure (Pa)
adjustable _sigma_m2 = 2.27E-18          -- Collision-cross section (m^2)
adjustable _vx_bar_gas_mmusec = 0        -- Mean background gas velocity
(mm/usec)
adjustable _vy_bar_gas_mmusec = 0        --  in x,y,z directions
adjustable _vz_bar_gas_mmusec = 0        --
adjustable _steps_per_MFP = 20.0         -- Mean number of time steps per MFP

---- adjustable at beginning of flight
-- voltage control
adjustable phase_angle_deg       = 0.0   -- entry phase angle of ion (deg)
adjustable freqency_hz           = 9.9E5 -- RF frequency of quad in (hz)
-- display
```

```
adjustable pe_update_each_usec   = 0.05  -- PE display update time step
(usec)
-- collisions
adjustable _mark_collisions = 1          -- Collision marker flag
adjustable _trace_level = 0              -- How much trace data (average KE)
to output
adjustable _trace_skip = 100             -- If _trace_level is 2, this is the
number
                                         --  of collisions before each trace

---- Internal variables
-- Statistics
local ke_averages = {}                  --current running average of KE for
each particle
local last_collision_times = {}         --last collision time for each
particle
local last_ion_number = -1              --last known ion number (-1 =
undefined)
local last_speed_ion = -1               --last known ion speed (-1 =
undefined)
local effective_mean_free_path_mm = -1 --currently used mean-free path (-1 =
undefined)
local trace_count = 0                   --count relative to _trace_skip
local max_timestep                      --maximum time step (usec) that
fast_adjust should permit
-- Define constants
local k = 1.3806505e-23       -- Boltzmann constant (J/K)
local R = 8.3145              -- Ideal gas constant (J/(mol*K))
local kg_amu = 1.6605402e-27  -- (kg/amu) conversion factor
local pi = math.pi            -- PI constant
local eV_J = 6.2415095e+18    -- (eV/J) conversion factor
-- Error function (erf)
function erf(z)               --erf(z) = (2/sqrt(pi)) * integral[0..z] exp(-
t^2) dt
    local z2 = abs(z)
    local t = 1 / (1 + 0.32759109962 * z2)
    local res = (    - 1.061405429 ) * t
    res = (res + 1.453152027 ) * t
    res = (res - 1.421413741 ) * t
    res = (res + 0.2844966736) * t
    res =((res - 0.254829592 ) * t) * exp(-z2*z2)
    res = res + 1
    if z < 0 then res = -res end
    return res
end
-- Return a normalized Gaussian random variable (-inf, +inf)
function gaussian_random()
    -- Using the Box-Muller algorithm.
    local s = 1
    local v1, v2
    while s >= 1 do
        v1 = 2*rand() - 1
        v2 = 2*rand() - 1
        s = v1*v1 + v2*v2
    end
    local rand1 = v1*sqrt(-2*ln(s) / s)  -- (assume divide by zero
improbable?)
```

```
    return rand1
end

-- Default SIMION initialize segment for ion trap example.
-- This segment is called on every particle creation.
function trap_initialize()
    -- Enable rerun mode (used only for side-effect of disabling trajectory
file saving).
    sim_rerun_flym = 1
end

-- Default SIMION fast_adjust segment for ion trap example.
-- This segment is called to modify electrode voltages.
local is_first  = true   -- first call flag
local omega     = 1.0    -- frequency (rad/usec)
local theta     = 0.0    -- phase offset (rad)
function trap_fast_adjust()
    ---- Generate trap RF voltages with fast adjust.
    -- For efficiency, we calculate some variables only once.
    if is_first then
        is_first = false
        theta = rad(phase_angle_deg)              -- phase angle (rad)
        omega = freqency_hz * 2 * 3.14159 * 1E-6  -- frequency (rad/usec)
    end
    -- Set electrode voltages.
    adj_elect01 = _DC_voltage
    adj_elect02 = _DC_voltage + _RF_amplitude * sin(theta +
ion_time_of_flight * omega)
        --U+V*sin(theta+t*omega)
end

-- Default SIMION time_step adjust segment for ion trap example.
-- This segment is called to override time-step size.
function trap_tstep_adjust()
    -- Keep time step <= 0.1 usec.
    if ion_time_step > 0.1 then ion_time_step = 0.1 end
end

-- Default SIMION other_actions segment for ion trap example.
-- This segment is called on every time-step.
function trap_other_actions()
    if _pressure_pa == 0 then  -- collisions disabled
        return
    end
    local vx = ion_vx_mm - _vx_bar_gas_mmusec
    local vy = ion_vy_mm - _vy_bar_gas_mmusec
    local vz = ion_vz_mm - _vz_bar_gas_mmusec
    local speed_ion = sqrt(vx^2 + vy^2 + vz^2)
    if speed_ion < 1E-7 then
         speed_ion = 1E-7  -- prevent divide by zero and such effects later
on
    end
    if _mean_free_path_mm > 0 then -- explicitly specified
        effective_mean_free_path_mm = _mean_free_path_mm
    else
        if last_ion_number ~= ion_number or
                abs(speed_ion / last_speed_ion - 1) > 0.05  -- changed
```

```
        then
            local c_bar_gas = sqrt(8*k*_temperature_k/pi/(_gas_mass_amu *
kg_amu)) / 1000
            local c_star_gas = sqrt(2*k*_temperature_k/(_gas_mass_amu *
kg_amu)) / 1000
            local s = speed_ion / c_star_gas
            local c_bar_rel = c_bar_gas * (
                (s + 1/(2*s)) * 0.5 * sqrt(pi) * erf(s) + 0.5 * exp(-s*s))
            effective_mean_free_path_mm = 1000 * k * _temperature_k *
                (speed_ion / c_bar_rel) / (_pressure_pa * _sigma_m2)
            last_speed_ion = speed_ion
            last_ion_number = ion_number
        end
    end
    max_timestep = effective_mean_free_path_mm / speed_ion / _steps_per_MFP
    local collision_prob = 1 -
        exp(- speed_ion * ion_time_step / effective_mean_free_path_mm)
    if rand() > collision_prob then
        return -- no collision
    end
    ----- Handle collision.
    local vr_stdev_gas =
        sqrt(k * _temperature_k / (_gas_mass_amu * kg_amu)) / 1000
    local vx_gas, vy_gas, vz_gas -- computed velocities
    local scale = speed_ion + vr_stdev_gas * 1.732 * 3  --sqrt(3)=~1.732
    repeat
        vx_gas = gaussian_random() * vr_stdev_gas
        vy_gas = gaussian_random() * vr_stdev_gas
        vz_gas = gaussian_random() * vr_stdev_gas
        local len = sqrt((vx_gas - vx)^2 + (vy_gas - vy)^2 + (vz_gas - vz)^2)
    until rand() < len / scale
    vx = vx - vx_gas
    vy = vy - vy_gas
    vz = vz - vz_gas
    local impact_offset = sqrt(0.999999999 * rand())
    local impact_angle = asin(impact_offset)
    local impact_theta = 2*pi*rand()
    local speed_ion_r, az_ion_r, el_ion_r = rect3d_to_polar3d(vx, vy, vz)
    local vr_ion = speed_ion_r * cos(impact_angle)    -- radial velocity
    local vt_ion = speed_ion_r * sin(impact_angle)    -- normal velocity
    local vr_ion2 = (vr_ion * (ion_mass - _gas_mass_amu))
                  / (ion_mass + _gas_mass_amu)
    vx, vy, vz = elevation_rotate(90 - deg(impact_angle), vr_ion2, vt_ion, 0)
    vx, vy, vz = azimuth_rotate(deg(impact_theta), vx, vy, vz)
    vx, vy, vz = elevation_rotate(-90 + el_ion_r, vx, vy, vz)
    vx, vy, vz = azimuth_rotate(az_ion_r, vx, vy, vz)
    vx = vx + vx_gas + _vx_bar_gas_mmusec
    vy = vy + vy_gas + _vy_bar_gas_mmusec
    vz = vz + vz_gas + _vz_bar_gas_mmusec
    ion_vx_mm, ion_vy_mm, ion_vz_mm = vx, vy, vz
    if _trace_level >= 1 then
      --Compute new ion speed and KE
        local speed_ion2 = sqrt(ion_vx_mm^2 + ion_vy_mm^2 + ion_vz_mm^2)
        local ke2_ion = speed_to_ke(speed_ion2, ion_mass)
        local dt = ion_time_of_flight - (last_collision_times[ion_number] or
0)
        reset_time = ion_time_of_flight * 0.5
```

```
        local w = 1 - (dt / reset_time)  -- ~= exp(-dt / reset_time)
        ke_averages[ion_number] = w * (ke_averages[ion_number] or ke2_ion)
                                  + (1-w) * ke2_ion
        if _trace_level >= 2 then -- more detail
            local T_ion = ke_averages[ion_number] / eV_J / (1.5 * k)
            if trace_count % _trace_skip == 0 then
                print(string.format(
                    "n=,%d,TOF=,%0.3g,ion KE (eV)=,%0.3e,ion mean KE
(eV)=," ..
                    "%0.3e,ion mean temp (K)=,%0.3e",
                    ion_number, ion_time_of_flight, ke2_ion,
                    ke_averages[ion_number], T_ion))
            end
            trace_count = (trace_count + 1) % _trace_skip
        end
        last_collision_times[ion_number] = ion_time_of_flight
    end

    if _mark_collisions ~= 0 then
        mark() -- draw dot at collision point
    end
    local next_pe_update = 0.0
    if ion_time_of_flight >= next_pe_update then
        -- Request a PE surface display update.
        sim_update_pe_surface = 1
        -- Schedule next PE display update time (usec).
        next_pe_update = ion_time_of_flight + pe_update_each_usec
    end
end

-- Default SIMION terminate segment for ion trap example.
-- This segment is called on each particle termination.
function trap_terminate()
    if _trace_level >= 1 then
        -- ion temperature
        local T_ion = ke_averages[ion_number] / eV_J / (1.5 * k)
        print(string.format(
            "n=,%d,TOF=,%0.3g,ion mean KE (eV)=,%0.3e,ion mean temp
(K)=,%0.3e",
            ion_number, ion_time_of_flight, ke_averages[ion_number], T_ion))
    end
    -- Disable rerun mode from initialize segment (we don't really want to
rerun)
    sim_rerun_flym = 0
end

-- Install default SIMION segments for ion trap example.
-- This provides a quick method for programs that use this
-- file to install the default ion trap functionality.
function trap_install_segments()
    segment.initialize    = trap_initialize
    segment.fast_adjust   = trap_fast_adjust
    segment.tstep_adjust  = trap_tstep_adjust
    segment.other_actions = trap_other_actions
    segment.terminate     = trap_terminate
end
```

A.1.4 Running Ions Sequentially with Different RF Amplitude and Same DC Offset

This program removed the variables for considering collisions with the background gas. Several variables were added so that the RF amplitude could be different for each ion simulated.

Variable definitions added:

```
-- ion trap voltage control
adjustable _RF_min            = 152       -- RF amplitude
adjustable _RF_max            = 1000
adjustable _RF_amplitude      = _RF_min
adjustable _DC_voltage  = 0
adjustable request_rerun      = 1         -- Flag: request rerun. 0 for no. 1
for yes.
adjustable count        = 0
adjustable ion_ending         = 0         -- for ion splat reference
adjustable delta_V            = 1         -- change in voltage for each
flight
adjustable maxTOF       = 8e6
```

Changes to trap_initialize to write data and increase RF amplitude:

```
function trap_initialize()
      -- change voltages
      if _RF_amplitude >= _RF_max then
            request_rerun = 0
      end
      outfile = 'file_name'
      if count == 0 then
            _RF_amplitude = _RF_min
            fout=io.open(outfile,'a')
            fout:write('RF, TOF, X, Y, ending')
            fout:write('\n')
            fout:close()
      else
            _RF_amplitude = _RF_amplitude + delta_V
      end
      count = count + 1
      -- Enable/Disable rerun mode
      sim_rerun_flym = request_rerun
end
```

Added to trap_other_actions() to consider an ion to be stably trapped or hit one electrode:

```
-- ion_splat = 0 when ion is in flight. Any other value when flight is
terminated
if ion_time_of_flight >= maxTOF then
      ion_splat = 2
end
if ion_splat ~= 0 or ion_splat ~= 2 then  -- Recording which electrode it hit
      if ion_py_mm > 8 then
            ion_ending = 1
      elseif ion_px_mm < 8 then
```

```
            ion_ending = 2
      elseif ion_px_mm > 12 then
            ion_ending = 3
      else
            ion_ending = 4
      end
end
```

Additions to trap_terminate() to record data:

```
function trap_terminate()
      fout=io.open(outfile,'a')
      fout:write(_RF_amplitude)
      fout:write(', ')
      fout:write(ion_time_of_flight)
      fout:write(', ')
      if ion_ending == 0 then
            fout:write('NA, NA, stable')
      elseif ion_ending == 1 then
            fout:write(ion_px_mm..', '..ion_py_mm..', ')
            fout:write('radial 1')
      elseif ion_ending == 2 then
            fout:write(ion_px_mm..', '..ion_py_mm..', ')
            fout:write('axial 1')
      elseif ion_ending == 3 then
            fout:write(ion_px_mm..', '..ion_py_mm..', ')
            fout:write('axial 2')
      elseif ion_ending == 4 then
            fout:write(ion_px_mm..', '..ion_py_mm..', ')
            fout:write('radial 2')
      end
      fout:write('\n')
      fout:close()
end
```

A.1.5 Running Ions Sequentially to Find the Boundaries of the Stability Diagram

This program was set to find the upper and lower boundaries of the stability diagram. The program used three stages. During the initial stage, the RF amplitude would be incrementally increased for each ion ran at a given DC offset until the first stable point was found. The next stage would find the boundaries by identifying the maximum DC offset value where the ion was still trapped for each increasing RF amplitude value. When no more stable points are seen at higher RF amplitude values, the program switches to the last stage. During this last stage, the program would identify the minimum DC offset value where the ion is still trapped for each

decreasing RF amplitude value. This continues until the program reaches the same RF amplitude and DC offset as the first stable point identified. For determining the boundaries of the stability diagram when considering collisions, this method was also used with considering the boundary to be if at least one of a thousand ions was stably trapped because of the randomness from the collisional model.

The initial parameters for no collisions were:

```
--Adjusting Parameters
adjustable run_count= 0             --Rerun counter
adjustable min_TOF = 2000
adjustable max_TOF = 2010      -- Maximum TOF to wait for (microseconds)
adjustable _RF_amplitude = 67              --RF Voltage being tested
adjustable _DC_voltage = 0          --DC voltage being tested
adjustable request_rerun = 1        -- Flag: request rerun. 0 for no. 1 for
yes.
adjustable stage = 0
adjustable m = 0
adjustable m_limit = 9
adjustable n = 0
adjustable n_limit = 9
adjustable first_RF = 0
adjustable first_DC = 0
adjustable latest_RF = 0
adjustable latest_DC = 0
```

Parameters for when collisions are present:

```
--Adjusting Parameters
adjustable run_count= 0             --Rerun counter
adjustable min_TOF = 100
adjustable max_TOF = 110       -- Maximum TOF to wait for (microseconds)
adjustable _RF_amplitude = 0        --RF Voltage being tested
adjustable _DC_voltage = 0          --DC voltage being tested
-- for adjusting voltages
adjustable request_rerun = 1        -- Flag: request rerun. 0 for no. 1 for
yes.
adjustable stage = 0
adjustable m = 0
adjustable m_limit = 9
adjustable n = 0
adjustable n_limit = 9
adjustable first_RF = 0
adjustable first_DC = 0
adjustable latest_RF = 0
adjustable latest_DC = 0
adjustable running = 0
adjustable number = 0
adjustable maxn = 1000
```

I also used a function for the data recording:

```
function record()
      fout = io.open(outfile, "a")
      fout:write(run_count..', '..stage..', '.._RF_amplitude..',
'.._DC_voltage..'\n')
      fout:close()
end
```

For the voltage control and data recording of the boundaries without considering collisions, I added to the function trap_terminate() :

```
run_count = run_count + 1                          -- No. of flights
if stage == 0 then                                 -- Find first point
      if ion_time_of_flight > min_TOF then
            First_RF = _RF_amplitude
            First_DC = _DC_voltage
            latest_RF = _RF_amplitude
            latest_DC = _DC_voltage
            record()
            _DC_voltage = _DC_voltage + 1
            stage = 1
      end
      _RF_amplitude = _RF_amplitude + 1
elseif stage == 1 then                     -- Find upper boundary points
      if ion_time_of_flight > min_TOF then
            if m > 0 then
                  record()
                  latest_RF = _RF_amplitude
                  latest_DC = _DC_voltage
                  _RF_amplitude = _RF_amplitude + 1
                  m = 0
                  n = 0
            else
                  if n == 0 then
                        record()
                        latest_RF = _RF_amplitude
                        latest_DC = _DC_voltage
                  end
                  n = n + 1
                  if n > n_limit then
                        _RF_amplitude = latest_RF - 1
                        _DC_voltage = latest_DC
                        m = 0
                        n = 0
                        stage = 2
                  end
            end
            _DC_voltage = _DC_voltage + 1
      else
            _DC_voltage = _DC_voltage - 1
            m = m + 1
            if m > m_limit then
                  _RF_amplitude = latest_RF
```

```
                  _DC_voltage = latest_DC
                  m = 0
                  n = 0
                  stage = 2
            end
      end
elseif stage == 2 then                          -- Find lower boundary points
      if ion_time_of_flight > min_TOF then
            if m > 0 then
                  record()
                  latest_RF = _RF_amplitude
                  latest_DC = _DC_voltage
                  _RF_amplitude = _RF_amplitude - 1
                  m = 0
                  n = 0
            else
                  if n == 0 then
                        record()
                        latest_RF = _RF_amplitude
                        latest_DC = _DC_voltage
                  end
                  n = n + 1
                  if n > n_limit then
                        _RF_amplitude = latest_RF + 1
                        _DC_voltage = latest_DC
                        m = 0
                        n = 0
                        stage = 1
                  end
            end
            _DC_voltage = _DC_voltage - 1
      else
            _DC_voltage = _DC_voltage + 1
            m = m + 1
            if m > m_limit then
                  m = 0
                  _RF_amplitude = latest_RF
                  _DC_voltage = latest_DC
                  stage = 1
            end
      end
end
if stage ~= 0 then                  -- Terminate when back to first
      if _RF_amplitude == First_RF and _DC_voltage == First_DC then
            request_rerun=0
      end
end
fout:close()
```

For the voltage control and data recording of the boundaries while considering collisions, I added to the function trap_terminate() :

```
if ion_time_of_flight > min_TOF then
      if stage == 0 then
            First_RF = _RF_amplitude
```

```
        First_DC = _DC_voltage
        latest_RF = _RF_amplitude
        latest_DC = _DC_voltage
        record()
        _DC_voltage = _DC_voltage + 1
        _RF_amplitude = _RF_amplitude + 1
        stage = 1
elseif stage == 1 then
        if m > 0 then
                record()
                latest_RF = _RF_amplitude
                latest_DC = _DC_voltage
                _RF_amplitude = _RF_amplitude + 1
                m = 0
                n = 0
        else
                if n == 0 then
                        record()
                        latest_RF = _RF_amplitude
                        latest_DC = _DC_voltage
                end
                n = n + 1
                if n > n_limit then
                        _RF_amplitude = latest_RF - 1
                        _DC_voltage = latest_DC
                        m = 0
                        n = 0
                        stage = 2
                end
        end
        _DC_voltage = _DC_voltage + 1
elseif stage == 2 then
        if m > 0 then
                record()
                latest_RF = _RF_amplitude
                latest_DC = _DC_voltage
                _RF_amplitude = _RF_amplitude - 1
                m = 0
                n = 0
        else
                if n == 0 then
                        record()
                        latest_RF = _RF_amplitude
                        latest_DC = _DC_voltage
                end
                n = n + 1
                if n > n_limit then
                        _RF_amplitude = latest_RF + 1
                        _DC_voltage = latest_DC
                        m = 0
                        n = 0
                        stage = 1
                end
        end
        _DC_voltage = _DC_voltage - 1
end
number = 0
```

```
elseif number >= maxn then
      run_count = run_count + 1
      if stage == 0 then
            _RF_amplitude = _RF_amplitude + 1
      elseif stage == 1 then
            _DC_voltage = _DC_voltage - 1
            m = m + 1
            if m > m_limit then
                  _RF_amplitude = latest_RF
                  _DC_voltage = latest_DC
                  m = 0
                  n = 0
                  stage = 2
            end
      elseif stage == 2 then
            _DC_voltage = _DC_voltage + 1
            m = m + 1
            if m > m_limit then
                  m = 0
                  _RF_amplitude = latest_RF
                  _DC_voltage = latest_DC
                  stage = 1
            end
      end
      number = 0
end
if stage ~= 0 then                    -- Terminate when back to first
      if _RF_amplitude == First_RF and _DC_voltage == First_DC then
            request_rerun=0
      end
end
```

A.1.6 Running Ions Sequentially at a range of RF Amplitude and DC Offset Values

This program was similar to the one described in section A.1.4 with the difference in that both the RF amplitude and DC offset are different for each ion.

The parameters used were:

```
-- ion trap voltage control
adjustable _RF_min            = 0         -- RF amplitude
adjustable _RF_max            = 1600
adjustable _RF_amplitude      = _RF_min
adjustable _DC_min            = -200            -- DC voltage
adjustable _DC_max            = 220
adjustable _DC_voltage        = _DC_min
adjustable request_rerun      = 1         -- Flag: request rerun. 0 for no. 1
for yes.
adjustable count        = 0
adjustable max_TOF            = 100
adjustable ion_ending         = 0         -- for ion splat reference
```

```
adjustable delta_V_RF         = .5        -- change in voltage for each
flight
adjustable delta_V_DC         = .125
```

Writing the header for the data and controlling the RF amplitude and DC offset were added to the function trap_initialize():

```
function trap_initialize()
      -- change voltages
      if _RF_amplitude > _RF_max then
            request_rerun = 0
      end
      outfile = 'MassToCharge'..ion_mass..'to'..ion_charge..'instability.csv'
      fout=io.open(outfile,'a')
      if count == 0 then
            _RF_amplitude = _RF_min
            _DC_voltage = _DC_min
            fout:write('count, RF, DC, TOF, X, Y, ending')
            fout:write('\n')
            fout:close()
            fout=io.open(outfile,'a')
      else
            if _DC_voltage > _DC_max then
                  _DC_voltage = _DC_min
                  _RF_amplitude = _RF_amplitude + delta_V_RF
            else
                  _DC_voltage = _DC_voltage + delta_V_DC
            end
      end
      count = count + 1
      -- Enable/Disable rerun mode
      sim_rerun_flym = request_rerun
end
```

Determining if the ion hit one of the electrodes or if it was stably trapped was added to the function trap_other_actions():

```
if ion_splat ~= 0 or ion_splat ~= 2 then
      if ion_py_mm > 8 then
            ion_ending = 1
      elseif ion_px_mm < 8 then
            ion_ending = 2
      elseif ion_px_mm > 12 then
            ion_ending = 3
      else
            ion_ending = 4
      end
end
if ion_time_of_flight > max_TOF then
      ion_ending = 0
      ion_splat = 2           -- After Max TOF period we will say the ion is
dead and move on
end
```

The data recording was in the trap_terminate() function:

```
function trap_terminate()
      fout:write(count)
      fout:write(', ')
      fout:write(_RF_amplitude)
      fout:write(', ')
      fout:write(_DC_voltage)
      fout:write(', ')
      fout:write(ion_time_of_flight)
      fout:write(', ')
      if ion_ending == 0 then
            fout:write('NA, NA, stable')
      elseif ion_ending == 1 then
            fout:write(ion_px_mm..', '..ion_py_mm..', ')
            fout:write('radial 1')
      elseif ion_ending == 2 then
            fout:write(ion_px_mm..', '..ion_py_mm..', ')
            fout:write('axial 1')
      elseif ion_ending == 3 then
            fout:write(ion_px_mm..', '..ion_py_mm..', ')
            fout:write('axial 2')
      elseif ion_ending == 4 then
            fout:write(ion_px_mm..', '..ion_py_mm..', ')
            fout:write('radial 2')
      end
      fout:write('\n')
      fout:close()
end
```

A.2 Matlab Scripts for Data Processing

I used Matlab to calculate multipole contributions and produce frequency spectra. Scripts in Matlab can be used to repeat calculations for several data sets. Comments in Matlab scripts are notated with "%" in front.

A.2.1 Calculating Multipole Contributions for Conventional Traps

The multipole contributions for conventional traps can be determined by taking the potential distribution across the trapping center and performing a polynomial fit. The field can also be displayed by taking the derivative of the potential distribution, and the multipoles can be shown by subtracting the linear contribution to the field. The data was obtained while flying a neutral particle across the trapping region in both the radial and axial directions. This script was

designed to read in the position and potential at each point, eliminate duplicates, interpolate the data points to ensure that the positions are evenly spaced, perform a polynomial fit to the 25th order, take the derivative of the potential distribution, determining the linear field contribution, and subtracting the linear field from the overall field.

```
clear all; close all;
% Input Data
Y=xlsread('filename','column');
PY=xlsread('filename','column');
X=xlsread('filename','column');
PX=xlsread('filename','column');
ro=5.91; zo=5.81; %Dimensions for cylindrical toroidal ion trap
[pky,locy]=findpeaks(-PY);
pky=pky(2); locy=locy(2);
[pkx,locx]=findpeaks(PX);
Yo=Y(locy); Xo=X(locx); sy=PY(locy); sx=PX(locx);

% Eliminate Duplicates
YI(1)=Y(1); PYI(1)=PY(1); m=1;
for n=2:length(Y)
    if Y(n)~=Y(n-1)
        m=m+1;
        YI(m)=Y(n);
        PYI(m)=PY(n);
    end
end
XI(1)=X(1); PXI(1)=PX(1); m=1;
for n=2:length(X)
    if X(n)~=X(n-1)
        m=m+1;
        XI(m)=X(n);
        PXI(m)=PX(n);
    end
end

% Interpolate Data
dy=(max(YI)-min(YI))/length(YI);
y=min(YI):dy:max(YI)-dy;
py=interp1(YI,PYI,y,'cubic');
dx=(max(XI)-min(XI))/length(XI);
x=min(XI):dx:max(XI)-dx;
px=interp1(XI,PXI,x,'cubic');

% First Derivative
py1=diff(py);
px1=diff(px);

% Normalization
r=(y-Yo)/ro;
pr=(py-sy)/max(py-sy);
[pkr,locr]=findpeaks(-pr);
pkr=pkr(2); locr=locr(2);
```

```
r1=r(1:end-1);

z=(x-Xo)/zo;
pz=px/sx;
[pkz,locz]=findpeaks(pz);
z1=z(1:end-1);

p=r1; q=z1;

% Find Linear Region of Field
f=r1;g=py1;
sum1=0; sum2=0; sum3=0; sum4=0; sum5=0;
for n=1:length(f)
    sum1=sum1+(f(n)*g(n));
    sum2=sum2+f(n);
    sum3=sum3+g(n);
    sum4=sum4+(f(n))^2;
    sum5=sum5+(g(n))^2;
end
Ry=(length(f)*sum1-sum2*sum3)/...
    ((length(f)*sum4-sum2^2)^(1/2)*(length(f)*sum5-sum3^2)^(1/2));
if length(r1)>=2*locr
    m=locr;
else
    m=length(r1)-locr;
end
while Ry^2<0.99999      %Increase number to decrease range used for linear
extrapolation
    m=m-1;
    f=r1(locr-m:locr+m);
    g=py1(locr-m:locr+m);
    sum1=0; sum2=0; sum3=0; sum4=0; sum5=0;
    for n=1:length(f)
        sum1=sum1+(f(n)*g(n));
        sum2=sum2+f(n);
        sum3=sum3+g(n);
        sum4=sum4+(f(n))^2;
        sum5=sum5+(g(n))^2;
    end
    Ry=(length(f)*sum1-sum2*sum3)/...
        ((length(f)*sum4-sum2^2)^(1/2)*(length(f)*sum5-sum3^2)^(1/2));
end
YR=polyfit(f,g,1);
yr=polyval(YR,r1);
pr1=(py1-YR(2))/YR(1);

h=z1;j=px1;
sum1=0; sum2=0; sum3=0; sum4=0; sum5=0;
for n=1:length(h)
    sum1=sum1+(h(n)*j(n));
    sum2=sum2+h(n);
    sum3=sum3+j(n);
    sum4=sum4+(h(n))^2;
    sum5=sum5+(j(n))^2;
end
Rx=(length(f)*sum1-sum2*sum3)/...
    ((length(f)*sum4-sum2^2)^(1/2)*(length(f)*sum5-sum3^2)^(1/2));
```

```
if length(z1)>=2*locz
    m=locz;
else
    m=length(z1)-locz;
end
while Rx^2<0.999999           %Increase number to decrease range used for
linear extrapolation
    m=m-1;
    h=z1(locz-m:locz+m);
    j=px1(locz-m:locz+m);
    sum1=0; sum2=0; sum3=0; sum4=0; sum5=0;
    for n=1:length(h)
        sum1=sum1+(h(n)*j(n));
        sum2=sum2+h(n);
        sum3=sum3+j(n);
        sum4=sum4+(h(n))^2;
        sum5=sum5+(j(n))^2;
    end
    Rx=(length(h)*sum1-sum2*sum3)/...
        ((length(h)*sum4-sum2^2)^(1/2)*(length(h)*sum5-sum3^2)^(1/2));
end
XZ=polyfit(h,j,1);
xy=polyval(XZ,z1);
pz1=(px1-XZ(2))/XZ(1);
clear sum1 sum2 sum3 sum4 sum5

% Subtract Linear
pLr=pr1-p;
pLz=pz1-q;

% Polynomial Fit
m=0; rs=0; prs=0;
for n=1:length(r)
    if -.99<=r(n)
        m=m+1;
        rs(m)=r(n);
        prs(m)=pr(n);
    end
end
cr=polyfit(rs,prs,25);
crq=cr/cr(24);
Cr=polyval(cr,rs);
clear m n

cz=polyfit(z,pz,25);
czq=cz/cz(24);
Cz=polyval(cz,z);

% Plots
a=[-2 2]; b=[0 0]; %For the x=0 and y=0 axes
figure
subplot(3,2,1)
plot(b,a,'k-',r,pr,'b-',rs,Cr,'r-')
axis([-1.5 1.5 0 1])
subplot(3,2,2)
plot(b,a,'k-',z,pz,'b-',z,Cz,'r-')
axis([-1.2 1.2 0 1])
```

```
subplot(3,2,3)
plot(a,b,'k-',b,a,'k-',r1,pr1,'b-',r1,p,'r-')
axis([-1.2 1.2 -1 1])
subplot(3,2,4)
plot(a,b,'k-',b,a,'k-',z1,pz1,'b-',z1,q,'r-')
axis([-1 1 -1.5 1.5])
subplot(3,2,5)
plot(a,b,'k-',b,a,'k-',r1,pLr,'b-')
axis([-1.2 1.2 -0.1 0.1])
subplot(3,2,6)
plot(a,b,'k-',b,a,'k-',z1,pLz,'b-')
axis([-1 1 -0.5 0.5])
clear a b

% The End
display('Finished')
```

A.2.2 Frequency Spectra of Ion Motion

The frequency spectra for the ion motion can be calculated by using a Fourier transform function in Matlab. The data collected included the time and the ion's position. This script was designed to read in the time and position of the ion, eliminate duplicates, interpolate the data points to ensure that the positions are evenly spaced, center the average at zero, perform the Fourier transform, and identify frequencies of the ion motion in Hz.

```
clear all;close all;
%reading in values from excel
data =
xlsread('U:\Documents\Research\SIMION\Harmonics\NonTruncated\IonMotionAtVolta
ges\RF750DC-60.xlsx','a12:c1048576');
tof = data(:,1);
x = data(:,2);
y = data(:,3);
OMEGA=2e6;
t=tof*1E-6;
% eliminate the duplicates
ti(1)=t(1);xi(1)=x(1);
yi(1)=y(1);
m=1;
N=length(t);
for n=2:N
    if t(n)~=t(n-1)
        m=m+1;
        ti(m)=t(n);
        xi(m)=x(n);
        yi(m)=y(n);
    end
end
```

```
% Interpolate data
tstart=min(ti);
tfinal=max(ti);
N=length(ti);
dt=(tfinal-tstart)/N;
T=tstart:dt:tfinal-dt;
X=interp1(ti,xi,T,'cubic');
Y=interp1(ti,yi,T,'cubic');
% zero the mean
ROffset=mean(Y);
SDR=std(Y);
Rm=Y-ROffset;
XOffset=mean(X);
SDX=std(X);
Xm=X-XOffset;
% Fourier transform
df=1/(N*dt); % Frequency Domain
f=0:df:1/dt-df;
F=f(1:ceil(N/2));
Rg=fft(Rm); % FFT
RG=Rg(1:ceil(N/2));
RA=abs(RG)*2/N; % Amplitude
RA0=RA/max(RA);
RTheta=angle(RG); % Phase
RP=RTheta/(2*pi);
Xg=fft(Xm); % FFT
XG=Xg(1:ceil(N/2));
XA=abs(XG)*2/N; % Amplitude
XA0=XA/max(XA);
XTheta=angle(XG); % Phase
XP=XTheta/(2*pi);
% Identifying Frequencies
[Rmax,locR]=max(RA0);
omegaR=F(locR);
[Xmax,locX]=max(XA0);
omegaX=F(locX);
% Plots
figure
subplot(2,2,1)
plot(F,RA0)
title('Radial')
axis([0 3e6 0 0.6])
subplot(2,2,2)
plot(F,XA0)
title('Axial')
axis([0 3e6 0 0.6])
subplot(2,2,3)
plot(F,RA0)
title('Fourier Transform')
axis([0 3e6 0 0.03])
subplot(2,2,4)
plot(F,XA0)
title('Fourier Transform')
axis([0 3e6 0 0.03])

% End of script
clear m n N S pks
```

```
disp('Finished')
```

A.2.3 Calculating Relative Field Linearity

The linearity of the field can be calculated by comparing it to a linear field. Data collected for this included the potential distribution both radially and axially. This script was designed to take the derivative of the potential distribution, remove outliers to the field, identify the trapping center, determine the linear portion of the field using the minimum number of points for a linear fit, and perform a regression analysis of the actual field to the calculated linear field.

```
clear all; close all;
% Input
data=xlsread('U:\Documents\Research\SIMION\Harmonics\ToroidalHexapoleContribu
tions\StabilitySectionsFor_m-z300\SimFiles\T1 0.25\Potential.xlsx');
Y=data(:,2);
PY=data(:,4);
X=data(:,6)-16;
PX=data(:,9);
% Remove empty (NaN) cells
Y=Y(~any(isnan(Y),2),:);
PY=PY(~any(isnan(PY),2),:);
X=X(~any(isnan(X),2),:);
PX=PX(~any(isnan(PX),2),:);
% Plotting
subplot(2,2,1)
plot(Y,PY)
axis([2 10 40 100])
subplot(2,2,2)
plot(X,PX)
axis([-4 4 0 60])
% Eliminate Dupicates
YI(1)=Y(1);PYI(1)=PY(1);m=1;
for n=2:length(Y)
    if Y(n)~=Y(n-1)
        m=m+1;
        YI(m)=Y(n);
        PYI(m)=PY(n);
    end
end
clear m; clear n;
XI(1)=X(1);PXI(1)=PX(1);m=1;
for n=2:length(X)
    if X(n)~=X(n-1)
        m=m+1;
        XI(m)=X(n);
        PXI(m)=PX(n);
    end
end
```

```
clear m; clear n;
% Interpolate data
dy=(max(YI)-min(YI))/length(YI);
y=min(YI):dy:max(YI)-dy;
py=interp1(YI,PYI,y,'pchip');
dx=(max(XI)-min(XI))/length(XI);
x=min(XI):dx:max(XI)-dx;
px=interp1(XI,PXI,x,'pchip');
% 1st Differential and removing outliers
    %Radial
yn=y; pyn=py; a=1;
while a==1
    yd=yn(1:end-1);
    pyd=diff(pyn);
    for n=2:length(yd)
        if pyd(n-1)>0 && pyd(n)<0
            subplot(2,2,3)
            plot(yd,pyd,yd(n),pyd(n),'ro')
            axis([2 10 -2 2])
            b=input('Remove this point and leftside?  (yes=1;no=0): ');
            if b==1
                yn=yn(n:end);
                pyn=pyn(n:end);
                b=0;
            end
        end
    end
    y1=yn(1:end-1);
    py1=diff(pyn);
    if yn~=y
        subplot(2,2,1)
        plot(Y,PY,yn,pyn,'m-')
        axis([2 10 40 100])
        subplot(2,2,3)
        plot(y1,py1)
        axis([2 10 -2 2])
    end
    a=0;
end
if min(py1)~=py1(1)
    [r,locr]=min(py1);
    subplot(2,2,3)
    plot(y1,py1,y1(locr),r,'ro')
    axis([2 10 -2 2])
    b=input('Remove left of this point?  (yes=1;no=0): ');
    if b==1
        yn=yn(locr:end);
        pyn=pyn(locr:end);
        y1=yn(1:end-1);
        py1=diff(pyn);
        b=0;
    end
    subplot(2,2,1)
    plot(Y,PY,yn,pyn,'m-')
    axis([2 10 40 100])
    subplot(2,2,3)
    plot(y1,py1)
```

```
    axis([2 10 -2 2])
end
if max(py1)~=py1(end)
    [r,locr]=max(py1);
    subplot(2,2,3)
    plot(y1,py1,y1(locr),r,'ro')
    axis([2 10 -2 2])
    b=input('Remove right of this point?  (yes=1;no=0): ');
    if b==1
        yn=yn(1:locr);
        pyn=pyn(1:locr);
        y1=yn(1:end-1);
        py1=diff(pyn);
        b=0;
    end
    subplot(2,2,1)
    plot(Y,PY,yn,pyn,'m-')
    axis([2 10 40 100])
    subplot(2,2,3)
    plot(y1,py1)
    axis([2 10 -2 2])
end
    %Axial
x1=x(1:end-1);
px1=diff(px);
xn=x; pxn=px;
if max(px1)~=px1(1)
    [z,locz]=max(px1);
    subplot(2,2,4)
    plot(x1,px1,x1(locz),z,'ro')
    axis([-4 4 -4 4])
    b=input('Remove left of this point?  (yes=1;no=0): ');
    if b==1
        xn=xn(locz:end);
        pxn=pxn(locz:end);
        x1=xn(1:end-1);
        px1=diff(pxn);
        b=0;
    end
    subplot(2,2,2)
    plot(X,PX,xn,pxn,'m-')
    axis([-4 4 0 60])
    subplot(2,2,4)
    plot(x1,px1)
    axis([-4 4 -4 4])
end
if min(px1)~=px1(end)
    [z,locz]=min(px1);
    subplot(2,2,4)
    plot(x1,px1,x1(locz),z,'ro')
    axis([-4 4 -4 4])
    b=input('Remove right of this point?  (yes=1;no=0): ');
    if b==1
        xn=xn(1:locz);
        pxn=pxn(1:locz);
        x1=xn(1:end-1);
        px1=diff(pxn);
```

```
        b=0;
    end
    subplot(2,2,2)
    plot(X,PX,xn,pxn,'m-')
    axis([-4 4 0 60])
    subplot(2,2,4)
    plot(x1,px1)
    axis([-4 4 -4 4])
end
% Find Trapping Center
[Cpy,locy]=min(pyn);
Cy=yn(locy);
[Cpx,locx]=max(px);
Cx=x(locx);
% Find Linear Region of Field
display('Locating Linear Region of Radial Field')
RunY=1;
while RunY==1
    f=y1;g=py1;
    Ny=input('Enter goal value for Ry^2: ');
    sum1=0; sum2=0; sum3=0; sum4=0; sum5=0;
    for n=1:length(f)
        sum1=sum1+(f(n)*g(n));
        sum2=sum2+f(n);
        sum3=sum3+g(n);
        sum4=sum4+(f(n))^2;
        sum5=sum5+(g(n))^2;
    end
    Ry=(length(f)*sum1-sum2*sum3)/...
        ((length(f)*sum4-sum2^2)^(1/2)*(length(f)*sum5-sum3^2)^(1/2));
    if length(y1)>=2*locy
        m=locy;
    else
        m=length(y1)-locy;
    end
    while Ry^2<Ny
        m=m-1;
        f=y1(locy-m:locy+m);
        g=py1(locy-m:locy+m);
        sum1=0; sum2=0; sum3=0; sum4=0; sum5=0;
        for n=1:length(f)
            sum1=sum1+(f(n)*g(n));
            sum2=sum2+f(n);
            sum3=sum3+g(n);
            sum4=sum4+(f(n))^2;
            sum5=sum5+(g(n))^2;
        end
        Ry=(length(f)*sum1-sum2*sum3)/...
            ((length(f)*sum4-sum2^2)^(1/2)*(length(f)*sum5-sum3^2)^(1/2));
    end
    L=length(f)
    YR=polyfit(f,g,1);
    yr=polyval(YR,y1);
    subplot(2,2,3)
    plot(y1,py1,'b-',y1,yr,'r-')
    axis([2 10 -2 2])
    RunY=input('Want to choose new Ry^2 goal? (yes=1;no=0): ');
```

```
end
pyBAR=mean(py1); SStotY=0; SSregY=0; SSresY=0;
for n=1:length(py1)
    SStotY=SStotY+(py1(n)-pyBAR)^2;
    SSregY=SSregY+(yr(n)-pyBAR)^2;
    SSresY=SSresY+(py1(n)-yr(n))^2;
end
RsqRadial=1-SSresY/SStotY
display('Locating Linear Region of Axial Field')
RunX=1;
while RunX==1
    h=x1;j=px1;
    Nx=input('Enter goal value for Rx^2: ');
    sum1=0; sum2=0; sum3=0; sum4=0; sum5=0;
    for n=1:length(h)
        sum1=sum1+(h(n)*j(n));
        sum2=sum2+h(n);
        sum3=sum3+j(n);
        sum4=sum4+(h(n))^2;
        sum5=sum5+(j(n))^2;
    end
    Rx=(length(h)*sum1-sum2*sum3)/...
        ((length(h)*sum4-sum2^2)^(1/2)*(length(h)*sum5-sum3^2)^(1/2));
    if length(x1)>=2*locx
        m=locx;
    else
        m=length(x1)-locx;
    end
    while Rx^2<Nx
        m=m-1;
        h=x1(locx-m:locx+m);
        j=px1(locx-m:locx+m);
        sum1=0; sum2=0; sum3=0; sum4=0; sum5=0;
        for n=1:length(h)
            sum1=sum1+(h(n)*j(n));
            sum2=sum2+h(n);
            sum3=sum3+j(n);
            sum4=sum4+(h(n))^2;
            sum5=sum5+(j(n))^2;
        end
        Rx=(length(h)*sum1-sum2*sum3)/...
            ((length(h)*sum4-sum2^2)^(1/2)*(length(h)*sum5-sum3^2)^(1/2));
    end
    M=length(h)
    XZ=polyfit(h,j,1);
    xz=polyval(XZ,x1);
    subplot(2,2,4)
    plot(x1,px1,'b-',x1,xz,'r-')
    axis([-4 4 -4 4])
    RunX=input('Want to choose new Rx^2 goal? (yes=1;no=0): ');
end
pxBAR=mean(px1); SStotX=0; SSregX=0; SSresX=0;
for n=1:length(px1)
    SStotX=SStotX+(px1(n)-pxBAR)^2;
    SSregX=SSregX+(xz(n)-pxBAR)^2;
    SSresX=SSresX+(px1(n)-xz(n))^2;
end
```

```
RsqAxial=1-SSresX/SStotX
clear sum1 sum2 sum3 sum4 sum5
% Prepare data to copy to Excel
dataY=[y',py'];
dataX=[x',px'];
dataY1=[y1',py1',yr'];
dataX1=[x1',px1',xz'];
stats=[Ny,Nx;L,M;RsqRadial,RsqAxial];
openvar('dataY')
openvar('dataX')
openvar('dataY1')
openvar('dataX1')
openvar('stats')
openvar('dataY')
% The End
display('Finished')
```

A.2.4 Percentage of Stable Ion Motion in the Apex of the Stability Diagram

In order to compare how many stable points of ion motion are in a stability diagram, the boundaries of the stability diagram need to be identified. The data obtained included the RF amplitude and DC offset settings for ions that were considered to be stably trapped. This script was designed to read the voltage settings for the stably trapped ions, organize data into two data sets, find the stable points at the boundary, extrapolate the $\beta_r = 0$ and $\beta_z = 1$, and calculate the percentage of stable points within the extrapolated boundaries in the region viewed.

```
clear all; close all;
% Input
data=xlsread('File Name');
z=size(data);
% Separate data
RF=data(:,2);
DC=data(:,3);
uRF1=data(:,6);
uDC1=data(:,7);
sets=2;
if z(2)>9
    uRF2=data(:,10);
    uDC2=data(:,11);
    sets=3;
end
if z(2)>13
    uRF3=data(:,14);
    uDC3=data(:,15);
    sets=4;
end
```

```
% Remove empty (NaN) cells
RF=RF(~any(isnan(RF),2),:);
DC=DC(~any(isnan(DC),2),:);
uRF1=uRF1(~any(isnan(uRF1),2),:);
uDC1=uDC1(~any(isnan(uDC1),2),:);
if sets >= 3
    uRF2=uRF2(~any(isnan(uRF2),2),:);
    uDC2=uDC2(~any(isnan(uDC2),2),:);
end
if sets >= 4
    uRF3=uRF3(~any(isnan(uRF3),2),:);
    uDC3=uDC3(~any(isnan(uDC3),2),:);
end
% Select boundary points for extrapolation
RFb(1)=RF(1);DCb(1)=DC(1);m=1;
for n=2:length(RF)
    if RF(n)~=RF(n-1)
        m=m+1;
        RFb(m)=RF(n);
        DCb(m)=DC(n);
    end
end
clear m; clear n;
p1=plot(RFb,DCb);
hold on
RFc=(min(RFb):RFb(2)-RFb(1):max(RFb));
% Select leftside for extrapolation, Identify “peak” to use points left
[pks1,locs1]=findpeaks(-DCb);
p2=plot(RFb(locs1),DCb(locs1),'o');
N1=length(locs1)
b1=input('Select point for leftside extrapolation: ');
delete(p2)
RFb1=RFb(1:locs1(b1)); DCb1=DCb(1:locs1(b1));
A=polyfit(RFb1,DCb1,1);
DCx1=polyval(A,RFc);
p3=plot(RFc,DCx1);
% Select rightside for extrapolation, Identify “peak” to use points right
locs2=[]; m=0;
for n=1:length(locs1)
    if locs1(n)>locs1(b1)
        m=m+1;
        locs2(m)=locs1(n);
    end
end
clear m; clear n;
p4=plot(RFb(locs2),DCb(locs2),'o');
N=length(locs2)
b=input('Select point for rightside extrapolation: ');
delete(p4)
RFb2=RFb(locs2(b):end); DCb2=DCb(locs2(b):end);
B=polyfit(RFb2,DCb2,1);
DCx2=polyval(B,RFc);
p5=plot(RFc,DCx2);
% Find intersection for Apex
RFa=(A(2)-B(2))/(B(1)-A(1));
DCa1=polyval(A,RFa); DCa2=polyval(B,RFa); DCa=(DCa1+DCa2)/2;
p6=plot(RFa,DCa,'*');
```

```
DCx=[];
for n=1:length(RFc)
    if DCx1(n)>DCx2(n)
        DCx(n)=DCx1(n);
    else
        DCx(n)=DCx2(n);
    end
end
p7=plot(RFc,DCx);
delete(p3)
delete(p5)
% Find number of points within theoretical region
stable=0;
for n=1:length(RF)
    z=find(RFc==RF(n));
    if DC(n)>=DCx(z)
        stable=stable+1;
    end
end
unstable1=0;
for n=1:length(uRF1)
    z=find(RFc==uRF1(n));
    if uDC1(n)>=DCx(z)
        unstable1=unstable1+1;
    end
end
unstable2=0;
if sets >= 3
    for n=1:length(uRF2)
        z=find(RFc==uRF2(n));
        if uDC2(n)>=DCx(z)
            unstable2=unstable2+1;
        end
    end
end
unstable3=0;
if sets >= 4
    for n=1:length(uRF3)
        z=find(RFc==uRF3(n));
        if uDC3(n)>=DCx(z)
            unstable3=unstable3+1;
        end
    end
end
unstable=unstable1+unstable2+unstable3;
% Data for export
Apex=[A B RFa DCa stable unstable];
openvar('Apex')
% The End
display('Finished')
```